

Charles University in Prague / Univerzita Karlova v Praze
Faculty of Science / Přírodovědecká fakulta

Study programme / Studijní program: Geologie
Subject of study / Studijní obor: Geologie



Mgr. Zita Bukovská

Localization of deformation in rocks with existing anisotropy:
consequences for geodynamic interpretations

Lokalizace deformace v anizotropních horninách:
důsledky pro geodynamické interpretace

Dissertation thesis / Disertační závěrečná práce

Supervised by / Školitel: RNDr. Petr Jeřábek, PhD.
Co-supervised by / Konzultant: Mgr. Ondrej Lexa, Ph.D.

Praha, 2015

DECLARATION / PROHLÁŠENÍ

I affirm that in the presented Ph.D. thesis I used only data acquired from my own research or from sources mentioned in the list of used literature. I also affirm that I didn't present this work, or even its significant part, to acquire another academic title or the same Ph.D. title at another university.

Prohlašuji, že jsem závěrečnou práci zpracovala samostatně a že jsem uvedla všechny použité informační zdroje a literaturu. Tato práce ani její podstatná část nebyla předložena k získání jiného nebo stejného akademického titulu.

Praha, 6.7.2015

Mgr. Zita Bukovská

ACKNOWLEDGEMENTS

I would like to thank to my supervisors Petr Jeřábek and Ondro Lexa and colleagues from the Institute of Petrology and Structural Geology at the Charles University for their support and help during my work on this thesis. Thanks to Petr for the field work support and the uncountable hours while working on all the below mentioned topics. To Ondro for the patience with my “manták” questions and to Martin for the SEM.

I would like also thank to Luiz F.G. Morales and Ralf Milke who made it possible for me to stay at the German Research Centre GeoForschungsZentrum Potsdam and the Free University Berlin for the great opportunities and support. Extra thanks to Luiz who taught me a lot about the microanalytical techniques and encouraged me into a numerous new fields. Thanks to Richard Wirth for exciting and encouraging work on TEM.

Among these persons I am also thankful to my friends who helped me with any issues and kept me company – the colleagues from Prague, Potsdam and Berlin, among others my office mates Niki, Vanessa, Maïke and Oli and my great Alpine field assistant Pét’a. I am grateful for all the discussions with numerous geoscientists I had opportunity to take on conferences, seminars etc.

Special thanks belong to my family and friends for the support and patience.

This work was supported by Charles University Grant Agency projects No. 5041/2012 and 13702/2014 and the Erasmus work placement programme.

PUBLICATIONS

Bukovská, Z., Jeřábek, P., Lexa, O., Konopásek, J., Janák, M., Košler, J., 2013. Kinematically unrelated C-S fabrics: an example of extensional shear band cleavage from the Vepor Unit, West Carpathians. *Geologica Carpathica* 64, 2, 103-116.

Bukovská, Z., Wirth, R., Morales, L.F.G. Pressure solution in rocks: FIB/TEM study on orthogneiss from South Armorican Shear Zone, France. *Contributions to Mineralogy and Petrology*, accepted

Bukovská, Z., Jeřábek, P., Morales, L.F.G. Major softening at brittle-plastic transition due to interplay between chemical and deformation processes: an insight from evolution of shear bands in the South Armorican Shear Zone. *Journal of Geophysical Research: Solid Earth*, submitted

Bukovská, Z., Jeřábek, P. Two separate orogen-parallel extension events in the Tauern Window revealed by crystallization – deformation relations, in preparation for *Journal of Metamorphic Petrology*

CONFERENCE CONTRIBUTIONS AND INVITED TALKS

Bukovská, Z., Wirth, R., Morales, L.F.G., 2015. Pressure Solution in Natural Samples: FIB/TEM Study on Orthogneiss from South Armorican Shear Zone, France. Goldschmidt Conference, Prague, Czech Republic (Talk)

Bukovská, Z., Wirth, R., Morales, L.F.G., 2015. Pressure solution in rocks: focused ion beam/transmission electron microscopy study on orthogneiss from South Armorican Shear Zone, France. University of Bochum, Germany (Invited talk)

Bukovská, Z., Jeřábek, P., 2015. Tectono-metamorphic evolution of western part of Tauern Window, Eastern Alps. Central European Tectonic Studies Group Meeting, Kadaň, Czech Republic (Talk)

Bukovská, Z., Jeřábek, P., 2014. Structural and metamorphic evolution of western part of Tauern Window. AGU Fall Meeting, San Francisco, USA (Poster)

Wirth, R., Bukovská, Z., Morales, L.F.G., 2014. Pressure solution in natural samples: FIB/TEM study on Orthogneiss from South Armorican Shear Zone, France. AGU Fall Meeting, San Francisco, USA (Poster, Presenting Author)

Bukovská, Z., Jeřábek, P., Lexa, O., Morales, L.F.G., Milke, R., 2014. The brittle-viscous-plastic evolution of shear bands in the South Armorican Shear Zone. EGU General Assembly, Vienna, Austria (Talk)

Bukovská, Z., Jeřábek, P., 2014. Tectonometamorphic record in the cover sequences of the western Tauern Window, Eastern Alps. 15th Symposium on Tectonics, Structural Geology and Geology of Crystalline Rocks, Potsdam, Germany (Poster)

Bukovská, Z., Jeřábek, P., Lexa, O., Morales, L.F.G., 2013. The progressive development

of shear bands from South Armorican Shear Zone, France. 19th International Conference on Deformation Mechanisms, Rheology and Tectonics, Leuven, Belgium (Talk)

Bukovská, Z., Jeřábek, P., 2013. Tectonometamorphic record in the cover sequences of the western Tauern Window, Eastern Alps. EGU Emile Argand Conference on Alpine Geological Studies, Schladming, Austria (Poster)

Bukovská, Z., Jeřábek, P., Lexa, O., Morales, L.F.G., 2013. The progressive development of shear bands in orthogneiss of the South Armorican Shear Zone, France. Central European Tectonic Studies Group Meeting, Hungary (Poster)

Bukovská, Z., 2012. The development of SC structures, an example of deformed granites of South Armorican Shear Zone, France. Student Conference on Geology 2012, Brno, Czech Republic (Talk)

Bukovská, Z., Jeřábek, P., Lexa, O., Konopásek, J., Janák, M., 2011. Structural characterization of Eastern part of the contact zone between the Gemer and Vepor units and its implications for evolution, West Carpathians. 10th Christmas Meeting of Slovak Geological Society, Bratislava, Slovakia (Talk)

Bukovská, Z., Jeřábek, P., Lexa, O., Konopásek, J., Janák, M., 2011. Diachronous SC geometries: an example from the Vepor Unit, West Carpathians. 18th International Conference on Deformation Mechanisms, Rheology and Tectonics, Oviedo, Spain (Poster)

Bukovská, Z., Jeřábek, P., Lexa, O., Janák, M., 2011. Diachronous SC' geometries and its significance for geotectonic evolution: an example from Vepor Unit, West Carpathians. Student Conference on Geology 2011, Prague, Czech Republic (Talk)

Bukovská, Z., Jeřábek, P., Lexa, O., Janák, M., 2011. Structural characterization of eastern part of the separation zone between the Gemer and Vepor Units in the West Carpathians, Central European Tectonic Studies Group Meeting, Skalský Dvůr, Czech Republic (Talk)

Bukovská, Z., Jeřábek, P., Lexa, O., 2010. The polyphase deformational record at the eastern contact of Vepor and Gemer Unit in West Carpathians. Student Conference on Geology, Brno, Czech Republic (Talk)

Bukovská, Z., Jeřábek, P., Lexa, O., 2010. Polyphase deformation fabrics at the eastern contact of the Vepor and Gemer Units in the West Carpathians, Slovakia. Central European Tectonic Studies Group Meeting, Machocice Kapitulne, Poland (Poster)

SUMMARY

This thesis is focused on the localization of deformation in rock with existing anisotropy, which can be seen in the form of S-C fabric (structure) or shear bands, and the interpretation of its significance in geodynamic studies. Therefore this work includes characterization of shear bands that are formed by deformation localization in broad spectra of conditions and from regional scale to the nanoscale. Since the S-C fabrics and shear bands were firstly described (Berthé et al., 1979; White, 1980, Gapais and White, 1982) these structures are often used while interpreting the rock geodynamic evolution, however, its detailed evolution is not well known. The aim of this study was to describe the detailed evolution of shear bands within the regional field work and microstructural study. The field work was followed by macroscopic and microscopic analyses of deformation structures revealing the origin and evolution of shear bands and S-C fabrics (structures, geometries) as study on rocks from selected regions that are mostly Variscan in origin, however, have been reworked by several deformation phases during Variscan and/or Alpine formation. Field works were conducted in Tauern Window in Eastern Alps at the border of Austria/Italy, in Central West Carpathians in Slovakia and in Armorican Massif in France with the emphasis on S-C fabric and shear band characterization with respect to the regional evolution. The microstructural analyses were focused on characterization of shear band evolution with respect to deformation mechanisms, the estimate on pressure and temperature conditions, chemistry changes and its consequences for rheology.

Chapter I

The tectono-metamorphic evolution of the westernmost part of Tauern Window shows the importance of combining structural observations with petrological data. The structural record in the studied area is dominated by the Alpine deformations that exhumed the Variscan granitoids from below the overlying Penninic and Subpenninic nappes and Austroalpine units. The main foliation is flat to gently dipping towards NNW-SSE and follows the structure of the contact between the deformed granitoids of Venediger Duplex and the overlying rocks. This fabric contains in numerous different lithologies metamorphic garnet that is syn- to post-kinematic with respect to the S1 fabric and the estimated P-T conditions show prograde metamorphic path in the region. This fabric is mainly in Penninic and Subpenninic nappes overprinted by F2 folds that were formed in N-S shortening that is in the studied area followed by escape of the nappes to the W. All together the petrologic observations with the

structural data show the kinematically unrelated S-C fabrics and the tectono-metamorphic evolution of Tauern Window comprising two E-W orogen-parallel extension phases related to the nappe stacking that formed the main S1 E-W stretching fabric later overprinted by the N-S shortening that steepened the nappe stack of Venediger duplex and folded the overlying sequences and caused the response of second orogen-parallel extension and lateral escape towards W.

Chapter II

In the study at the boundary region of major basement-cover Vepor and Gemer units in the Central West Carpathians the occurrence of S-C fabrics plays an important role. The study shows the structural evolution of the area together with metamorphic overprint and dating of the fabrics. The Vepor Unit and its contact zone are represented by orthogneiss, quartzite and chloritoid-kyanite schist. The S-C fabrics occur within a major detachment shear zone, which crosscuts the earlier imbricated structure related to overthrusting of the Gemer Unit over Vepor Unit. The formation of S-C fabric is thus associated with Cretaceous syn-burial orogen-parallel flow and subsequent exhumational unroofing. The formation of the two fabrics characterized by distinct quartz deformation microstructure and metamorphic assemblage is separated by an inter-tectonic growth of transversal chloritoid-, kyanite-, \pm monazite-bearing assemblage. The discussion shows that the S-C fabrics as documented in this study area reveal the kinematically unrelated formation of two sets of fabric. The age of this inter-tectonic metamorphic stage together with existing $^{40}\text{Ar}/^{39}\text{Ar}$ ages on exhumation of the Vepor Unit indicate that despite the similar appearance to shear bands or S-C mylonites there is at least 10 my time span between the formation of homogeneous S fabrics and superposed discrete C fabrics in the studied rocks. The S fabric formed during Early Cretaceous subhorizontal lateral flow associated with overthrusting of the Gemer Unit and burial of the Vepor Unit, while the C fabric originated via Late Cretaceous extensional shearing within the major detachment shear zone associated with exhumation of the Vepor Unit.

Chapter III

The detailed microstructural study on the evolution of the originally defined S-C fabric from South Armorican Shear zone revealed a complicated story of deformation mechanisms changes its positive feedback to the chemical and mechanical processes. The fabrics are generally believed to be formed during the synkinematic cooling of plutons along the South Armorican shear zone at 315 – 300 Ma. The two fabrics formation differs by at least 200 °C

in temperature. We describe three main stages of the shear band (C fabric) evolution that include initiation of shear band formation by microcracking (stage I) followed by subgrain rotation recrystallization in quartz and coeval dissolution precipitation creep (stage II) in microcline. The recrystallizing quartz data allowed us to discuss some mechanical constraints on microcline dissolution precipitation which suggest creep at 17 – 26 MPa differential stress and the strain rate of $1.8 \cdot 10^{-15} \text{ s}^{-1}$. The stage III is characterised by localized slip on white mica bands accommodated by dislocation creep at strain rate $1.8 \cdot 10^{-14} \text{ s}^{-1}$ and stress 5.75 MPa. The discussion includes the geometrical constraints on the shear band and S-C fabric evolution as well as the mechanisms and its response in the deforming granites in the shear zone that is connected to the fluid presence and rheological implications. The mechanical data point to non-steady-state evolution of the brittle-plastic transition in the South Armorican Shear Zone characterized by major weakening to strengths lower than 10 MPa.

Chapter IV

Pressure solution features in the orthogneiss from South Armorican Shear Zone were studied in the means of transmission electron microscopy in places previously chosen with optical microscopy. The pressure solution features were found in great extent at the interfaces of quartz, K-feldspar and white mica. At the interfaces of quartz and white mica the pressure solution of quartz follows the dislocations and is related to the crystallographic orientation of the quartz grains. Solution pits are formed at the interfaces that are parallel to the basal planes of white mica while where the white mica basal planes are perpendicular the mica overgrows the quartz. In order to see the 3D extent of these features the focused ion beam was used to produce the 3D view on the interface changes which shows the continuity of the pits that were formed at the interface. In case the mica basal planes are at acute angle to the quartz interface the amorphous layers occur. In case of K-feldspar and white mica interfaces the K-feldspar is being dissolved or leached which is a reason for amorphous layer formation. The observed features are discussed with respect to the previously described models that describe the dissolution precipitation creep (e.g. Gratier et al., 2013, Wassmann and Stöckhert, 2013), formation of amorphous layers via interface-coupled dissolution precipitation creep as described by Hellmann et al. (2012). In order to understand the pressure solution on such interfaces the discussion on the main compressive stress orientation is included. Our data show that within the presence of external stresses the respective crystallographic orientation of phases plays a major role, as well as the fluid presence that directly dissolve the mineral phases, and the local dislocation density or more general the defect density.

ABSTRAKT

Lokalizace deformace se vyskytuje v zemské kůře jako důsledek aplikovaného napětí a je rozšířeným fenoménem, který lze sledovat v korových horninách. Obvykle se lokalizace deformace projevuje ve formě střížných zón. Střížné zóny malého měřítka označované jako střížné pásy (shear bands), které jsou součástí S-C struktur jsou často využívány jako kinematické indikátory, ačkoli jejich vývoj, kinematický rámec a kontinuita nejsou dobře definovány. Interpretace geodynamického vývoje nemusí být pak jednoznačná a snadná. Z hlediska kinematické kontinuity a vývoje byly rozlišeny a popsány dva typy S-C struktur: a) kinematicky nekontinuální S-C struktury tvořené v průběhu více deformačních událostí a b) kinematicky kontinuální S-C struktury tvořené během jediné deformační události. Kinematicky nekontinuální S-C struktury byly studovány v západní části Taurského okna ve Východních Alpách a v Gemersko-veporské kontaktní zóně v Centrálních Západních Karpatech, kde předcházející geodynamické interpretace misinterpretovaly význam struktur lokalizace deformace. Kinematicky kontinuální S-C struktury byly studovány v Jihoarmorické střížné zóně, kde byly S-C struktury definovány a poprvé popsány (Berthé a kol., 1979).

Navzájem protínající se stavby pod malými úhly tvořící S-C geometrie byly dokumentovány v rámci terénních prací a dále studovány od makroměřítka, přes mikroměřítka až k nanoměřítka. Hlavní část práce byla věnována mikrostrukturním analýzám jednotlivých staveb a deformačním mechanismům, minerálním asociacím a změnám chemického složení minerálů, teplotně-tlakovým podmínkám, věkovým odhadům apod.

Kinematicky kontinuální S-C struktury jsou tvořené sledem několika deformačních mechanismů provázaných jednak s chemickými změnami v hornině, tak s mechanickými změnami a přítomností fluid. Sledované vztahy ukazují na významné snížení pevnosti v oblasti křehce-plastického rozhraní a nerovnovážený vývoj. Z druhé strany přítomnost kinematicky nekontinuálních S-C struktur odhaluje polyfázový vývoj zahrnující pohřbení a následnou exhumaci korových hornin v extenzním režimu, kdy subparalelní stavby S a C jsou tvořeny v průběhu odlišných deformačních událostí a za odlišných podmínek.

Tato disertační práce ukazuje, že detailní rozlišení kinematicky kontinuálních a nekontinuálních S-C struktur je zásadní pro interpretace geodynamického vývoje a podává důležité poznatky o propojení deformačních mechanismů a reologie hornin.

ABSTRACT

Localization of deformation occurs in Earth's crust as a consequence of applied stress and is widespread phenomenon that can be found in crustal rocks. Such localization of deformation can be mostly seen in a form of shear zones. Small shear zones referred as shear bands or S-C structures are often used as kinematic indicators. However, the evolution and kinematic continuity of such structures is not well identified, which makes it problematic when interpreting regional geodynamic evolution. Two possible cases were distinguished and described in this thesis: a) kinematically discontinuous S-C structures formed during two deformation events and b) kinematically continuous S-C structures formed during single deformation event. Kinematically unrelated S-C structures were studied in westernmost part of Tauern Window in Eastern Alps and in Gemer-Vepor Contact Zone in Central West Carpathians where previous geodynamic interpretations might have misinterpreted localization structures. Kinematically continuous shear bands were studied in South Armorican Shear Zone where the S-C fabrics were originally defined and described (Berthé et al., 1979).

Two fabrics that crosscut each other at small angles forming S-C geometries were documented during field work and studied from macroscale down to microscale or nanoscale. Main part of the work focused on microstructural analyses of the respective fabrics and its deformation microstructures, mineral assemblages and mineral chemistry changes, pressure-temperature conditions, age estimates etc.

Kinematically continuous S-C structures formed by several deformation mechanisms, which are connected both to chemical changes in the rock as well as mechanical changes and presence of fluids. The observed relationships show dramatic weakening at brittle-plastic transition in non-steady-state regime. On the other hand presence of kinematically discontinuous S-C structures reveal polyphase evolution documenting burial and extensional exhumation of basement rocks, where the S and C fabrics form subparallel and crosscut each other at different conditions during different deformation events.

This thesis shows that proper distinguishing of kinematically continuous and discontinuous S-C structures/shear bands is fundamental while interpreting consequences for geodynamic evolution and detailed studies give important observations of interplay of deformation mechanisms and rock rheology.

LIST OF CONTENTS

INTRODUCTION	3
CHAPTER I: TWO SEPARATE OROGEN PARALLEL EXTENSION EVENTS IN THE TAUERN WINDOW REVEALED BY CRYSTALLIZATION-DEFORMATION RELATIONS	7
1 INTRODUCTION	8
2 GEOLOGICAL SETTING	8
3 STRUCTURAL RECORD	10
4 PETROGRAPHY OF STUDIED ROCKS	13
4.1 VENEDIGER BASEMENT	13
4.2 VENEDIGER COVER.....	15
4.3 SUBPENNIC NAPPEs.....	16
4.4 PENNIC NAPPEs.....	16
5 MINERAL CHEMISTRY	18
5.1 GARNET CHEMISTRY.....	18
6 P-T CONDITIONS	22
7 DISCUSSION	26
8 CONCLUSIONS	29
CHAPTER II: KINEMATICALLY UNRELATED S-C FABRICS: AN EXAMPLE OF EXTENSIONAL SHEAR BAND CLEAVAGE FROM THE VEPOR UNIT, WEST CARPATHIANS	34
1 INTRODUCTION	34
2 GEOLOGICAL SETTING	35
3 STRUCTURAL RECORD IN THE STUDIED AREA	38
4 ANALYTICAL TECHNIQUES	40
5 QUARTZ DEFORMATION MICROSTRUCTURE	41
6 QUARTZ TEXTURE	43
7 PETROGRAPHY AND MINERAL CHEMISTRY	43
8 MONAZITE DATING	49
9 DISCUSSION	51
10 CONCLUSIONS	54
CHAPTER III: MAJOR SOFTENING AT BRITTLE-PLASTIC TRANSITION DUE TO INTERPLAY BETWEEN CHEMICAL AND DEFORMATION PROCESSES: AN INSIGHT FROM EVOLUTION OF SHEAR BANDS IN THE SOUTH ARMORICAN SHEAR ZONE	60
1 INTRODUCTION	61
2 SAMPLE LOCALIZATION AND DESCRIPTION	62
3 ANALYTICAL METHODS	63
4 CHARACTERIZATION OF S-C FABRICS	64
4.1 MICROCRACKS AND SHEAR BANDS	66
4.2 MINERAL CHEMISTRY OF S AND C FABRICS.....	68
4.3 P-T CONDITIONS OF SHEAR BAND FORMATION	70
4.4 MICROSTRUCTURE OF SHEAR BANDS	73
4.5 QUANTITATIVE MICROSTRUCTURAL ANALYSIS OF SHEAR BANDS.....	75
4.5.1 <i>Crystallographic preferred orientation in shear bands</i>	77
5 DISCUSSION	82
5.1 S-C FABRICS IN THE SOUTH ARMORICAN SHEAR ZONE: THEIR ORIGIN AND GEOMETRY	82
5.1.1 <i>Initiation of shear bands</i>	83
5.1.2 <i>Geometry of S-C fabrics</i>	84

5.2	MECHANISMS RELATED TO FORMATION AND EVOLUTION OF SHEAR BANDS	85
5.3	RHEOLOGICAL IMPLICATIONS	88
5.4	STRENGTH EVOLUTION AT BRITTLE-PLASTIC TRANSITION	91
6	CONCLUSIONS	92
CHAPTER IV: PRESSURE SOLUTION IN ROCKS: FOCUSED ION BEAM/TRANSMISSION ELECTRON MICROSCOPY STUDY ON ORTHOGNEISS FROM SOUTH ARMORICAN SHEAR ZONE, FRANCE		100
1	INTRODUCTION	101
2	GEOLOGICAL SETTING AND SAMPLE DESCRIPTION	102
3	ANALYTICAL TECHNIQUES AND SAMPLE PREPARATION	104
4	RESULTS	105
4.1	QUARTZ – WHITE MICA PHASE BOUNDARY	105
4.2	K-FELDSPAR – WHITE MICA PHASE BOUNDARY	109
5	DISCUSSION	113
6	CONCLUSIONS	117
CONCLUSIONS		122

INTRODUCTION

One of the main problems in structural geology is the ambiguity of kinematic interpretation of data obtained by geometrical analysis of deformation structures. Kinematic analysis is based on detailed knowledge on polyphase rock deformation evolution of structural elements, its kinematic continuity. The identification of structural element continuous or discontinuous evolution is thus becoming fundamental for structural analysis and geodynamic interpretations.

The classical example of kinematically continuous planar structures are e.g. conjugated shear zones, also known as extensional shear bands, that crosscut planar fabric at low to medium angles (e.g. Passchier and Trouw, 2005). This geometric relationship is traditionally known as shear bands (White, 1979; White et al., 1980; Gapais and White 1982; Gapais, 1989), C- and C'-bands (Berthé et al. 1979; Ponce and Choukroune, 1980), extensional crenulation cleavage (Platt, 1979, 1984; Platt and Vissers, 1980), asymmetric boudinage, asymmetric folds or shear kink bands (e.g. Dewey, 1965; Cosgrove, 1976; Cobbold, 1979).

Shear bands formed in the kinematic continuity were for the first time described and defined in South Armorican Shear Zone by Berthé et al. (1979). Since this work are the S-C and S-C' structures used for kinematic interpretations on all scales, even though their mechanical consequence is not well known. On the other hand, S-C and S- C' structures may be formed as a consequence of overprint of older planar fabric by younger cleavage, thus in kinematically unrelated deformation phases. The S-C fabrics are mostly formed in rocks with existing anisotropy in medium-grade shear zones, especially in granitoids and might be followed by formation of C' shear bands (Berthé et al., 1979).

Time- or kinematic- relationship of existing anisotropy and newly evolving zones of localized deformation appears to be the crucial unanswered problem for application of the shear band concept in structural field studies. Two possibilities arise: a) the existing anisotropy and localization of deformation is formed in kinematic continuity, which represents failure of anisotropy stability because of strain increase (e.g. Holyoke and Tullis, 2006) or b) localized shear deformation is overprinting anisotropy that has evolved during previous kinematically unrelated deformation phase.

This study focuses on shear bands in crustal rocks, where shear bands and S-C fabrics are often used as kinematic indicators (e.g. Malavielle and Cobb, 1986; Blenkinsop and Treloar, 1995) and are expected to be found at conditions close to brittle plastic transition (e.g. Fousseis

and Handy, 2008). The aim of this work is to describe mechanisms of shear band formation and indicative criteria for distinction of above mentioned concepts of shear band evolution on the basis of geometry, chemical and microstructural analyses complemented with other analytical techniques.

As a case study was chosen the field area of South Armorican Shear Zone where shear bands were described and defined as kinematically continuous structures by Berthé et al. (1979). This is complemented with field area in the Vepor-Gemer Contact Zone in Central West Carpathians where the presence of S-C fabrics (Plašienka, 1993; Hók et al., 1993) led to interpretation of exhumation through brittle-ductile unroofing (Plašienka et al., 1999; Janák et al., 2001), however, recent studies dispute these observations (e.g. Jeřábek et al., 2007). Another field area is the western part of Tauern Window which reveals some characteristics similar to the area in Carpathians and its exhumation history was discussed in many works (e.g. Selverstone, 1988; Fügenschuh, 1997; Lammerer and Weger, 1998; Rosenberg and Garcia 2011). The rocks from selected regions are mostly Variscan in origin, however, have been reworked by several deformation phases during Variscan and/or Alpine formation. Field works were conducted with the emphasis on S-C fabric and shear band characterization and with respect to regional evolution. The observations as follows are looking for the criteria on different scales – from regional field work and interpretations down to nanoscale using different techniques. Combination of microanalytical techniques focused on characterization of shear band evolution with respect to deformation mechanisms, estimate on pressure and temperature conditions, chemistry changes and its consequences for rheology. The microanalytical results were connected to the field observations in order to interpret geodynamic evolution.

The studied cases of shear bands within S-C fabrics reveal both kinematically related and kinematically unrelated fabrics, which are distinguished by different deformation microstructures, mineral associations, age of deformation and P-T condition. The results show that it is crucial to study shear bands and S-C structures in detail both in field and in laboratory using microanalytical techniques to understand the relationships and mechanisms of formation, which might be extrapolated to interpretation of geodynamic evolution. There is also great importance to obtain observations on different scales in relation to the deformation mechanisms as these are the primary mechanisms for lithospheric deformations and thus carry important information on crustal rheology.

The individual parts of this thesis are sorted from regional scale studies that focus on the

interpretation of S-C fabrics with respect to regional evolution in Tauern Window (Chapter I) and in Vepor-Gemer Contact Zone (Chapter II), towards the very detailed description of mechanisms that formed shear bands in the South Armorican Shear Zone (Chapter III) down to even more closer look to the dissolution-precipitation process in these shear bands (Chapter IV).

References

Berthé, D., Choukroune, P., Jegouzo, P. (1979). Orthogneiss, mylonite and noncoaxial deformation of granites: the example of the South Armorican Shear Zone. *Journal of Structural Geology* 1, 31-42.

Blenkinsop, T. G., Treloar, P. J. (1995). Geometry, classification and kinematics of SC and SC' fabrics in the Mushandike area, Zimbabwe. *Journal of Structural Geology*, 17(3), 397-408.

Cobbold, P. R. (1979). Removal of finite deformation using strain trajectories. *Journal of Structural Geology*, 1(1), 67-72.

Cosgrove, J. W. (1976). The formation of crenulation cleavage. *Journal of the Geological Society*, 132(2), 155-178.

Dewey, J. F. (1965). Nature and origin of kink-bands. *Tectonophysics*, 1(6), 459-494.

Fügenschuh, B., Seward, D., Mancktelow, N. (1997). Exhumation in a convergent orogen: the western Tauern window. *Terra Nova*, 9(5-6), 213-217.

Fusseis, F., Handy, M. R. (2008). Micromechanisms of shear zone propagation at the brittle–viscous transition. *Journal of Structural Geology*, 30(10), 1242-1253.

Gapais, D. (1989). Shear structures within deformed granites: Mechanical and thermal indicators, *Geology* 17, 1144-1147.

Gapais, D., White, S.H. (1982). Ductile shear bands in a naturally deformed quartzite, *Textures and Microstructures*, 5, 1-17.

Hók, J., Kováč, P., Madarás, J. (1993). Extensional tectonics of the western part of the contact area between Veporicum and Gemicum (Western Carpathians). *Mineralia Slovaca* 25, 172-176 (in Slovak with English summary).

Holyoke, C. W., Tullis, J. (2006). Mechanisms of weak phase interconnection and the effects of phase strength contrast on fabric development, *Journal of Structural Geology*, 28 (4), 621-640.

Janák, M., Plašienka, D., Frey, M., Cosca, M., Schmidt, S.T., Lupták, B., Méres, Š. (2001). Cretaceous evolution of a metamorphic core complex, the Veporic unit, Western Carpathians

(Slovakia): P–T conditions and in situ $^{40}\text{Ar}/^{39}\text{Ar}$ UV laser probe dating of metapelites. *Journal of Metamorphic Geology* 19, 197–216.

Jeřábek, P., Stünitz, H., Heilbronner, R., Lexa, O., Schulmann, K. (2007). Microstructural-deformation record of an orogen-parallel extension in the Vepor Unit, West Carpathians. *Journal of Structural Geology*, 29(11), 1722-1743.

Lammerer, B., Weger, M. (1998). Footwall uplift in an orogenic wedge: the Tauern Window in the Eastern Alps of Europe. *Tectonophysics*, 285(3), 213-230.

Malavieille, J., Cobb, F. (1986). Cinématique des déformations ductiles dans trois massifs métamorphiques de l'Ouest des Etats-Unis: Albion (Idaho). Raft River et Grouse Creek (Utah): *Bulletín de la Societ  G ologique de France*, 8, 885-898.

Passchier, C. W., Trouw, R. A. J. (2005). *Microtectonics*, 366 pp.

Plašienka, D. (1993). Structural pattern and partitioning of deformation in the Veporic Foederata cover unit (Central Western Carpathians), in: Rakús M. and Vozár J. (Eds.): *Geodynamic Model and Deep Structure of the Western Carpathians*. pp. 269-277.

Plašienka, D., Janák, M., Lupták, B., Milovský, R., Frey, R. (1999). Kinematics and metamorphism of a Cretaceous core complex: the Veporic unit of the Western Carpathians. *Phys. Chem. Earth (A)* 24, 651-658.

Platt, J.P. (1979). Extensional crenulation cleavage. In: Cobbold P.R. and Fergusson C.C. (Eds.): *Description and Origin of Spatial Periodicity in Tectonic Structures*, Report on a Tectonic Studies Group Conference. *Journal of Structural Geology* 1. Pergamon, Oxford - New York, International, pp.95-96.

Platt, J.P. (1984). Secondary cleavages in ductile shear zones. *Journal of Structural Geology* 6, 439-442.

Platt, J.P., Vissers, R.L.M. (1980). Extensional structures in anisotropic rocks. *Journal of Structural Geology* 2, 397-410.

Ponce, L.M.I., Choukroune, P. (1980). Shear zones in the Iberian Arc. *Journal of Structural Geology* 2, 63-68.

Rosenberg, C. L., Garcia, S. (2011). Estimating displacement along the Brenner Fault and orogen-parallel extension in the Eastern Alps. *International journal of earth sciences*, 100(5), 1129-1145.

Selverstone, J. (1988). Evidence for east-west crustal extension in the Eastern Alps: Implications for the unroofing history of the Tauern window. *Tectonics*,7(1), 87-105.

White, S.H. (1979). Grain and sub-grain size variations across a mylonite zone. *Contributions to Mineralogy and Petrology* 70, 193-202.

White, S.H., Burrows, S.E., Carreras, J., Shaw, N.D., Humphreys, F.J. (1980). On mylonites in ductile shear zones. *Journal of Structural Geology* 2, 175-187.

TWO SEPARATE OROGEN-PARALLEL EXTENSION EVENTS IN THE TAUERN WINDOW REVEALED BY CRYSTALLIZATION-DEFORMATION RELATIONS

Zita Bukovská^{1,2}, Petr Jeřábek^{1,2}

¹ Institute of Petrology and Structural Geology, Faculty of Science, Charles University, Albertov 6, 128 43 Prague 2, Czech Republic

² Czech Geological Survey, Klárov 131/3, 112 81 Prague 1, Czech Republic

Abstract

The westernmost Tauern Window is traditional area of studied on exhumation history tectonic window. The study was focused on combining the structural observations with petrological data in order to describe the tectono-metamorphic evolution of this part of tectonic window. The area represents the nappe stack of post-Variscan Venediger basement and Permo-Carboniferous and Early Mesozoic cover sequences together with Subpenninic and Penninic nappes. The structure of the area is dominated by S1 fabric that corresponds to the nappe stack structure of the area, duplicates the lithology contacts and bears E-W trending lineation L1. This fabric is mainly in the Penninic nappes overprinted by shortening in form of tight folds F2 with steep axial planes S2 and subhorizontal fold axes trending E-W. Close to the basement-cover contact and overlying nappes the S3 fabric is found in the form of cleavage or individual shears, occasionally also small folds with N-S trending axes. The lineation L3 is trending E-W parallel to the L1. The metamorphic evolution is defined by presence of syn- to post-kinematic garnet in S1 fabric and retrograde micas and chlorite in S3 fabric. The garnets show preserved zoning with overall increase of almandine and decrease in spessartine component. The thermodynamic conditions modeled with Perple_X show prograde metamorphic path for garnet from all nappes with increase P-T conditions from ~460 °C to ~560 °C and from ~4 to ~9 kbar.

The S1 fabric with presence of prograde syn- to post-kinematic garnets evolves during nappe stacking and flattening, that is accommodated by E-W extension. The second phase forms large folds in the N-S shortening regime which induces subsequent exhumation of basement nappes within the E-W extension that produces the steep C fabric of kinematically discontinuous S-C fabrics mainly in the western part of the studied area and small scale folds with the top-to-the W kinematics.

Keywords: *orogen-parallel extension, Tauern Window, kinematically discontinuous S-C fabric*

1 Introduction

The S-C fabrics are often used as kinematic indicators in geodynamic interpretations. The main controversy related to the field interpretation of S-C fabrics is their temporal and kinematic relationship, i.e. within shear zone the C fabrics form either as a result of increasing strain (e.g. Berthé et al., 1979; Selverstone, 1988) or due to the overprint of an earlier kinematically unrelated anisotropy (Lister and Snoke, 1984; Agard et al. 2011; Bukovská et al., 2013).

Structure of the Tauern Window is build by dome-like nappe stack (e.g. Frisch, 1980; Schmid et al., 2013). The exhumation of Tauern Window is assumed to be connected to N-S shortening which was compensated by extensional unroofing (Selverstone, 1988; Ratschbacher et al., 1989; Behrmann and Frisch, 1990; Fügenschuh et al., 1997; Lammerer and Weger, 1998; Neubauer et al., 1999; Frisch et al., 2000; Scharf et al., 2013; Bertrand, 2015), or by folding and erosion (e.g. Behrmann, 1988; Rosenberg et al., 2004; Rosenberg and Garcia, 2011) in a sense the area represents either dome-like structure characterised by orogen-parallel extension or typical core complex driven mainly by gravitational forces. The evolution of orogen parallel dome-like structures is related with extension, typically with multiscale upright folding and upper crustal ductile thinning mechanisms that are driving the growth and destruction of the dome. Subhorizontal foliation and orogen parallel stretching lineation can be related to prograde metamorphic evolution associated with burial (Jeřábek et al., 2008, 2012) and not exhumation as it is typical for the orogen parallel extensional dome-like structures as documented e.g. from studied area (e.g. Selverstone and Spear, 1985).

In order to understand the evolution of the westernmost Tauern Window and the significance of S-C fabrics we present a detailed structural study in combination with microstructural relations of fabrics and metamorphic minerals.

2 Geological Setting

The Tauern Window represents a tectonic window in the Eastern Alps (Fig. 1) that exposes Variscan rocks of the distal European margin and the overlying Penninic oceanic rocks from beneath the Austroalpine units of the Adriatic margin in a large-scale domal structure (e.g. Staub, 1924; Frisch, 1980). The subcretion of oceanic and continental Europe-derived crust below the Adria upper plate and subsequent doming and lateral extrusion resulted from Late Cretaceous-Miocene subduction-collision process (Schmid et al., 2013 and references

therein).

The studied area is located in the westernmost part of the Tauern Window (Figs. 1, 2). Here, the lowermost unit is represented by the basement granitoids and orthogneiss of the subpenninic Venediger Duplex (Tuxer and Zillertaler Kern; Frisch, 1976; Schmid et al., 2013). These rocks were derived from the distal European margin (e.g. Schmid et al., 2013); they are late-Variscan (310-270 Ma) and were only affected by the Alpine metamorphism. The basement rocks of the Venediger Duplex are overlain by the post-Variscan cover sequence of Permo-Carboniferous and Early Mesozoic sedimentary age represented by various metasediments and metavolcaniclastics (Veselá et al., 2008; 2011) and by allochthonous metasediments of the Subpenninic nappes in hanging wall of Venediger Duplex represented by Wolfendorn and Modereck nappe systems (e.g. Frisch, 1974). These nappes are overlain by ophiolite-bearing units of Penninic nappes represented by the Glockner nappe system consisting of greenschists (prasinities) and calcschists of the Valais ocean (Staub, 1924; Pestal et al., 2009).

The Venediger Duplex cover rocks together with the Subpenninic nappes were previously called Lower (untere) Schieferhülle and the Penninic nappes as Upper (obere) Schieferhülle (e.g. Thiele, 1980; Selverstone, 1985). We will not use these local terms and stick to the nappe related names as it was suggested by Schmid et al. (2013). For clear distinction we will use the term Venediger basement for Venediger Duplex rocks *sensu stricto* and Venediger cover for its cover sequences and Subpenninic nappes for the overlying Modereck and Wolfendorn nappes.

In the studied area the rocks of Venediger basement include pre-Variscan quartzite, biotite schist and amphibolite (rocks of “Altes Dach”) as well as post-Variscan granite – granodiorite (“Zentralgneis”) that is often deformed to orthogneiss. The Venediger cover sequences of Permo-Mesozoic rocks include several types of marble, graphitic schist, biotite schist, dolomite, quartzite and quartzitic schist. The Wolfendorn nappe consists of marble, quartzitic marble, metaarkose, quartzite, dark phyllite, metabreccia, dolomite, quartzitic schist and paragneiss. The Modereck nappe consists of several types of marble and phyllite, garnet/bearing schist, amphibolite, metagabbro, dolomite, quartzite, carbonatitic quartzite and arkose. The sequence of Glockner nappe in the studied area includes carbonatitic schist and phyllite, marble, greenschist, chloritic phyllite, serpentinite and dark phyllite.

The previous thermobarometric P-T estimates on the Alpine metamorphism in the studied region indicated higher-pressure metamorphism up to ~550 °C at 1.1 GPa for metapelites in

the Venediger cover and Subpenninic nappes (Selverstone et al., 1984; Selverstone, 1985; 1988; 1993) and 600 °C at 6-7 kbar for greenschists and amphibolites of the Penninic nappes (Schulz et al., 1995). In metapelites the garnet growth was associated with increasing temperature along a clockwise P-T-t loop showing initial increase in pressure followed by pressure decrease (Selverstone, 1985; Selverstone, 1993). The timing of garnet growth has been evaluated by Rb-Sr method indicating 35-30 Ma in Penninic nappes and 62-30 Ma in Subpenninic nappes (Christensen et al., 1994). On the other hand, more recent Sm-Nd dating from similar garnets indicates growth of garnets between 28 and 20 Ma (Pollington and Baxter, 2010). The metamorphic equilibration for the peak P-T conditions (Tauernkristallization) was estimated by Rb-Sr method to occur between 30 and 28 Ma (Inger and Cliff, 1994) and recently by U-Pb method on apatites at 37-34 Ma (Schneider et al., 2015). Rapid cooling and exhumation of the studied area started at ca. 20 Ma (von Blanckenburg et al., 1989; Fügenschuh et al., 1997; Scharf et al., 2013) or 31-29 Ma (Schneider et al., 2015).

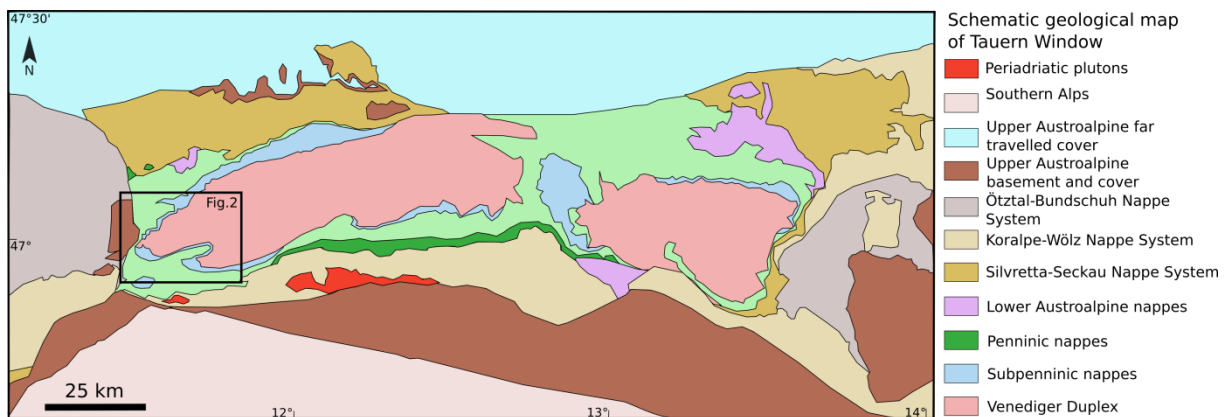


Fig. 1 Schematic map of Tauern Window within the realm of Eastern Alps, after Schmid et al. (2013). The rectangle shows studied area and extent of map in Figure 2a.

3 Structural record

Deformation record related to three main deformation events was distinguished in the studied area. The oldest deformation event D1 is associated with the development of amphibolite facies grade metamorphic foliation S1 dominating the entire studied region (Fig. 2a). This foliation (Fig. 3a) is penetrative in the metasediments, greenschists and metabasites of the Subpenninic and Penninic units and heterogeneously developed in the basement

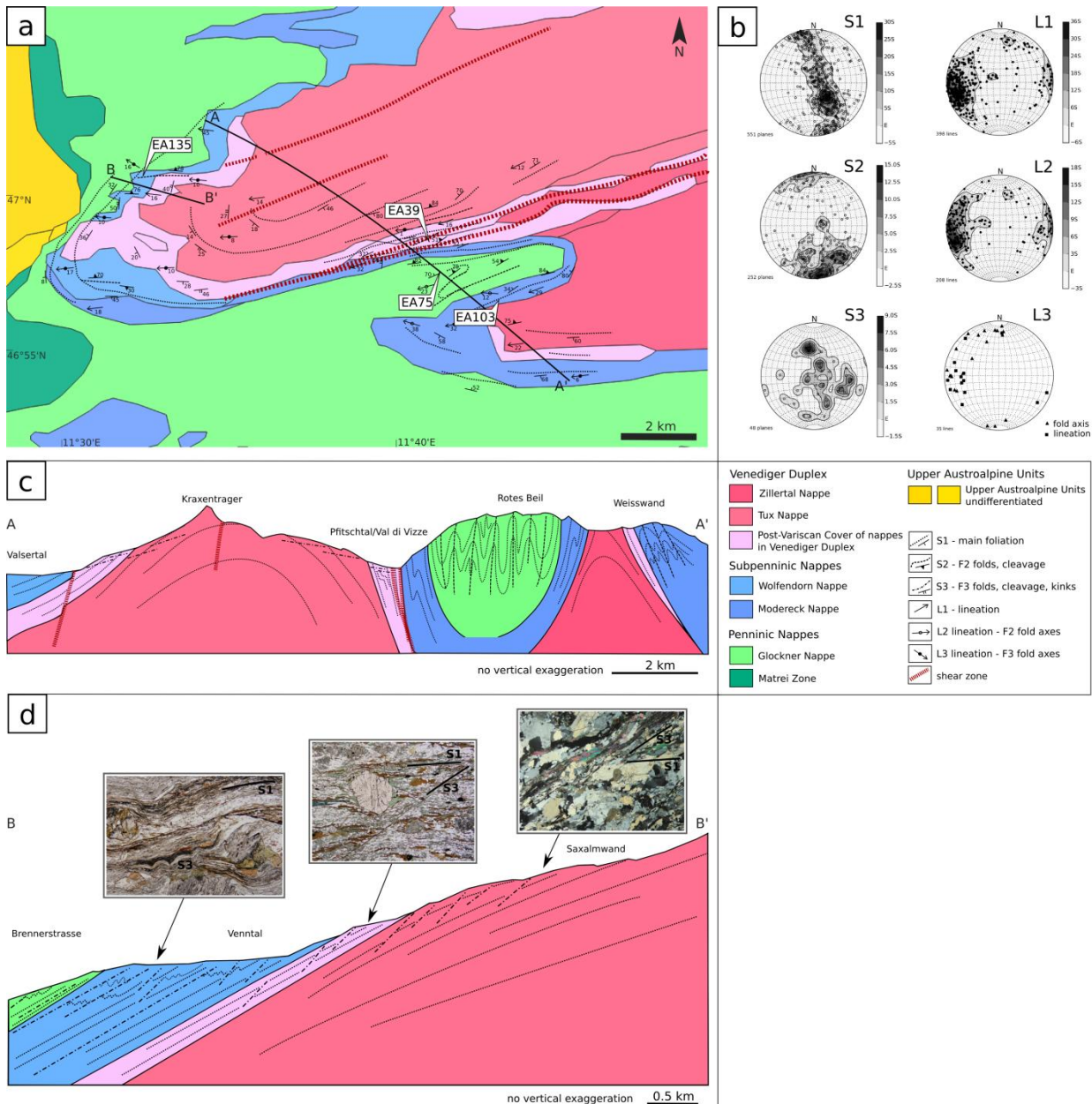


Fig. 2 a) Schematic geologic map of the studied area in westernmost part of Tauern Window. The structural record shows continuance of major fabrics S1 and S3, orientation of lineations as well as fold axes with major shear zones in the area (red). The location of idealized cross sections in c) and d) is depicted as AA' and BB'. b) The pole figures with data from studied area – S1: main foliation bearing L1 lineation, S2 represented mainly by fold axial planes of F2 folds, eventually cleavages, bearing L2 – fold axes or stretching foliation, and S3 cleavages or fold axial planes of F3 folds, bearing L3 – fold axes or striations. c) Idealized cross section AA' in the studied area in between Valser Tal (Austria) and Weisswand area (Italy). d) Cross section BB' in the Venntal area. Map and profile modified after Brandner et al. (2008) and Schmid et al. (2013) with insets of micrographs (II polarizers, width of view ~3 mm). The cross-sectional profiles show the relationship of three documented fabrics. The field data were analyzed and plotted using pySDB and plug-in readSDB (<http://petrol.natur.cuni.cz/~ondro>) for QGIS Desktop (www.qgis.org).

granitoids and it is subparallel to the lithological contacts (Fig. 2a). The S1 dips at shallow to steep angles to the NNW or SSE (Fig. 2b) mainly as a result of subsequent folding and doming during D2. S1 bears generally WSW-ENE trending stretching lineation L1 (Fig. 2b) defined by shape preferred orientation of quartzo-feldspathic aggregates and alignment of white mica.

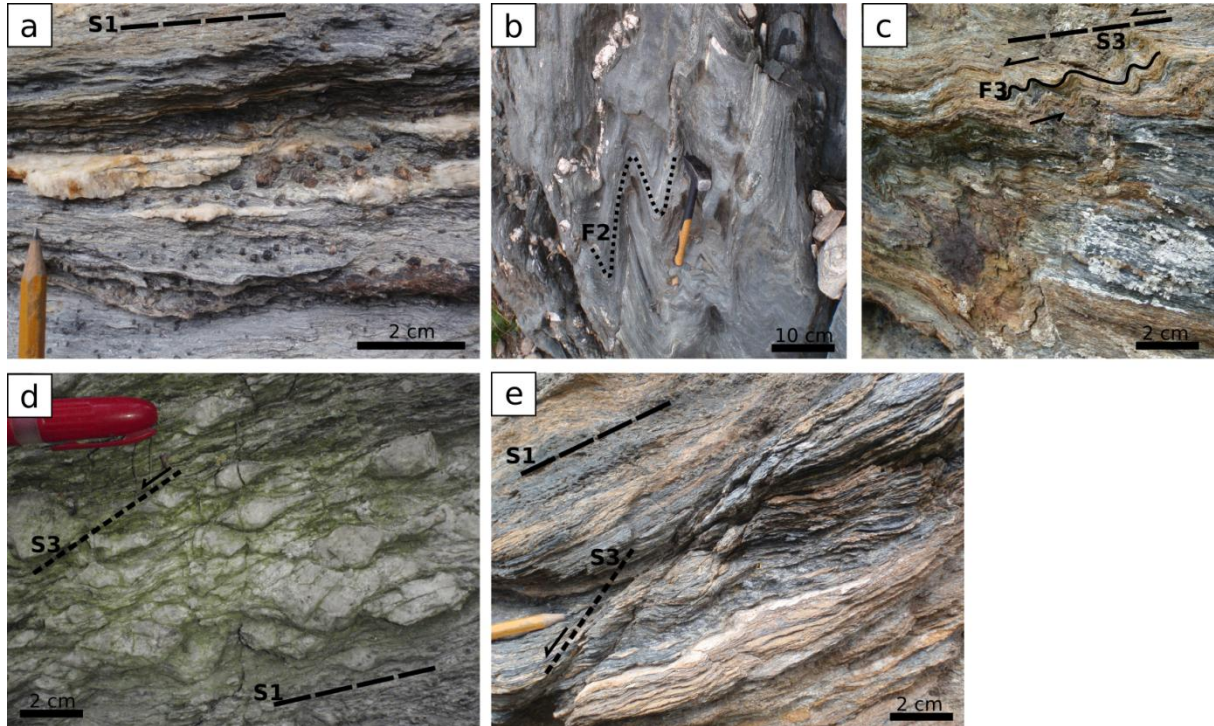


Fig. 3 Structural record within the studied area with shown trend and character of fabrics. a) Fabric S1 with abundant garnet of the Wolfendorn nappe in Venntal (locality EA135). b) F2 folds in the Penninic nappes in Filtuiden area (locality EA178). c) F3 folds in the schists of Modereck nappe the S3 fabric (locality EA99). d) Deformed Venediger basement orthogneiss close to the contact with cover sequences in Silltal (locality EA121) with foliation S1 and localized shears S3. e) Deformation in Wolfendorn nappe – S1 fabric crosscut by S3 cleavage (locality EA134 in Venntal). The GPS coordinate localization for localities is given in the Appendix.

The second deformation event is associated with the development of large scale folds F2 with subvertical WSW-ENE axial planes and axial planar cleavage of greenschist facies grade. The small scale tight folds (Fig. 3b) and cleavages are most profound in the synform of Penninic nappes between the nappes of Venediger basement (Fig. 2c). The fold axes L2 are subhorizontal and generally WSW-ENE trending (Fig. 2b).

The latest documented fabric S3 was identified mainly in the Venediger basement, cover and Subpenninic nappes in the westernmost part of the studied area (Fig. 2a). In the vicinity of the basement-cover contact, S3 is represented by discrete westward-dipping greenschist

facies cleavage which crosscuts S1 foliation in the form of S-C (S1-S3) fabrics (Fig. 2d). S3 bears west-plunging lineation L3 defined by alignment of white mica and quartz and the geometry of S-C fabrics shows consistent top-to-the-west kinematics (Fig. 3d, e). Away from the basement-cover contact towards the west the S1 becomes completely transposed/overprinted by S3 suggesting a formation of major detachment shear zone associated with D3 event. In addition, the strongly sheared schists of the Subpenninic nappes contain small scale folds F3 (Fig. 3c) with subhorizontal N-S trending fold axes, i.e. perpendicular to lineation L3, and westward vergence.

4 Petrography of studied rocks

In order to understand the relationship between deformation and metamorphism in the westernmost part of the Tauern Window, the representative lithologies from individual units/nappes were studied in detail. Our samples include orthogneiss from the Venediger basement (sampled in the vicinity of the overlying cover sequences), garnet-bearing schist from the Venediger cover, garnet-biotite schists and graphitic schists from the Subpenninic nappes, and greenschist and garnet-bearing micaschist from the Penninic nappes.

4.1 Venediger basement

The basement rocks are in the studied area mainly represented by deformed granitoids with well developed main foliation (Fig. 3d) that is defined by presence of plagioclase and K-feldspar porphyroclasts, muscovite, biotite and quartz aggregates with accessory tourmaline, zircon and monazite. These granitoids are deformed to orthogneisses close to the contact to the overlying nappes or to biotite-rich (\pm amphibole) schists that are found mainly close to or within the shear zones. In the orthogneisses in the vicinity to the cover sequences were observed S3 structures (Fig. 3d): cleavages or individual localized shears. These are crosscutting the main foliation S1 under acute angle and are mainly formed by greenschist-grade minerals such as biotite, muscovite and chlorite. At some places also synkinematic garnet is found in S1 fabric within rocks close to the contact to the cover sequences. In these orthogneisses only small amount of feldspar porphyroclasts and quartz aggregates is preserved, while the main part of the matrix is formed by fine grained recrystallized mixture of quartz and feldspar grains and biotite, muscovite and chlorite that define the S1 fabric (Fig. 4a). Garnets are overgrowing the S1 foliation and are typically small (up to 0.3 mm, Fig. 5a) with inclusions of quartz and muscovite. The biotite-rich schists are composed of quartz, K-feldspar, plagioclase, albite, biotite and muscovite and in some cases also chlorite and

amphibole. As accessory minerals are found apatite, zircon, ilmenite, titanite, epidote and iron oxides.

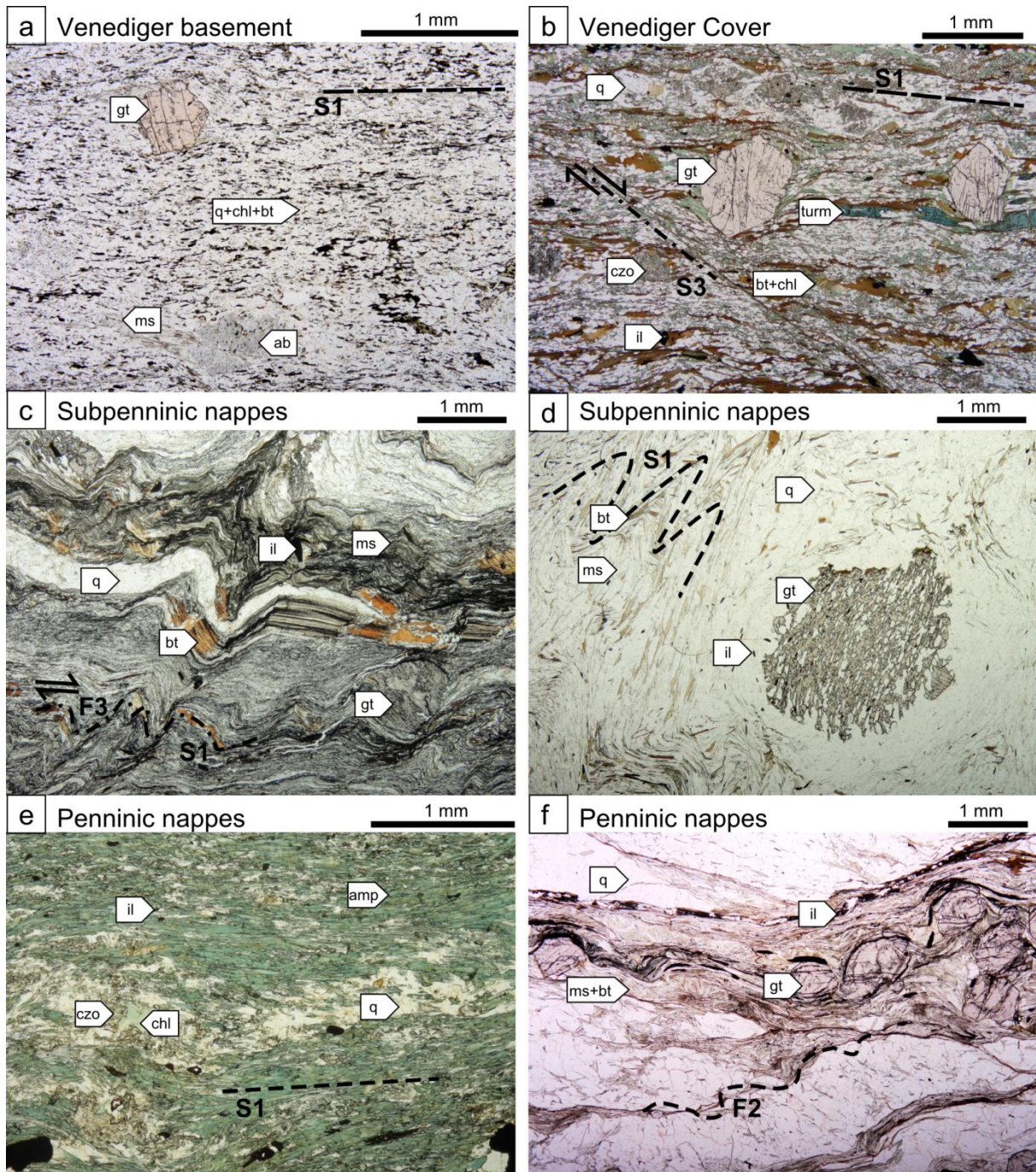


Fig. 4 Micrographs of studied lithologies (II polarizers) with traces of S1 – S3 fabrics. a) Orthogneiss from Venediger basement (sample EA84); b) biotite schist from Venediger cover (sample EA85); c) graphitic schist from Subpenninic Wolfendorn nappe (sample EA135C); d) garnet-bearing schist from Subpenninic Modereck nappe (sample EA103E); e) greenschist (also called prasinite) from Penninic nappes (sample EA77) and f) micaschist from Penninic nappes (sample EA75). Mineral abbreviations: ab – albite, amp - amphibole, bt - biotite, chl - chlorite, czo - clinozoisite, gt - garnet, il - ilmenite, ms - muscovite, q - quartz

4.2 Venediger cover

The Venediger cover biotite schists (Fig. 4b) were extensively studied because of the presence of metamorphic garnet that grows in the S1 fabric and is syn- to post-kinematic to S1 as documented by inclusion trails. S1 foliation is defined by flakes of biotite that is commonly replaced by chlorite (S3, Fig. 4b), muscovite and matrix of quartz, plagioclase, garnet, eventually amphibole (tschermakitic hornblende) and accessory zircon, ilmenite, apatite, iron oxides and monazite. The garnet is significantly larger (up to 3 mm; Fig. 5b) than the garnets found in the basement rocks. It contains abundant inclusions of quartz and ilmenite, eventually also muscovite. Where S3 cleavages (Fig. 4b) are present these are defined by biotite, muscovite and chlorite overgrowing the S1 fabric.

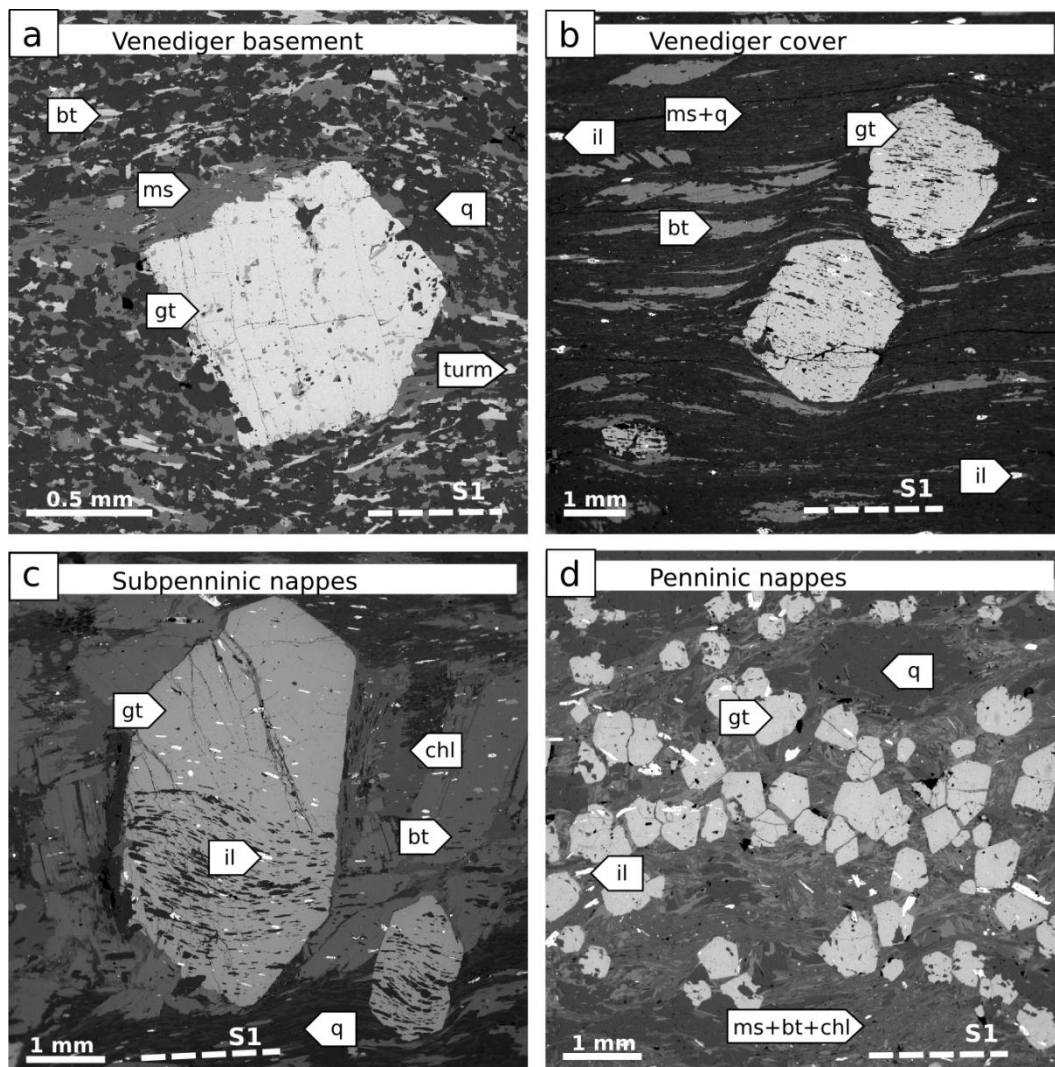


Fig. 5 Back scattered electron images of syn- to post-kinematic garnets within the main fabric S1: a) Venediger basement (sample EA84), b) Venediger cover (sample EA39), c) Subpenninic nappes – Modereck nappe (sample EA98), d) Penninic nappes (sample FIL). Mineral abbreviations: bt - biotite, chl - chlorite, gt - garnet, il - ilmenite, ms - muscovite, q - quartz, turm - tourmaline

4.3 Subpenninic nappes

The graphitic garnet-bearing schists in Wolfendorn nappe (Fig. 3a,e) are composed of quartz rich matrix with plagioclase and K-feldspar grains, muscovite and biotite flakes that define the S1/S3 fabric. Presence of graphite and garnet with graphitic inclusion trails in the S3 fabric indicate that the S1 fabric might have been reworked and parallelized into the S3 fabric (Fig. 3a). The quartz is dynamically recrystallized. Sometimes this fabric is crosscut by localized shears (Fig. 3e) or is folded into small F3 folds (Fig. 4c) that are formed in muscovite-rich layers and include garnets that formed during S1 growth. The garnets are large (up to 6 mm; Figs. 3a, 5c) syn- to post-kinematic (rotated) to the foliation with subhedral to euhedral shape and preserve abundant inclusion trails of graphite, in lesser amount also quartz, ilmenite and seldom muscovite. The biotite grains also preserve inclusions of graphite. Minor phases include dispersed graphite, ilmenite, apatite, zircon and monazite or allanite.

The garnet-bearing schists in Modereck nappe (Fig. 4d) contain porphyroblasts of K-feldspar and plagioclase, muscovite, garnet, epidote and biotite, that is in some cases replaced by chlorite. As accessory phases are found ilmenite, zircon, apatite and rutile. Garnets are quite large up to 15 mm in diameter with inclusions of quartz, epidote, ilmenite, chlorite, apatite and rutile. The garnets are syn- or post-metamorphic to the main foliation S1. Sometimes in the less competent lithologies the F3 folds (Fig. 3c) are found.

4.4 Penninic nappes

The most abundant lithologies within Penninic nappes are greenschists and calcschists. The greenschists (Fig. 4e) contain amphiboles with composition of actinolitic/magnesian-hornblende, chlorite, clinozoisite, albite, quartz, ilmenite and titanite. Calcschists contain mainly carbonate, quartz and muscovite with accessory ilmenite or rutile. The S1 fabric is folded by F2 tight folds (Fig. 3b).

The only lithology containing metamorphic garnets within Penninic nappes is micaschist (Fig. 4f). The S1 fabric is defined by quartz, biotite and muscovite. In the S1 fabric are abundant metamorphic garnets that are syn- to post-kinematic to the S1 fabric (Fig. 5d), locally are present small F2 folds pronounced mainly in muscovite-rich layers. Locally in the rock found chlorite and accessory rutile, ilmenite, zircon and monazite.

Lithology	Venediger Duplex basement: orthogneiss					Venediger Duplex basement: biotite schist from shear zone							Venediger Duplex cover: biotite schist		
	muscovite	biotite	K-feldspar	plagioclase	tourmaline	K-feldspar	plagioclase	muscovite	biotite	chlorite	epidote	amphibole	plagioclase	chlorite	muscovite
Sample	EA84 2 4	EA84 6	EA84 2 3	EA84 2 7	EA84 2 6	EA68 3	EA68 4	EA68 22	EA68 6	EA68 5	EA68 34	EA82A 11	EA192B 13	EA192B 6	EA192B 7
Wt.%															
SiO ₂	45.46	34.48	62.94	67.52	36.99	64.59	67.20	46.13	35.72	24.06	38.41	40.68	68.11	22.77	46.74
TiO ₂	0.68	2.43	0.00	0.00	0.30	0.00	0.00	0.13	2.30	0.13	0.10	0.38	0.00	0.00	0.00
Al ₂ O ₃	28.13	15.78	18.70	19.61	22.04	18.30	20.49	29.80	16.02	20.00	27.08	14.80	19.68	20.69	34.80
FeO	6.28	27.56	0.00	0.00	13.58	0.00	0.00	6.00	25.20	33.85	7.60	15.67	0.00	39.47	2.44
MnO	0.00	0.49	0.00	0.00	0.00	0.00	0.00	0.09	0.63	0.86	0.12	0.31	0.00	0.00	0.00
MgO	1.32	4.84	0.00	0.00	0.00	0.00	0.00	1.14	5.21	7.31	0.00	8.19	0.00	4.04	0.29
CaO	0.00	0.00	0.00	0.29	23.50	0.00	1.25	0.05	0.08	0.06	23.60	10.41	0.25	0.00	0.00
Na ₂ O	0.22	0.07	0.75	11.30	0.00	0.71	10.92	0.24	0.10	0.00	0.00	1.74	11.34	0.00	0.21
K ₂ O	10.72	9.52	15.07	0.06	0.00	16.09	0.09	11.06	9.74	0.00	0.00	0.38	0.07	0.00	10.22
F	0.00	0.00	0.00	0.00	0.00	0.00	0.00	0.27	0.28	0.00	0.00	0.00	0.00	0.00	0.00
Cl	0.00	0.00	0.00	0.00	0.00	0.24	0.00	0.00	0.06	0.00	0.00	0.00	0.00	0.00	0.00
Total	92.81	95.18	97.47	98.78	96.41	99.93	99.95	94.91	95.32	86.27	96.91	92.57	99.44	86.96	94.70
X Mg	0.27	0.24						0.44	0.27	0.28		0.48		0.15	0.17

Lithology	Wolfendorn nappe: graphitic schist				Modereck nappe: garnet bearing schist			Glockner nappe: micaschist			Glockner nappe: greenschist		
	muscovite	chlorite	K-feldspar	plagioclase	muscovite	chlorite	biotite	muscovite	chlorite	biotite	amphibole	plagioclase	clinozoisite
Sample	E135C 29	E135C 30	EA89C 43	EA89C 44	EA103E 3	EA103E 5	EA103E 4	FIL2 8	FIL2 3	FIL2 5	EA46 1	EA46 3	EA46 6
Wt.%													
SiO ₂	47.60	23.44	46.73	63.89	45.08	22.75	34.44	48.47	24.50	36.39	50.63	52.78	37.92
TiO ₂	0.34	0.00	0.45	0.00	0.25	0.00	1.71	0.36	0.00	1.36	0.09	0.00	0.02
Al ₂ O ₃	34.07	21.25	34.84	22.34	32.86	20.68	17.61	33.47	22.41	18.65	6.96	28.11	31.01
FeO	2.03	27.44	1.90	0.45	2.24	32.83	23.76	1.77	23.44	17.58	6.73	0.18	1.90
MnO	0.00	0.30	0.00	0.00	0.00	0.01	0.00	0.00	0.20	0.00	0.27	0.00	0.05
MgO	1.30	11.76	0.98	0.00	1.03	8.81	6.80	1.41	14.60	10.31	16.74	0.01	0.00
CaO	0.00	0.00	0.00	3.15	0.00	0.00	0.00	0.00	0.00	0.09	12.37	10.80	23.95
Na ₂ O	0.97	0.00	1.21	9.98	0.91	0.00	0.15	0.47	0.00	0.18	0.61	5.13	0.02
K ₂ O	9.47	0.00	9.17	0.00	9.69	0.00	8.79	9.95	0.00	8.85	0.02	0.03	0.00
F	0.00	0.00	0.00	0.00	0.00	0.00	0.00	0.00	0.00	0.00	0.00	0.00	0.00
Cl	0.00	0.00	0.00	0.00	0.00	0.00	0.00	0.00	0.00	0.00	0.00	0.00	0.00
Total	95.79	84.19	95.28	99.81	92.06	85.07	93.27	95.89	85.15	93.40	94.43	97.04	94.88
X Mg	0.57	0.43			0.45	0.32	0.32	0.59	0.53	0.51	0.82		

Tab. 1 Representative mineral microprobe analyses from selected lithologies. Note that garnet compositions can be found in Tab. 2.

5 Mineral chemistry

White micas that are found in rocks across the studied area, mostly defining S1, eventually S3 fabric have composition of muscovite with Si reaching 3.05-3.31 and $\text{XMg}_{\text{Fetot}}$ 0.17-0.64. Biotites in studied rocks reaches $\text{XMg}_{\text{Fetot}}$ 0.23-0.59, these are present in the S1 fabric or in Venediger cover across the S1 fabric crosscut by S3 fabric biotites. Chlorites in studied rocks are part of retrograde assemblage in S3 fabric mostly, sometimes alternate original S1 biotite, with $\text{XMg}_{\text{Fetot}}$ reaching 0.07-0.61. Epidotes have composition with XFe^{3+} reaching 0.65-1.00, sometimes close to allanite in composition. Feldspars are represented by matrix plagioclases with composition of albite Ab 90-97, oligoclase Ab 71-90 and in Penninic nappes also andesine and labradorite (Ab 25-70). Only in some schists in Modereck nappe are found K-feldspars with orthoclase content Or 82-95. The amphiboles from Penninic nappes and Venediger cover are actinolitic hornblendes or magnesio-hornblendes with Si reaching 6.28–7.34 and XMg 0.48-0.82. Representative chemical analyses of the rock-forming phases are in Table 1.

5.1 Garnet chemistry

Metamorphic garnets reveal compositional zoning (Fig.6) that differs for studied rock types and nappes (Fig.7). The garnets from Venediger basement and shear zones within basement are more grossular rich, garnets of Venediger cover, Subpenninic Wolfendorn nappe and Penninic nappes are richer in spessartine with a spread in almandine content, while garnets from Subpenninic Modereck nappe are richest in almandine.

In the orthogneiss of Venediger basement (Fig. 5a, 6a), the almandine rich garnets do not reveal significant compositional zoning with grossular (Grs) 35-37, almandine (Alm) 26-32, spessartine (Sps) 19-22, pyrope (Prp) 0-1 and XMg value that reaches from 0.01 - 0.03. Quite similar composition although slightly more grossular or almandine rich with more pronounced zoning have the garnets from shear zones within the basement with composition of Grs 45 → 51, Alm 39 → 46, Sps 4 → 26, Prp 1 → 2 and XMg from 0.01 – 0.03, that show increase of Fe while decrease of Ca. Other garnets differ from those found in basement with higher almandine and pronounced zoning.

Garnets from Venediger cover sequences (Fig. 5b, 6b) are almandine rich with variable content of Mn. The composition reaches from core towards the rims Alm 37-60 → 52-67 Grs 19-23 → 14-16, Sps 3-29 → 6-14, Prp 3-5 → 7-8 and XMg 0.07 – 0.11, thus the Fe and Mg content increases while Ca and Mn decreases. In the rim part the spessartine (Mn) component

slightly increase from 14 to 19 which is balanced by more significant decrease of Ca.

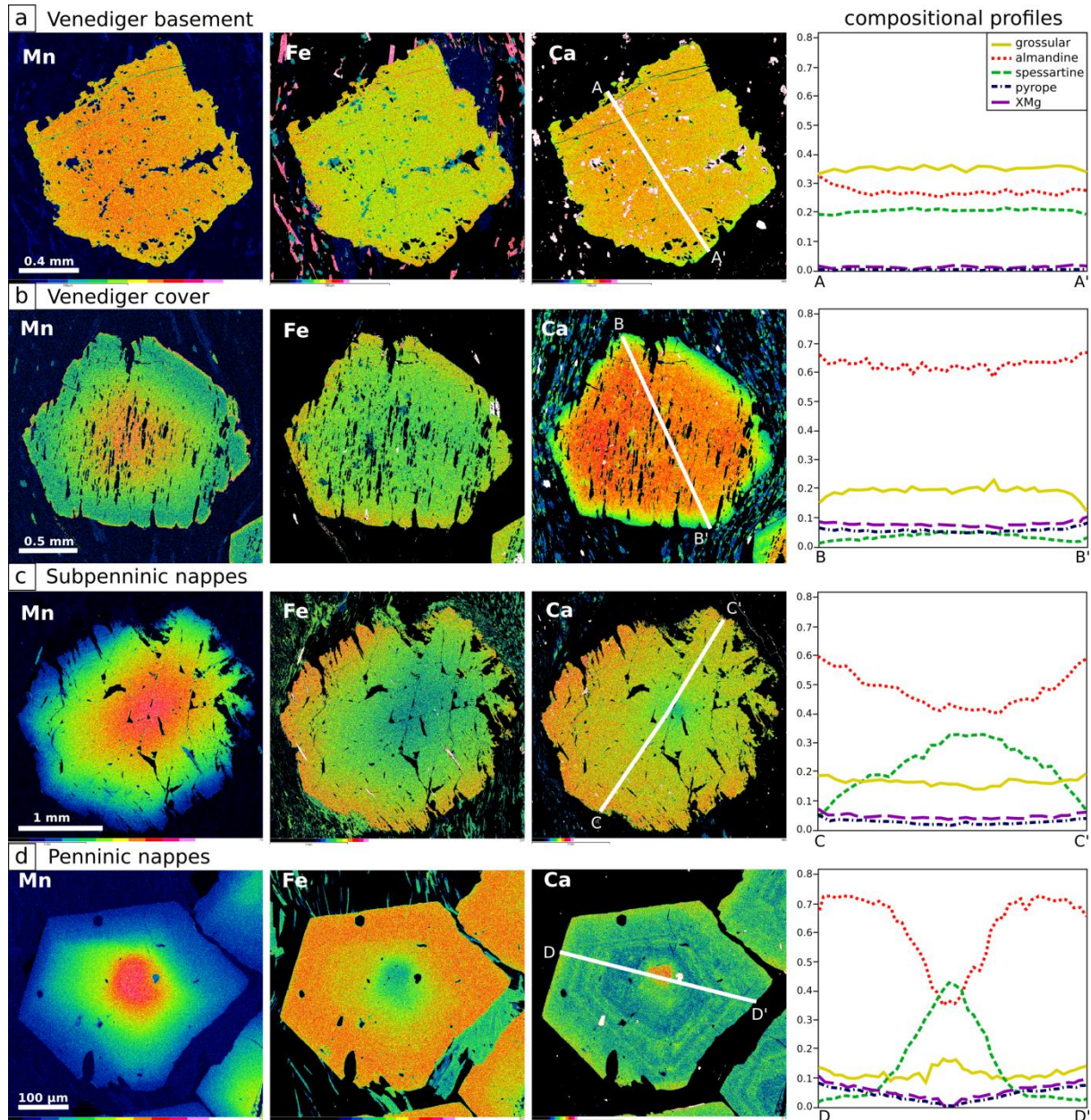


Fig. 6 Garnet compositional maps of manganese, iron and calcium for garnets from a) Venediger basement (EA84), b) Venediger cover (sample EA39), c) Subpenninic nappes (sample EA135C), d) Penninic nappes (sample FIL) and compositional profiles as located within maps of Ca. Compositional changes along the profile are plotted in almandine (yellow), grossular (red), pyrope (blue) and spessartine component (green) and X Mg (violet).

Garnets from Subpenninic nappes (Fig. 5c, 6c) are almandine rich with increase of Mg from core to rim, while decreasing Mn. The garnets within the Wolfendorn nappe show more pronounced zoning with significant increase of Fe content and decrease of Mn. The composition changes from core to rim Alm 41-46 → 60-63, Grs 14-15 → 16-19, Sps 26-33 → 5, Prp 2 → 5 with XMg 0.04 → 0.07. Garnets from Modereck nappe have not significant

zoning with composition Alm 61-70 → 67-68, Grs 10-20 → 13-18, Sps 7-12 → 0-2, Prp 2-3 → 7-10 and XMg 0.03-0.05 → 0.09-0.12 changing from core to rim.

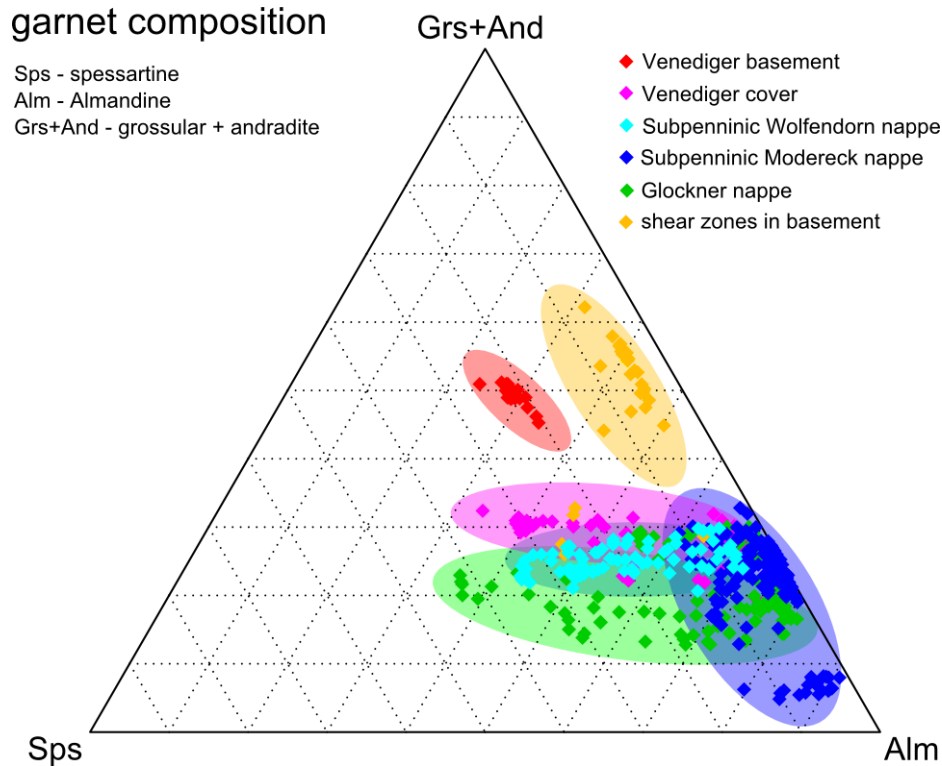


Fig. 7 Garnet composition in ternary diagram with compositions for garnets in Venediger basement (red), cover (pink) and shear zones (orange) within basement (yellow, see the geological map in Fig. 2a) and Subpenninic (light and dark blue) and Penninic nappes (green). The extent is given by garnet zoning as well as differences within lithologies.

Garnets found in Penninic nappes (Fig. 5d, 6d) show zoning close to the one of garnets in Wolfendorn nappe with increase of Fe and Mg from core to rim as well as decrease of Mn. The Ca content decreases from core, however show slight increase in garnet rim which is balanced by decrease in Fe and Mn. The garnets have mostly composition of spessartine, which abruptly changes to almandine. The change from core to rim is Alm 35-52 → 70-73, Sps 14-22 → 12-17, Grs 15-43 → 1-3, Prp 0-4 → 6-10 with XMg 0.00-0.06 → 0.03-0.10.

Garnets from shear zones that are found within basement reveal the same zoning as other garnets. In their composition are close to garnets from Venediger cover rocks. The composition varies from core to rim Alm 35 → 45, Grs 54 → 45, Sps 5, Prp 1, XMg 0.02 → 0.03.

Lithology	Venediger Duplex basement		Venediger Duplex basement		Venediger Duplex cover		Modereck nappe		Wolfendorn nappe		Glockner nappe		
	orthogneiss		biotite schist in shear zone		biotite schist		schist		graphitic schist		micaschist		
	core	rim	core	rim	core	rim	core	rim	core	rim	core	rim	rim
Sample	EA84	EA84	EA203B	EA203B	EA39	EA39	EA103E	EA103E	EA135C	EA135C	EA75	EA75	EA75
Wt. %													
SiO ₂	36.47	36.77	36.91	37.11	36.46	36.39	35.84	36.02	35.95	36.24	35.86	35.99	35.13
TiO ₂	0.18	0.08	0.15	0.08	0.12	0.04	0.12	0.03	0.14	0.03	0.00	0.00	0.00
Al ₂ O ₃	20.10	20.24	20.58	20.74	20.55	20.69	20.28	20.59	20.51	20.70	20.35	20.51	19.94
Fe ₂ O ₃	4.51	3.54	1.74	0.99	2.54	2.31	3.43	3.22	2.05	2.99	1.32	2.31	2.91
FeO	14.08	16.37	24.96	30.56	28.94	32.15	30.41	33.99	19.90	29.47	16.61	33.79	30.88
MnO	11.08	9.89	7.07	0.55	2.01	1.59	3.47	0.00	15.02	2.46	18.93	1.66	1.06
MgO	0.17	0.21	0.96	2.20	1.44	2.19	0.53	1.38	0.49	1.28	0.00	1.44	1.94
CaO	14.18	13.49	8.15	7.35	7.94	4.60	6.31	5.19	5.56	7.12	5.54	3.91	5.15
Total	100.77	100.58	100.51	99.57	100.00	99.96	100.39	100.42	99.62	100.29	98.61	99.62	97.02
Si	2.91	2.94	2.96	2.98	2.94	2.94	2.92	2.92	2.94	2.92	2.97	2.94	2.93
Ti	0.01	0.00	0.01	0.00	0.01	0.00	0.01	0.00	0.01	0.00	0.00	0.00	0.00
Al	1.89	1.91	1.95	1.97	1.95	1.97	1.94	1.97	1.98	1.97	1.98	1.98	1.96
Fe ³⁺	0.27	0.21	0.11	0.06	0.15	0.14	0.21	0.20	0.13	0.18	0.08	0.14	0.18
Fe ²⁺	0.94	1.09	1.68	2.05	1.95	2.17	2.07	2.30	1.36	1.99	1.15	2.31	2.15
Mn	0.75	0.67	0.48	0.04	0.14	0.11	0.24	0.00	1.04	0.17	1.33	0.11	0.08
Mg	0.02	0.02	0.12	0.26	0.17	0.26	0.06	0.17	0.06	0.15	0.00	0.18	0.24
Ca	1.21	1.15	0.70	0.63	0.69	0.40	0.55	0.45	0.49	0.62	0.49	0.34	0.46
Total	8.00	8.00	8.00	8.00	8.00	8.00	8.00	8.00	8.00	8.00	8.00	8.00	8.00
X Andradite	0.14	0.11	0.05	0.03	0.05	0.08	0.11	0.10	0.06	0.09	0.04	0.07	0.09
X Pyrope	0.01	0.01	0.04	0.08	0.60	0.67	0.02	0.05	0.02	0.05	0.00	0.05	0.07
X Almandine	0.27	0.32	0.53	0.66	0.21	0.12	0.61	0.69	0.42	0.60	0.37	0.71	0.65
X Grossular	0.35	0.34	0.22	0.20	0.04	0.03	0.16	0.13	0.15	0.19	0.16	0.11	0.14
X Spessartine	0.21	0.20	0.15	0.01	0.98	0.98	0.07	0.00	0.32	0.05	0.42	0.04	0.02
X Mg	0.02	0.02	0.06	0.11	0.08	0.11	0.03	0.07	0.04	0.07	0.00	0.07	0.10

Tab. 2 Representative garnet microprobe analyses from selected lithologies and respective nappes. Chemical analyses and compositional maps of selected minerals were carried out using the EDS detector X-Max 50 (Oxford Instruments) attached to the scanning electron microscope TESCAN Vega at the Institute of Petrology and Structural Geology, Charles University in Prague. The analyses and compositional maps were obtained with accelerating potential 15 kV and beam current 1 nA and 5nA, respectively. The chemical analyses were normalized to 12 oxygens for garnet, 14 oxygens for chlorite, 11 oxygens for white mica, 23 oxygens for amphibole, 3 oxygens for feldspar, 12.5 oxygens for clinozoisite - epidote (see Table 1). XMg is defined as $\text{XMg} = \text{Mg}/(\text{Mg} + \text{Fe}_{\text{tot}})$. Chemical analyses of garnet were plotted using the GeoChemicalData toolkit (GCDkit, Janoušek et al., 2006).

6 P-T conditions

The P-T pseudosections and compositional isopleths were calculated using the *Perple_X* thermodynamic software (Connolly, 2005; version 6.6.8) with the internally consistent thermodynamic data set of Holland and Powell (1998: version 2004). The preferred system for calculation was MnO - Na₂O - CaO - K₂O - FeO - MgO - Al₂O₃ - SiO₂ - H₂O (MnCKFMASH) with water in excess. The whole rock compositions used to calculate the P-T pseudosections are presented in Table 3. Titanium was not used in the calculation as it is present in very small amounts in the garnets as well as in the accessory phases, however the model for garnet Ti does not exist and the computation did not succeed.

The resulting pseudosections (Fig. 8) have been calculated with following solid solution models for biotite (Tajčmanová et al., 2009), chlorite (extended from Holland et al., 1998), white mica (Coggon and Holland, 2002; Auzanneau et al., 2010), plagioclase (Newton et al., 1980), garnet (Holland and Powell, 1998), clinopyroxene (Holland and Powell, 1996), chloritoid (Holland and Powell, 1998), stilpnomelane (Massonne and Willner, 2008) and staurolite (Holland and Powell, 1998). The results from *Perple_X* thermodynamic modelling were plotted using *pyWerami*.

The estimates on metamorphic conditions of garnet-bearing rocks were calculated for the Venediger cover (Fig. 8a), Subpenninic (Figs. 8b,c) and Penninic nappes (Fig. 8d). The deformation-crystallization relations in these rocks clearly show syn- to post-kinematic growth of garnet with respect to the main metamorphic foliation S1. To obtain more accurate P-T estimates for individual samples, the compositional isopleths of XMg and grossular component in garnet were plotted into each calculated pseudosection. The analysed garnet core and rim compositions were then used to characterize the P-T path related to garnet growth (Fig. 8). Because the isopleths for XMg and grossular component in the pseudosection calculated for the Penninic nappes are temperature dependent and subparallel, the pressure estimate was obtained by using the silica content in white mica.

In the resulting P-T pseudosection for sample from Venediger cover biotite schist (Fig. 8a), the observed equilibrium assemblage biotite, muscovite, garnet, quartz, plagioclase and chlorite with accessory zircon, ilmenite and apatite corresponds to a stability field ranging between 460-580 °C and spread above and below the modelled pressure of 3-9 kbar. This stability field is limited by the disappearance of chlorite towards higher temperatures, by the occurrence of clinozoisite towards lower temperatures and by disappearance of garnet towards

lower temperatures and lower pressures. The modelled compositional isopleths for grossular and XMg crosscut in the stability field with Grs21 and XMg 0.07 for the composition of garnet core and in garnet rim Grs12 and XMg 0.11. Based on the pseudosection the P-T conditions documented by garnet growth reaches from 515 °C and 5.6 kbar to 565 °C and 6.7 kbar for the garnet rim composition.

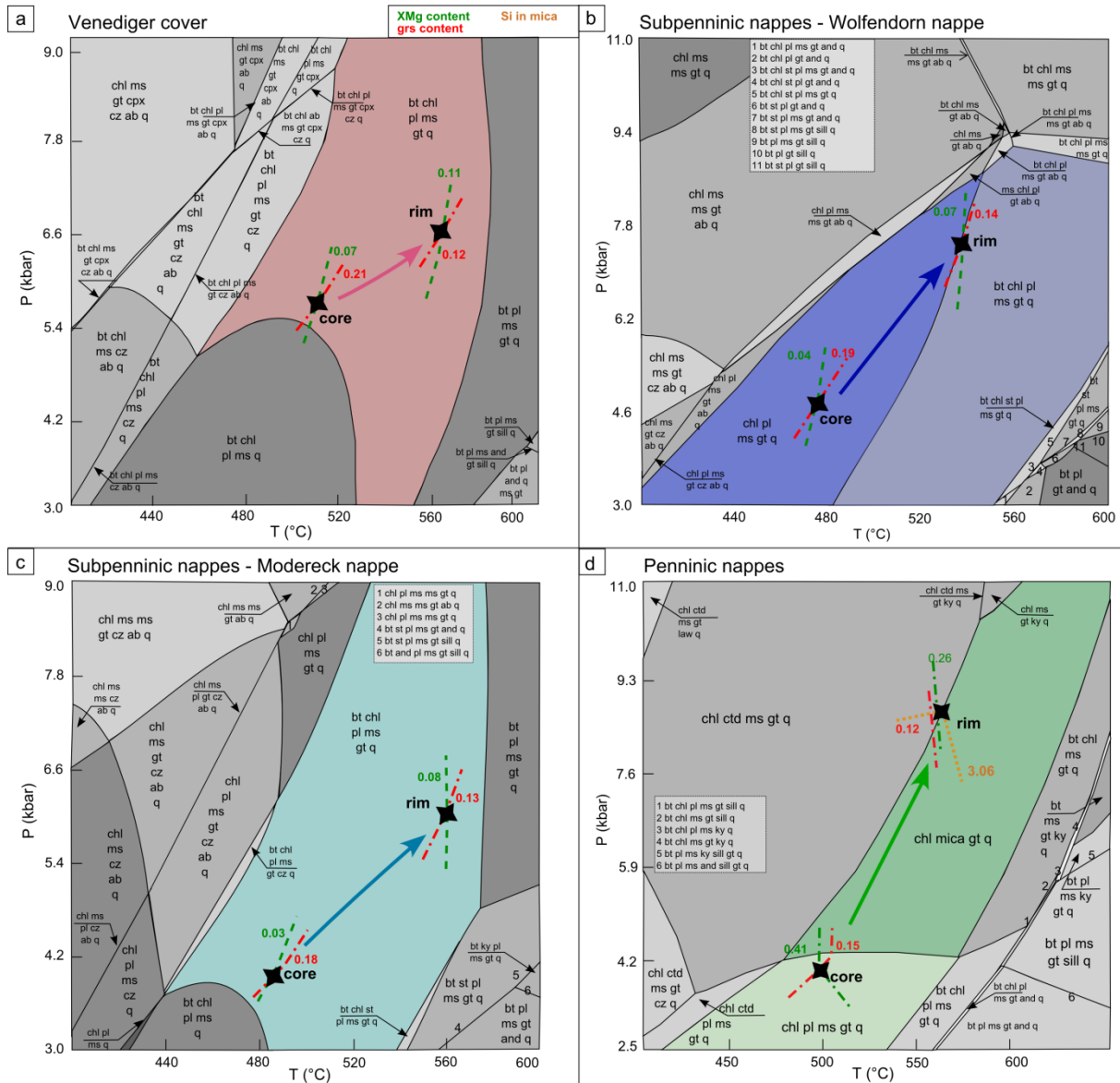


Fig. 8 Resulting P-T pseudosections with modeled conditions of garnet growth within a) Venediger cover biotite schist (sample EA39), b) Wolfendorn nappe schist (sample EA135C), c) Modereck nappe schist (sample EA103), d) Penninic nappes micaschist (sample EA75). The arrows show the presumed prograde path of garnet growth estimated by representative isopleths of XMg content and grossular component in garnet and Si in muscovite (in d). Rock analyses used for P-T pseudosection calculation can be found in Table 3.

In the schist from Subpenninic Wolfendorn nappe (Fig. 8b) the equilibrium assemblage biotite, muscovite, plagioclase, garnet, quartz and chlorite with accessory ilmenite, apatite, zircon, allanite, that corresponds to stability field ranging between 480-550 °C and from below 3 up to 9 kbar. This stability field is limited towards lower temperature with disappearance of biotite, towards higher temperatures by appearance of staurolite and towards higher pressures by appearance of albite or second white mica. The stability field of muscovite, plagioclase, garnet, quartz and chlorite is modelled for the composition of garnet core in 400-535 °C and below modelled 3 kbar and up to 8.6 kbar. The stability field is limited by appearance of biotite towards higher pressures and by appearance of albite and second white mica towards lower temperatures. The modelled compositional isopleths crosscut in the biotite-lacking stability field for garnet core composition with grossular content Grs19 and XMg 0.04 and in the biotite-containing stability field for rim composition of Grs14 and XMg 0.07. P-T conditions for garnet growth correspond to 475 °C and 4.7 kbar for core composition and 540 °C and 7.5 kbar for rim composition.

The sample from Subpenninic Modereck nappe schist (Fig. 8c) contains assemblage of biotite, muscovite, plagioclase, garnet, quartz and chlorite with accessory ilmenite, apatite and zircon, which corresponds to modelled stability field within 440-570 °C and slightly above and below modelled 3-9 kbar. This stability field is limited by disappearance of chlorite towards higher temperatures, by disappearance of biotite towards lower temperatures and higher pressures, by appearance of clinozoisite towards lower temperatures and by disappearance of garnet towards lower temperatures and lower pressures. Compositional isopleths for garnet core and rim content of grossular and XMg crosscut in the stability field. The core compositions of Grs18 and XMg 0.03 correspond to 485 °C and 4.0 kbar, while rim composition of Grs13 and XMg 0.08 corresponds to P-T conditions of 560 °C and 6.0 kbar.

Micaschist from Penninic nappes (Fig. 8d) has a stable assemblage of muscovite, chlorite, garnet and quartz, with accessory rutile, ilmenite, zircon and monazite, that corresponds to stability field at 475-700 °C and 4.2-11 kbar for modelled 400-700 and 3-11 kbar. The stability field is limited by appearance of biotite towards higher pressures, by appearance of chloritoid towards lower temperatures and by appearance of plagioclase towards lower pressures. The modelled isopleths for garnet core composition crosscut in the lower pressure stability field of muscovite, plagioclase, garnet, chlorite and quartz that is limited by appearance of chloritoid towards lower temperature, by appearance of biotite towards higher temperature and by disappearance of plagioclase towards higher pressure which extends from

420-555 °C and below 3 up to 4.2 kbar. The garnet core composition with Grs15 and XMg 0.41 refer to 500 °C and 3.8 kbar. The garnet isopleths for grossular and XMg content in garnet rim are in the stability field without plagioclase parallel and temperature dependent within this field and do not cross cut each other, the Si content in white mica was used to estimate the pressure. The garnet rim composition of Grs12, XMg 0.26 and Si in white mica 3.06 gave the P-T conditions of 560 °C and 8.7 kbar at the boundary towards the lower temperature field containing chloritoid. However chloritoid was never observed in studied samples.

Garnet growth reveals prograde metamorphic conditions in all studied samples. The later retrogression is represented by presence of late chlorite or chloritized biotite.

Lithology	Venediger Duplex cover	Wolfendorn nappe	Modereck nappe	Glockner nappe
	biotite schist	graphitic schist	garnet bearing schist	micaschist
Sample	EA39	EA135	EA98	EA75
SiO ₂	68.54	65.83	48.77	72.13
TiO ₂	0.80	0.00	1.18	0.60
Al ₂ O ₃	16.36	16.52	22.93	14.10
FeO	4.85	9.56	17.80	5.84
MnO	0.08	0.85	0.46	1.33
MgO	2.04	2.96	1.34	2.76
CaO	1.32	0.63	3.02	0.39
Na ₂ O	2.37	0.97	1.93	0.20
K ₂ O	3.63	2.67	2.58	2.67
Total	100.00	100.00	100.00	100.00

Tab. 3 Whole rock analyses of selected lithologies used for thermodynamic modelling in Perple_X. For details see text, for results see Fig. 8. Compositions were obtained by the wet chemistry method in laboratories of the Czech Geological Survey in Prague. The relative 2σ uncertainties from the analyzed oxides were better than 1 % (SiO₂), 2 % (FeO), 5 % (Al₂O₃, K₂O, Na₂O), 7 % (TiO₂, MnO, CaO), 6 % (MgO) and 10 % (Fe₂O₃, P₂O₅). Several effective bulk rock analyses were obtained from thin sections by area scanning electron microscopy using TESCAN Vega at the Institute of Petrology and Structural Geology, Charles University in Prague.

7 Discussion

The tectonic evolution within the Tauern Window comprises five distinct events (Schmid et al., 2013) that can be more or less traced in different parts of the window. The first phase is assigned to the subduction of Piemont-Liguria ocean and accretion of oceanic relics (D1; in the studied area might have affected Glockner nappe system), followed by subduction of Valais ocean and most distal parts of the European margin (D2; Subpenninic Modereck nappe system), followed by exhumation of high-pressure units and by accretion of European crust (D3), formation of Venediger Duplex (D4) and the Barrovian equilibration and by indentation, doming and exhumation of the post-Variscan series (D5). The exhumation is ascribed to orogen-parallel extension triggered by indentation by Southern Alps (Scharf et al., 2013) and by Pannonian extension that allowed for doming and lateral extrusion (Ratschbacher, 1991) or to gravitational collapse (Rosenberg et al., 2007). The dating of exhumation was discussed by many authors, the onset of the exhumation is expected at about 21 Ma in the area of Brenner fault (Fügenschuh, 1997) however parts of Tauern Window might have been affected by exhumation earlier (Cliff et al., 1985) where significantly contributed erosion (Schmid et al., 2013; Schneider et al., 2015).

The studied area in westernmost part of Tauern Window includes three deformation stages that were documented during field work. The most prominent deformation stage is D1 that forms the main fabric S1, found across the studied area parallel to lithological contacts. In between the Venediger basement nappes this fabric is intensively folded by D2 folding, that forms tight folds with steep dipping axial planes and E-W trending axes. Mostly in the northwestern part of the studied area the S1 foliation is crosscut by cleavage or individual shears S3, forming S-C fabrics, or affected by tiny westward folds. The hereby described phase D1 is similar to the Alpine D4 phase (~29 Ma) of Schmid et al. (2013) and Scharf et al. (2013). The phase is in these works connected to the formation of Venediger Duplex when European plate breaks off and Barrovian type metamorphism (Tauernkrystallization) takes place. The here described phases D2-D3 correspond to their phase D5 (~17 Ma) that forms as a response to the subduction of Adriatic slab by indentation, doming and lateral escape (Schmid et al., 2013, Scharf et al., 2013).

The thermodynamic modelling gave us the prograde metamorphic path for all the studied garnets nevertheless the nappe position and lithology (Fig. 9a). The metamorphic conditions increases from ~460 °C to ~550 °C and from ~4 to ~9 kbar and are not far away from the

conditions published by Selverstone et al. (1985) in some parts of her metamorphic path. Christensen et al. (1994) followed this work and described the growth of these garnets with decreasing pressure as well. The main difference is that our observation reveals the prograde instead of retrograde growth of these garnets. However, our data are in concordance with thermobarometry results obtained from amphibolites and greenschists from Penninic nappes in the studied area published by Schulz et al. (1995), that show increase in P-T conditions to 600 °C and 6-7 kbar followed by rapid exhumation and cooling. The correlation of prograde garnets with tectonic is possible because of the growth relationship of garnet and the fabrics (Fig. 9b). The prograde garnets are syn- to post-kinematic with respect to S1 fabric as documented by rotated or straight inclusion trails where these grow in E-W extensional – N-S constrictional regime. In Subpenninic and Penninic nappes these garnets can be found in the sequences folded by D2 where the fabric is shortened in N-S direction and extended vertically. Garnets are also preserved in rocks where the S3 fabric is pronounced by presence of cleavage or shearing (Fig. 9b) in N-S constrictional – E-W extensional regime.

Moreover the garnets from the Penninic nappes are similar to the garnets from blueschist facies metapelites from Iberian Massif studied by Carmona-Lopez et al. (2013) where the different zoning in garnets were described from two different nappe positions (Lower and Upper metapelites) that are similar to the Subpenninic (Lower Schieferhülle) and Penninic nappes (Upper Schieferhülle) in Tauern Window. The garnets show subduction-related prograde metamorphism at significantly higher pressures that is followed by rapid exhumation which is in overall agreement with our observations.

The observation of garnets that are syn- to post-kinematic with respect to S1 and that grow under prograde conditions, allows us to interpret the S1 fabric as being formed during the nappe stacking that forms the flow of the basement nappes (Fig. 9c left) within the regional E-W extension and thus flat lying foliation within the Venediger Duplex that bears E-W trending lineation parallel to the stretching of the Venediger basement under the load of the overlying nappes. This S1 fabric is bearing metamorphic garnets with prograde evolution that documents these increased P-T conditions during nappe stacking and flattening. The N-S shortening causes folding of nappe stack (Fig. 9c right) that is expressed by presence of the tight folds with E-W sub-horizontal fold axes and steepening of the S1 fabric. The shortening induces subsequent exhumation of basement nappes within the E-W extension that produces the steep C fabric of S-C geometries mainly in the western part of the studied area through the progressive development of detachment and faulting together with folding (Manktelow and

Pavlis, 1994). The occurrence of S-C fabrics is not connected to single deformation event, thus these are kinematically unrelated and refer to two deformation events that have co-parallel fabrics. The situation in Tauern Window is similar to the exhumation of orogen-parallel dome Central West Carpathians (Jeřábek et al., 2012).

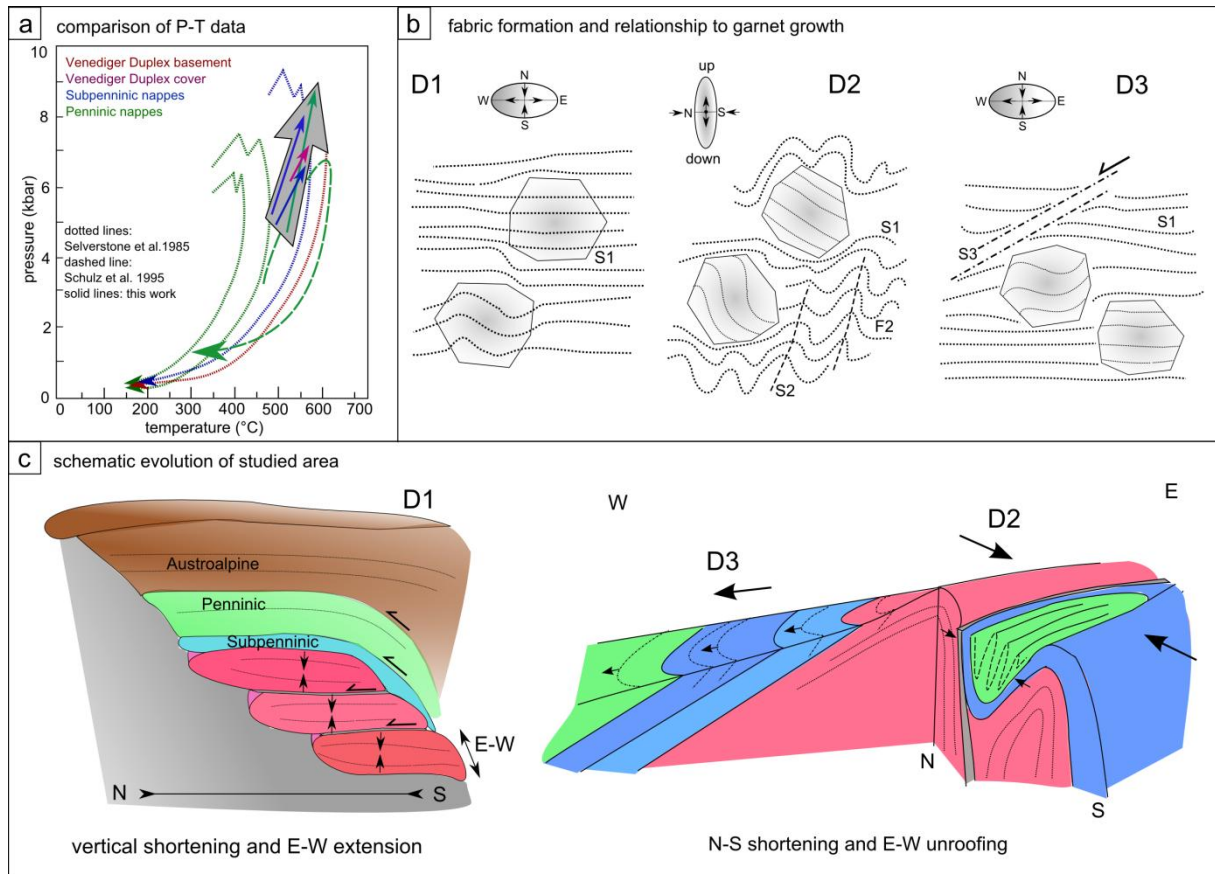


Fig. 9 a) Comparison of published P-T estimates (from Selverstone, 1985 and Schulz et al., 1995; dotted and dashed arrows respectively) and data obtained by thermodynamic modelling from this work (solid arrows) according to the nappe position (red – Venediger basement, violet – Venediger cover rocks, blue - Subpenninic nappes, green – Penninic nappes). b) The evolution of fabrics in studied area and the stress orientation documented on deformation ellipsoids: during D1 deformation phase the S1 fabric is formed with syn- to post-kinematic garnet with the N-S shortening and E-W stretching, that bears significant trails of the S1 fabric, in the D2 phase this fabric might be overprinted by folding as a result of N-S shortening, in the D3 phase the local shears and cleavages are formed as a consequence of E-W stretching and unroofing of the basement rocks. c) Idealized evolution of the studied area. The first deformational stage is related to nappe stacking that causes shortening and E-W stretching of the Venediger basement nappe stack, that is later steepened by N-S shortening (D2) and subsequent folding that causes escape of Subpenninic and Penninic nappes towards W (D3).

8 Conclusions

The westernmost part of Tauern Window represents an area that has undergone two separate orogen-parallel extensions. These are revealed by the combination of detail structure description, relationships of mineral assemblages and structures, i.e. crystallization-deformation relations and thermodynamic modelling. The first orogen-parallel extension connected to the nappe stacking formed the main flat foliation with prograde syn-to post-kinematic garnets that grew at ~460 - 560 °C and ~4 - 9 kbar. This fabric was steepened during N-S shortening, that represents the second phase, that induced the second E-W orogen-parallel extension and exhumation of the Tauern Window basement rocks, formation of the C fabric and in the metamorphic record is represented by occurrence of greenschist facies minerals. The formation of co-parallel fabrics resulted in presence of kinematically discontinuous S-C fabric.

Acknowledgement

This work was supported by Charles University Grant Agency Project No. 13702/2014.

Appendix: GPS coordinates of selected localities

Locality	Geological setting	GPS coordinates		Elevation (m)
		Latitude (°N)	Longitude (°E)	
EA39	Venediger cover	46.98425	11.65184	1824
EA46	Glockner nappes	47.01291	11.71792	1823
EA68	Venediger basement	46.99794	11.60473	2378
EA75	Glockner nappes	46.97507	11.66216	1986
EA77	Glockner nappes	46.97246	11.66752	2113
EA82	Venediger cover	47.01270	11.54934	1759
EA84	Venediger basement	47.01313	11.54824	1795
EA85	Venediger cover	47.01363	11.54719	1726
EA89	Wolfendorn nappe	47.01565	11.53677	1611
EA98	Modereck nappe	46.96188	11.69618	2358
EA103	Modereck nappe	46.97072	11.72314	3350
EA134	Wolfendorn nappe	47.01505	11.52846	1527
EA135	Wolfendorn nappe	47.00562	11.52695	1500
EA192	Venediger cover	46.98033	11.62859	1590
EA203	Glockner nappes	46.98245	11.71255	2586
FIL	Glockner nappes	46.97937	11.68114	ca. 2100

References

- Agard, P., Augier, R., Monié, P. (2011). Shear band formation and strain localization on a regional scale: Evidence from anisotropic rocks below a major detachment (Betic Cordilleras, Spain). *Journal of Structural Geology*, 33(2), 114-131.
- Behrmann, J.H. (1988). Crustal-scale extension in a convergent orogen: the Sterzing-Steinach mylonite zone in the Eastern Alps. *Geodinamica Acta*, 2(2), 63-73.
- Behrmann, J.H., Frisch, W. (1990). Sinistral ductile shearing associated with metamorphic decompression in the Tauern Window, Eastern Alps. *Jahrbuch der Geologischen Bundesanstalt Wien*, 133(2), 135-146.
- Berthé, D., Choukroune, P., Jegouzo, P. (1979). Orthogneiss, mylonite and noncoaxial deformation of granites: the example of the South Armorican Shear Zone. *Journal of Structural Geology* 1, 31-42.
- Bertrand, A., Rosenberg, C., Garcia, S. (2015). Fault slip analysis and late exhumation of the Tauern Window, Eastern Alps. *Tectonophysics*, 649, 1-17.
- Brandner, R., Reiter, F., Töchterle, A. (2008). Überblick zu den Ergebnissen der geologischen Vorerkundung für den Brenner-Basistunnel. *Geo Alp*, 5, 165-174.
- Bukovská, Z., Jeřábek, P., Lexa, O., Konopásek, J., Janák, M., Košler, J. (2013). Kinematically unrelated C—S fabrics: an example of extensional shear band cleavage from the Veporic Unit (Western Carpathians). *Geologica Carpathica*, 64(2), 103-116.
- Christensen, J.N., Selverstone, J., Rosenfeld, J.L., DePaolo, D.J. (1994). Correlation by Rb-Sr geochronology of garnet growth histories from different structural levels within the Tauern Window, Eastern Alps. *Contributions to Mineralogy and Petrology*, 118(1), 1-12.
- Cliff, R. A., Droop, G.T.R., Rex, D.C. (1985). Alpine metamorphism in the south-east Tauern Window, Austria: 2. Rates of heating, cooling and uplift. *Journal of metamorphic Geology*, 3(4), 403-415.
- Coggon, R., Holland, T.J.B. (2002). Mixing properties of phengitic micas and revised garnet-phengite thermobarometers. *Journal of Metamorphic Geology* 20:683-96.
- Connolly, J.A.D. (2005). Computation of phase equilibria by linear programming: A tool for geodynamic modeling and its application to subduction zone decarbonation. *Earth and Planetary Science Letters* 236:524-541.
- Frisch, W. (1974). Die stratigraphisch-tektonische Gliederung der Schieferhülle und die Entwicklung des penninischen Raumes im westlichen Tauernfenster (Gebiet Brenner-Gerlospaß). *Mitt. Geol. Ges. Wien*, 66(67), 9-20.
- Frisch, W. (1980). Tectonics of the western Tauern Window. *Mitteilungen der Österreichischen Geologischen Gesellschaft*, 71(72), 65-71.
- Frisch, W., Dunkl, I., Kuhlemann, J. (2000). Post-collisional orogen-parallel large-scale

extension in the Eastern Alps. *Tectonophysics*, 327(3), 239-265.

Fügenschuh, B., Seward, D., Mancktelow, N. (1997). Exhumation in a convergent orogen: the western Tauern window. *Terra Nova*, 9(5-6), 213-217.

Holland, T.J.B., Powell, R. (1998). An internally consistent thermodynamic data set for phases of petrological interest. *Journal of Metamorphic Geology* 16:309-43.

Holland, T., Baker, J., Powell, R. (1998). Mixing properties and activity-composition relationships of chlorites in the system MgO-FeO-Al₂O₃-SiO₂-H₂O. *European Journal of Mineralogy* 10:395-406.

Hottinger, A. (1935). *Geologie der Gebirge zwischen der Sonnblick-Hocharn-Gruppe und dem Salztal in den östlichen Hohen Tauern* (Doctoral dissertation, Diss. Naturwiss. ETH Zürich, Nr. 853, 0000. Ref.: Staub, R.; Korref.: Niggli, P.).

Inger, S., Cliff, R. A. (1994). Timing of metamorphism in the Tauern Window, Eastern Alps: Rb-Sr ages and fabric formation. *Journal of metamorphic Geology*, 12(5), 695-707.

Janoušek, V., Farrow, C. M., Erban, V. (2006). Interpretation of whole-rock geochemical data in igneous geochemistry: introducing Geochemical Data Toolkit (GCDkit). *Journal of Petrology* 47(6):1255-1259

Jeřábek, P., Lexa, O., Schulmann, K., Plašienka, D. (2012). Inverse ductile thinning via lower crustal flow and fold-induced doming in the West Carpathian Eo-Alpine collisional wedge. *Tectonics*, 31(5).

Jeřábek, P., Faryad, W.S., Schulmann, K., Lexa, O., Tajčmanová, L. (2008). Alpine burial and heterogeneous exhumation of Variscan crust in the West Carpathians: insight from thermodynamic and argon diffusion modelling. *Journal of the Geological Society*, 165(2), 479-498.

Lammerer, B., Weger, M. (1998). Footwall uplift in an orogenic wedge: the Tauern Window in the Eastern Alps of Europe. *Tectonophysics*, 285(3), 213-230.

Lister, G.S., Snoke, A.W. (1984). SC mylonites. *Journal of Structural Geology*, 6(6), 617-638.

López-Carmona, A., Pitra, P., Abati, J. (2013). Blueschist-facies metapelites from the Malpica-Tui Unit (NW Iberian Massif): phase equilibria modelling and H₂O and Fe₂O₃ influence in high-pressure assemblages. *Journal of Metamorphic Geology*, 31(3), 263-280.

Massonne, H.J., Willner, A.P. (2008). Phase relations and dehydration behaviour of psammopelite and mid-ocean ridge basalt at very-low-grade to low-grade metamorphic conditions. *European Journal of Mineralogy*, 20(5), 867-879.

Neubauer, F., Genser, J., Kurz, W., Wang, X. (1999). Exhumation of the Tauern window, Eastern Alps. *Physics and Chemistry of the Earth, Part A: Solid Earth and Geodesy*, 24(8), 675-680.

Newton, R.C., Charlu, T.V., Kleppa, O.J. (1980). Thermochemistry of the high structural state plagioclases. *Geochemica Cosmochimica Acta*44:933-41.

Pestal, G., Hejl, E., Egger, H., van Husen, D., Linner, M., Mandl, G., Reitner, J., Rupp, C., Schuster, R. (2005). Geologische Karte von Salzburg 1:200.000, Geologische Bundesanstalt Vienna.

Pollington, A.D., Baxter, E.F. (2010). High resolution Sm–Nd garnet geochronology reveals the uneven pace of tectonometamorphic processes. *Earth and Planetary Science Letters*, 293(1), 63-71.

Ratschbacher, L., Frisch, W., Neubauer, F., Schmid, S. M., Neugebauer, J. (1989). Extension in compressional orogenic belts: the eastern Alps. *Geology*,17(5), 404-407.

Ratschbacher, L., Frisch, W., Linzer, H. G., Merle, O. (1991). Lateral extrusion in the Eastern Alps, part 2: structural analysis. *Tectonics*, 10(2), 257-271.

Rosenberg, C. L., Garcia, S. (2011). Estimating displacement along the Brenner Fault and orogen-parallel extension in the Eastern Alps. *International journal of earth sciences*, 100(5), 1129-1145.

Rosenberg, C. L., Brun, J. P., Gapais, D. (2004). Indentation model of the Eastern Alps and the origin of the Tauern Window. *Geology*, 32(11), 997-1000.

Rosenberg, C.L., Brun, J.P., Cagnard, F., Gapais, D. (2007). Oblique indentation in the Eastern Alps: insights from laboratory experiments. *Tectonics*,26(2).

Scharf, A., Handy, M.R., Favaro, S., Schmid, S.M., Bertrand, A. (2013). Modes of orogen-parallel stretching and extensional exhumation in response to microplate indentation and roll-back subduction (Tauern Window, Eastern Alps). *International journal of earth sciences*, 102(6), 1627-1654.

Schmid, S.M., Scharf, A., Handy, M.R., Rosenberg, C.L. (2013). The Tauern Window (Eastern Alps, Austria): a new tectonic map, with cross-sections and a tectonometamorphic synthesis. *Swiss Journal of Geosciences*,106(1), 1-32.

Schneider, S., Hammerschmidt, K., Rosenberg, C. L., Gerdes, A., Frei, D., Bertrand, A. (2015). U–Pb ages of apatite in the western Tauern Window (Eastern Alps): Tracing the onset of collision-related exhumation in the European plate. *Earth and Planetary Science Letters*, 418, 53-65.

Schulz, B., Triboulet, C., Audren, C. (1995). Microstructures and mineral chemistry in amphibolites from the western Tauern Window (Eastern Alps), and PT deformation paths of the Alpine greenschist-amphibolite facies metamorphism. *Mineralogical Magazine*, 59(397), 641-660.

Selverstone, J. (1985). Petrologic constraints on imbrication, metamorphism, and uplift in the SW Tauern Window, Eastern Alps. *Tectonics*, 4(7), 687-704.

Selverstone, J. (1988). Evidence for east-west crustal extension in the Eastern Alps:

Implications for the unroofing history of the Tauern window. *Tectonics*, 7(1), 87-105.

Selverstone, J. (1993). Micro-to macroscale interactions between deformational and metamorphic processes, Tauern Window, Eastern Alps. *Schweizerische Mineralogische und Petrographische Mitteilungen*, 73(2), 229-239.

Selverstone, J., Spear, F. S. (1985). Metamorphic P–T Paths from pelitic schists and greenstones from the south-west Tauern Window, Eastern Alps. *Journal of metamorphic Geology*, 3(4), 439-465.

Selverstone, J., Spear, F. S., Franz, G., Morteani, G. (1984). High-pressure metamorphism in the SW Tauern Window, Austria: PT paths from hornblende-kyanite-staurolite schists. *Journal of Petrology*, 25(2), 501-531.

Staub, R. (1924). *Der Bau der Alpen; Beitr. z. geol. Karte d. Schweiz, neue Folge*, 52, 107.

Tajčmanová, L., Connolly, J.A.D., Cesare, B. (2009). A thermodynamic model for titanium and ferric iron solution in biotite. *Journal of Metamorphic Geology* 27:153-64.

Thiele, O. (1980). *Das Tauernfenster*. In R. Oberhauser (ed.): *Der Geologische Aufbau Österreichs*, 300-314, Springer, Vienna.

Veselá, P., Lammerer, B., Wetzel, A., Söllner, F., Gerdes, A. (2008). Post-Variscan to Early Alpine sedimentary basins in the Tauern window (eastern Alps). *Geological Society, London, Special Publications*, 298(1), 83-100.

Veselá, P., Söllner, F., Finger, F., Gerdes, A., (2011). Magmato-sedimentary Carboniferous to Jurassic evolution of the western Tauern window, Eastern Alps (constraints from U-Pb zircon dating and geochemistry). *International Journal of Earth Sciences*, 100(5), 993-1027.

von Blanckenburg, F., Villa, I. M., Baur, H., Morteani, G., Steiger, R. H. (1989). Time calibration of a PT-path from the Western Tauern Window, Eastern Alps: the problem of closure temperatures. *Contributions to Mineralogy and Petrology*, 101(1), 1-11.

KINEMATICALLY UNRELATED S-C FABRICS: AN EXAMPLE OF EXTENSIONAL SHEAR BAND CLEAVAGE FROM THE VEPOR UNIT, WEST CARPATHIANS

Zita Bukovská¹, Petr Jeřábek¹, Ondrej Lexa¹, Jiří Konopásek², Marian Janák³, Jan Košler²

¹ Institute of Petrology and Structural Geology, Faculty of Science, Charles University, Albertov 6, 128 43 Prague 2, Czech Republic

² Department of Earth Science and Center for Geobiology, University of Bergen, Allégaten 41, N-5007 Bergen, Norway

³ Geological Institute, Slovak Academy of Science, Dúbravská 9, P.O. BOX 106, 840 05 Bratislava 45, Slovak Republic

Abstract

Discontinuous and kinematically unrelated S-C fabrics have been recognised along the contact between the Gemer and Vepor units in the West Carpathians. The formation of S and C fabrics within orthogneiss, quartzite and chloritoid-kyanite schist of the Vepor Unit is associated with Cretaceous syn-burial orogen-parallel flow and subsequent exhumational unroofing. The formation of the two fabrics characterized by distinct quartz deformation microstructure and metamorphic assemblage is separated by an inter-tectonic growth of transversal chloritoid-, kyanite-, \pm monazite-bearing assemblage. The monazite U-Th-Pb concordia age of 97 ± 4 Ma was obtained by laser ablation ICP-MS dating method. The age of this inter-tectonic metamorphic stage together with existing $^{40}\text{Ar}/^{39}\text{Ar}$ ages on exhumation of the Vepor Unit indicate that despite the similar appearance to shear bands or S-C mylonites there is at least 10 my time span between the formation of homogeneous S fabrics and superposed discrete C fabrics in the studied rocks.

Keywords: *Structural geology, discontinuous S-C fabrics, Central West Carpathians, Vepor Unit, shear band cleavage, quartz deformation microstructure, monazite dating*

1 Introduction

Shear bands refer to sub-parallel small-scale shear zones transecting an earlier anisotropy at small to intermediate angles which typically develop within larger-scale shear zones. These structures are associated with bulk simple shear or extension parallel to the earlier anisotropy and had been presented as shear bands (White, 1979; Gapais and White, 1982), C or C' bands

(Berthé et al., 1979; Ponce and Choukroune, 1980; Lister and Snoke, 1984), extensional crenulation cleavage (Platt, 1979; 1984; Platt and Vissers, 1980) or shear band cleavage due to its cleavage-like appearance (White et al., 1980; Passchier and Trouw, 2005). The main distinction between compressional crenulation cleavage and extensional shear band cleavage is based on the angle between cleavage and earlier foliation exhibiting 45-90° for compressional and less than 45° for extensional cleavage (Passchier and Trouw, 2005). Therefore the shear band cleavage needs to be revealed by the complete S-C structure defined by pervasive anisotropy S “Schistosité” and discretely spaced cleavage C “Cisaillement” (Berthé et al., 1979). The main controversy related to the field interpretation of S-C fabrics is their temporal and kinematic relationship i.e. within a shear zone the C fabrics form either as a result of increasing strain or due to the overprint of an earlier kinematically unrelated anisotropy (Lister and Snoke, 1984; Agard et al., 2011).

The contact zone between two major basement-cover thrust sheets, the hanging-wall Gemer and footwall Vepor units, in the Central West Carpathians is characterized by complicated structure of Early Cretaceous imbrications modified by Late Cretaceous extension (Plašienka, 1980; 1984; Lupták et al., 2000; 2003; Jeřábek et al., 2012). The extension resulted in the development of major shear zone associated with unroofing and exhumation of the Vepor Unit due to gravitationally-driven up-flow of middle crust in the core complex mode (Plašienka et al., 1999; Janák et al., 2001) or large-scale polyharmonic folding (Jeřábek et al., 2008; Jeřábek et al., 2013). The S-C fabrics recognized within this shear zone been previously interpreted as continuous kinematically related exhumation fabrics (Hók et al., 1993, Plašienka, 1993, Lupták et al., 2003).

In this study, we aim to decipher the kinematically related versus unrelated nature of the S-C fabrics developed within major extensional shear zone at the boundary between the Gemer and Vepor units in the West Carpathians. The S-C fabrics were studied in orthogneiss, quartzite and chloritoid-kyanite schist across the shear zone, which allowed us to perform detailed structural, microstructural, metamorphic and geochronological characterization of the two fabrics. Furthermore based on our new data, the regional context of complicated structure of the eastern part of the Gemer and Vepor contact zone is discussed.

2 Geological setting

The Vepor Unit together with the Gemer Unit to the east - southeast and Tatra Unit to the north (Fig. 1a) represent segments of Variscan crust that had been incorporated into the

structure of the Central West Carpathians wedge during the Cretaceous Eo-Alpine convergence (Plašienka et al., 1997). The Early Cretaceous thrust sheet stacking of the structurally lower Tatra, middle Vepor and upper Gemer Unit (Tomek, 1993; Plašienka et al., 1997) was followed by Late Cretaceous doming and exhumation of the deeper parts of the Vepor Unit (Janák et al., 2001; Jeřábek et al., 2012).

The studied area is located in the vicinity of the north-south trending contact between the footwall Vepor Unit and the hanging wall Gemer Unit (Fig. 1b). In this area, the Gemer Unit comprises Lower Palaeozoic volcano-sedimentary basement rocks of the Gelnica and Rakovec groups marked by low- to medium-grade Variscan metamorphism (Faryad, 1991) and overlying Upper Carboniferous–Permian metasedimentary cover (Vozárová and Vozár, 1988). The Gemer Unit is overthrust by the Meliata accretionary wedge complex of Jurassic age (Kozur and Mock, 1973; Faryad and Henjes-Kunst, 1997) and the uppermost Silica carbonate nappe system (Fig. 1a). Mostly low-grade Alpine metamorphic conditions have been determined for the Gemer Unit (e.g. Petrasová et al., 2007). In the studied area, the Vepor Unit is characterized by an imbricated structure (Plašienka, 1980; 1984) comprising from west to east and bottom to top (Fig. 1b, c): 1) Variscan basement migmatite, orthogneiss and Carboniferous granitoids (Bibikova et al., 1988; Michalko et al., 1998); 2) Permian cover quartzite; 3) garnet-bearing schist; 4) Permian cover quartzite-arkose marked by the presence of chloritoid-kyanite schist (Vrána, 1964; Lupták et al., 2000) and 5) Permo–Triassic quartzite and marble of the Foederata cover (Rozlosznik, 1935; Schönerberg, 1946). The garnet-bearing schists were traditionally related to the Vepor basement (Klinec, 1966; Vrána, 1966), however on the basis of pollen analysis they have been later reinterpreted as Carboniferous metasediments of the Vepor cover belonging to the Slatviná formation (Planderová and Vozárová, 1978; Vozárová and Vozár, 1988). The degree of Alpine metamorphic overprint reached amphibolite facies in the Vepor basement (up to 600 °C and 11 kbar, Vrána, 1966; Janák et al., 2001; Jeřábek et al., 2008) and greenschist facies in the Foederata cover (up to 380°C and 4.5kbar, Lupták et al., 2003). The metamorphic conditions of chloritoid-kyanite schists have been estimated to 530-560°C and 6-8 kbar (Lupták et al., 2000). The southern part of the studied area has been later affected by HT-LP contact metamorphism related to the intrusion of Upper Cretaceous Rochovce I-type granite (Kamenický, 1977; Klinec et al., 1980; Vozárová, 1990; Hraško et al., 1998; Poller et al., 2001).

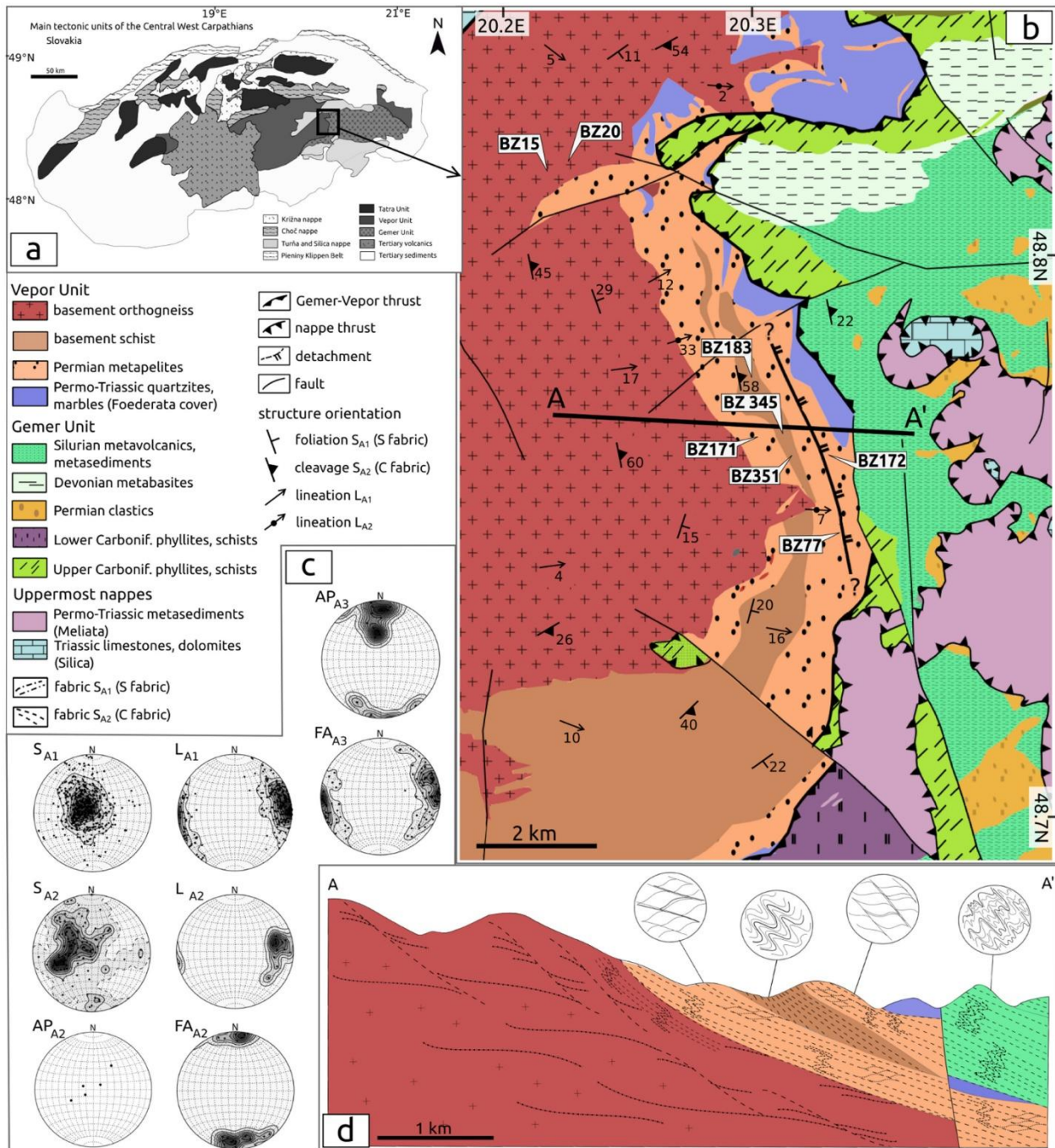


Fig. 1 a) Tectonic units of the Central West Carpathians. b) Simplified geological and structural map of the studied area including location of the studied samples and structural cross-section A-A', structural symbols show orientation of foliation S_{A1} (S fabric) and cleavage S_{A2} (C fabric), and accompanying lineations. Map based on Geological map of Slovak republic 1:50 000 <http://mapserver.geology.sk>. c) Lower hemisphere equal area projection of main structures documented in the studied area (S - foliation, L - lineation, AP – fold axial plane, FA – fold axis, and A1-A3 - Alpine deformation events). Contours are double the multiples of standard deviation above the uniform distribution. d) Structural cross-section across the Gemer-Vepor contact zone with macroscopic insets. GPS coordinates of selected localities: BZ13 48°42'15.38"N, 20°18'24.12"E; BZ15 48°43'55.91"N, 20°17'03.50"E; BZ20 48°48'10.32"N, 20°13'14.10"E; BZ22 48°48'20.97"N, 20°14'55.78"E; BZ77 48°46'46.52"N, 20°17'09.85"E; BZ171 48°47'45.69"N, 20°16'45.87"E; BZ172 48°45'20.16"N, 20°18'30.31"E; BZ183 48°45'48.61"N, 20°17'47.90"E; BZ188 48°45'34.55"N, 20°17'56.23"E; BZ345 48°45'17.49"N, 20°18'30.24"E; BZ351 48°45'18.65"N, 20°18'30.47"E.

3 Structural record in the studied area

Within the hanging wall Gemer Unit, we identified one penetrative metamorphic foliation overprinted by two phases of folding. The greenschist facies metamorphic foliation S_V recognised exclusively in the Lower Palaeozoic rocks of the Gemer Unit is similarly to other authors (e.g. Faryad, 1990; Hovorka et al., 1988) considered to result from Variscan tectono-metamorphic event. This foliation shows various orientation due to subsequent folding characterized by steep or south facing and generally E-W trending axial planes or low-grade spaced cleavage. On the scale of Gemer Unit, this latter cleavage forms large-scale positive fan-like structure interpreted to result from the Early Cretaceous overthrusting of the Gemer Unit over Vepor (Snopko, 1971; Lexa et al., 2003). In the proximity of the Gemer-Vepor boundary, both Variscan fabrics and steep Early Alpine cleavage are affected by isoclinal folding with subhorizontal axial planes and E-W trending axes.

In the footwall Vepor Unit, we recognised three deformation-metamorphic fabrics which were subsequently affected by one folding event. The oldest deformation fabric comprises scarce relics of high grade Variscan foliation S_V in basement migmatites and schists. The first Alpine metamorphic foliation S_{A1} heterogeneously affects both basement and cover and dips generally to the E or SE under shallow to intermediate angles (Fig. 1b, c). The S_{A1} fabric bears mineral and stretching lineation L_{A1} defined by shape preferred orientation of quartz aggregates and white mica, which plunges generally to the east (Fig. 1b, c). The S_{A1} is axial planar to the locally preserved isoclinal folds affecting Variscan foliations in the basement and bedding in the cover. The fold axes are typically E-W trending i.e. subparallel to lineation L_{A1} . In the basement, the S_{A1} is only heterogeneously overprinted by discrete S_{A2} cleavage, while in the cover the S_{A2} becomes dominant deformation fabric. This late cleavage dips to the E or SE at steeper angles than the foliation S_{A1} and bears an east-plunging mostly muscovite-bearing lineation (Fig. 1c). The S_{A2} is axial planar to the locally developed isoclinal folds F_{A2} characterised by N-S trending axes. The S_{A2} is defined mainly by shape preferred orientation of chlorite and white mica. The last deformation event is associated with upright folding of all previous fabrics and led to the development of small-scale crenulations as well as large-scale folds F_{A3} with generally E-W trending axial planes (Fig. 1b, c). This late stage folding is associated with the development of sinistral transpressional shear zone along the NE-SW trending Gemer-Vepor boundary to the south from the studied area (Lexa et al., 2003).

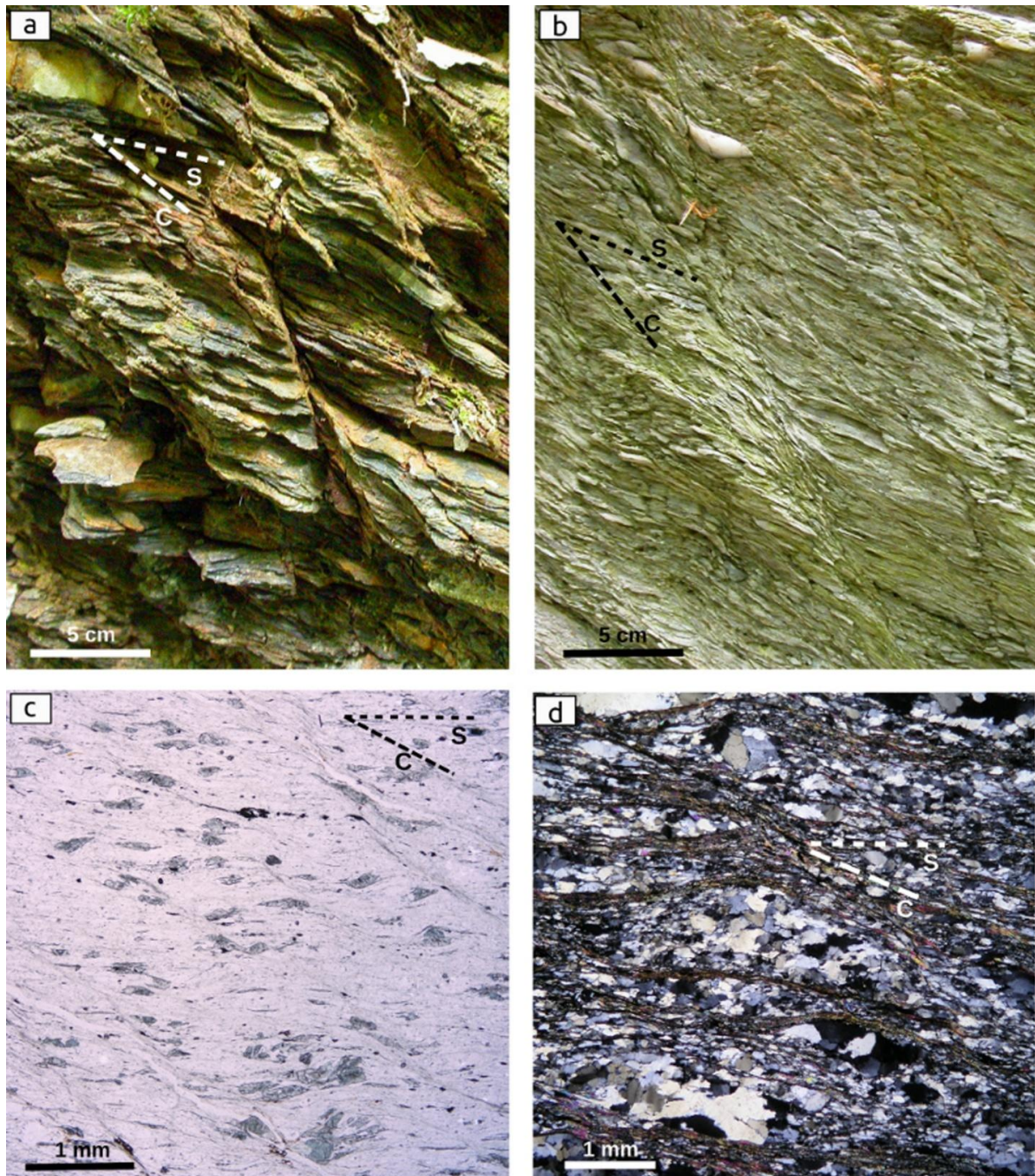


Fig. 2 Field photographs (a, b) and micrographs (c, d) of S-C fabrics in the Vepor Unit: a) basement schist, b) Permian quartzite, c) chloritoid-kyanite schist and d) quartzite (crossed polarisers).

In the studied area, the SA1 and SA2 fabrics typically show the low angle extensional shear band cleavage relationships characterized by discrete cleavage SA2 cross-cutting the foliation SA1 (Fig. 2) and thus in the subsequent text, the two fabrics will be referred as C and S fabrics, respectively. These S-C fabrics form an angle ranging between 10 and 30° and are characterized by the normal top-to-the-east sense of shear. The LA1 and LA2 lineations (Fig. 1c) are both perpendicular to the S-C intersection implying the synkinematic character of the two fabrics (Passchier and Trouw, 2005).

4 Analytical techniques

The S-C fabrics in the Vepor Unit were analysed in orthogneiss, chloritoid-kyanite schist and quartzite (Figs. 2 and 3a), which allowed us to characterize both fabrics in terms of quartz deformation microstructure and texture, metamorphism and age. The analyses were performed in the thin sections parallel to XZ plane of finite strain ellipsoid, i.e. parallel to L_{A1} and L_{A2} lineations and perpendicular to intersection of S-C fabrics.

Quartz deformation microstructure have been quantitatively analysed by means of Computer Integrated Polarization microscopy (CIP) technique of Panozzo Heilbronner and Pauli (1993) and Electron Backscatter Diffraction (EBSD) technique using HKL system attached to scanning electron microscope TESCAN at the Institute of Petrology and Structural Geology, Charles University in Prague. The grain size and grain shape statistics were obtained from manually digitized grain maps based on CIP-derived misorientation images (Heilbronner, 2000) using the PolyLX Matlab toolbox (Lexa 2003). In this paper, the average 2D grain size is defined as 1 sigma range of area weighted logarithmic mean of equal area diameter. The grain shapes are characterized by particle (PAROR) and surface (SURFOR) orientation distribution functions (ODF) (Panozzo, 1983; 1984) shown in the rose diagrams.

Chemical analyses of selected minerals were carried out using EDS detector X-Max 50 (Oxford Instruments) attached to scanning electron microscope TESCAN Vega at the Institute of Petrology and Structural Geology, Charles University in Prague. The analyses were obtained with accelerating potential 15kV and beam current 1nA. Matrix correction procedure XPP was used based on Phi-Rh-Z method. The precision control was held by repeated analyses measurements on known phases, mainly standards. Standards that were used for each analysed element (element, detection limit of 2 sigma in weight %): albite (Na, 0.1); synthetic periclase (Mg, 0.04); synthetic $Y_3Al_5O_{12}$ (Al, 0.1); sanidine (Si, 0.16); sanidine (K, 0.04); wollastonite (Ca, 0.04); synthetic rutile (Ti, 0.06); synthetic Cr_2O_3 (Cr, 0.06); rhodonite (Mn, 0.08); haematite (Fe, 0.08); pentlandite (Mn, 0.12).

Chloritoid analyses were normalised to 12 oxygens, chlorite was normalised to 14 oxygens and white mica analyses were normalised to 11 oxygens (see Table 1). The classification of white mica followed Tischendorf et al. (2004). X_{Mg} is defined as $X_{Mg} = Mg/(Mg+Fe)$.

U-Th-Pb dating of monazite was performed directly from polished thin sections by laser ablation ICP-MS analysis following the technique described in Košler et al. (2001). A Thermo-Finnigan Element 2 sector field ICP-MS coupled to a 193 nm ArF excimer laser

(Resonetics RESolution M-50 LR) at Bergen University was used to measure Pb/U and Pb/Th isotopic ratios. The laser was fired at 5 Hz using energy of 40 mJ/pulse and beam diameter of 7 micrometers, while the sample was moved underneath the laser beam to produce linear raster pits (<5 μm deep) in the monazite grains. The ablation was done in He (0.65 l/min). Fragment of a large monazite crystal from a granulite in the Androyan Complex in Madagascar (555 Ma: U-Pb TIMS age by R. Parrish, pers. comm. and 557 ± 20 Ma: electron microprobe chemical dating by Montel et al., 1996) was used to calibrate the Tl-Bi-Np tracer solution that was analysed simultaneously with the ablated monazite samples. In addition, two monazite samples with known TIMS ages (Tarasinga leptynite, India, 953 ± 4 Ma, Aftalion et al., 1988, and garnetiferous gneiss from the Lake Baikal Complex, Russia; 1862 ± 4 Ma, Aftalion et al., 1991) were periodically analysed during this study for quality control and yielded concordia ages of 957 ± 43 Ma ($n=5$) and 1868 ± 89 Ma ($n=3$), respectively (n = number of analyses; all uncertainties are 2 sigma).

5 Quartz deformation microstructure

All studied samples show two distinct quartz microstructures related to S and C fabrics as exemplified by two samples in Fig. 3A, i.e. orthogneiss sample BZ15 and quartzite sample BZ77 (for location see Fig. 1). The S fabrics are defined by recrystallized quartz aggregates with larger grain size, which are cross-cut or modified by localized C fabrics forming tails of recrystallized grains with considerably smaller grain size (Fig. 3a). The aggregates show grain size within the ± 1 sigma range of 45-184 μm ($d_{\text{mean}} = 91 \mu\text{m}$) for orthogneiss and 140-403 μm ($d_{\text{mean}} = 237 \mu\text{m}$) for quartzite, while the tails show grain size within the range of 20-56 μm ($d_{\text{mean}} = 33 \mu\text{m}$) for orthogneiss and 47-140 μm ($d_{\text{mean}} = 81 \mu\text{m}$) for quartzite (Fig. 3d).

The quartz grains are strongly elliptical in orthogneiss aggregates while the grains in tails from both lithologies and quartzite aggregates show weak ellipticity (Fig. 3a). The shape preferred orientation of quartz grains characterized by particle ODF (PAROR) is subparallel to the long axis of either the S fabric aggregates or C fabric tails (Fig. 3c). The surface ODF (SURFOR) in quartzite aggregates shows symmetric distribution with maximum parallel to the aggregate long axis. In quartzite tails, the surface ODF is weakly monocline with maximum that is slightly inclined with respect to the tail orientation. In orthogneiss, the surface ODF is weakly to strongly monocline with maxima that are slightly and strongly inclined with respect to aggregate and tail orientation, respectively (Fig. 3c). Within the C fabrics, the inclination of surface ODF maxima with respect to C tails orientation is consistent

with observed macroscopic sense of shear (e.g. Simpson and Schmid, 1983).

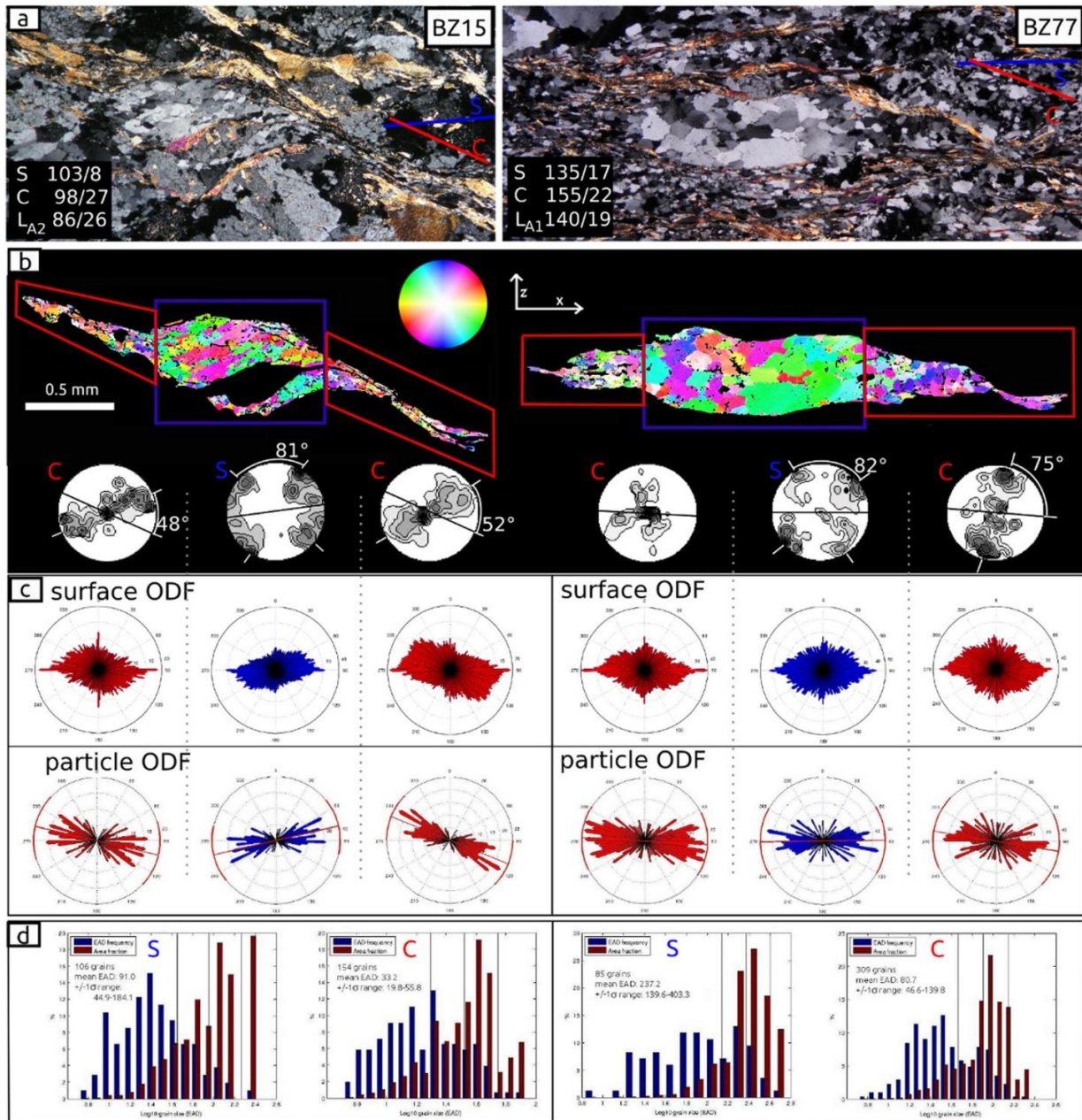


Fig. 3 Quartz microstructure within S and C fabrics from orthogneiss sample BZ15 (left column) and quartzite sample BZ77 (right column). a) Micrograph (crossed polarisers) of S-C fabrics shows recrystallized quartz aggregates within S fabric and tails within C fabric. b) Quartz c-axis CPO images and corresponding lower hemisphere equal area pole figures from S aggregates and C tails. The c-axis orientation colouring of individual grains is shown in colour look-up table pole figure. The black lines in the pole figures correspond to the long axis of S aggregates and C tails, and the contours correspond to multiples of uniform distribution. c) Surface (SURFOR) and particle (PAROR) orientation distribution functions for S aggregates and C tails. d) Quartz grain size distributions within S aggregates and C tails manifested by 2D equal area diameter (EAD) frequency and area fraction. The average 2D grain size defined as 1σ range of area weighted logarithmic mean of EAD and number of grains are also shown in the histograms.

6 Quartz texture

The crystal preferred orientation (CPO) of quartz c-axes shows similar patterns for both orthogneiss and quartzite samples. Within the aggregates defining the S fabric, the c-axis CPO's are characterized by two-point peripheral maxima, which are symmetrically distributed around the aggregate long axis at the distance of approximately 50° (Figs. 3b, 4a). Additionally, the aggregate in orthogneiss sample BZ15 shows two-point peripheral c-axis submaxima distributed symmetrically around the aggregate long axis within $\sim 15^\circ$ distance. On the other hand, the aggregate in quartzite sample BZ77 shows minor c-axis submaximum in the centre of the pole figure. The aggregate double point maxima in both samples are interpreted to result from activity of basal $\langle a \rangle$ slip system while the submaxima suggest prism $\langle a \rangle$ slip in case of quartzite and prism $\langle c \rangle$ slip in case of orthogneiss (e.g. Schmid and Casey, 1986). By using the fabric opening thermometer of Kruhl (1996, 1998) modified by Morgan and Law (2004), the c-axis opening angle of $\sim 80^\circ$ (Figs. 3b, 4a) corresponds to $\sim 550^\circ\text{C}$.

Within the tails defining the C fabric, the c-axis CPO's show single girdle patterns inclined with respect to C planes (Figs. 3b, 4b, c). This inclination is more pronounced in orthogneiss sample BZ15 compared to quartzite sample BZ77 as indicated by the angle of $46\text{-}52^\circ$ and 75° between the single girdle trace and C fabric trace in the pole figures (Figs. 3b, 4b, c). The highly inclined c-axis single girdle pattern is characteristic for combined activity of rhomb $\langle a \rangle$ and prism $\langle a \rangle$ slip systems (Keller and Stipp, 2011) and suggests normal sense of shearing along the C planes (Lister and Williams, 1979; Simpson and Schmid, 1983; Schmid and Casey, 1986).

7 Petrography and mineral chemistry

Within the imbricated structure of the studied area several lithologies have been evaluated by means of petrography and mineral chemistry. These are from bottom to top: 1) Vepor basement orthogneiss; 2) Vepor cover quartzite belonging to Rimavica formation; 3) Vepor garnet-bearing schist; 4) Vepor cover chloritoid-kyanite schist and 5) Foederata cover quartzite (Fig. 1b, c). In orthogneiss and chloritoid-kyanite schist, the analysis revealed that both S and C fabrics are associated with distinct metamorphic record.

In orthogneiss, the S fabric is defined by metamorphic mineral assemblage of biotite, chlorite, white mica, albite and quartz. In contrast, the discrete C fabric contains only chlorite, white mica and quartz. While chlorite in both fabrics shows identical composition with $X_{\text{Mg}} =$

0.56 (sample BZ20B, Table 1), the chemical analyses of white mica revealed three generations that include muscovite I, phengite and muscovite II (sample BZ20B in Figs. 5a, b and 6a). The first generation of white mica (muscovite I) is represented by large flakes (ca. 1 mm in size) that are associated neither with the S, nor the C fabric and are probably of magmatic origin (Fig. 4a). The Si content in muscovite I varies between 3.09-3.15 a.p.f.u. (Table 1, Fig 6a). Muscovite I flakes are overgrown by second generation of white mica (phengite) which is common in the S fabric (Fig. 5a, b).

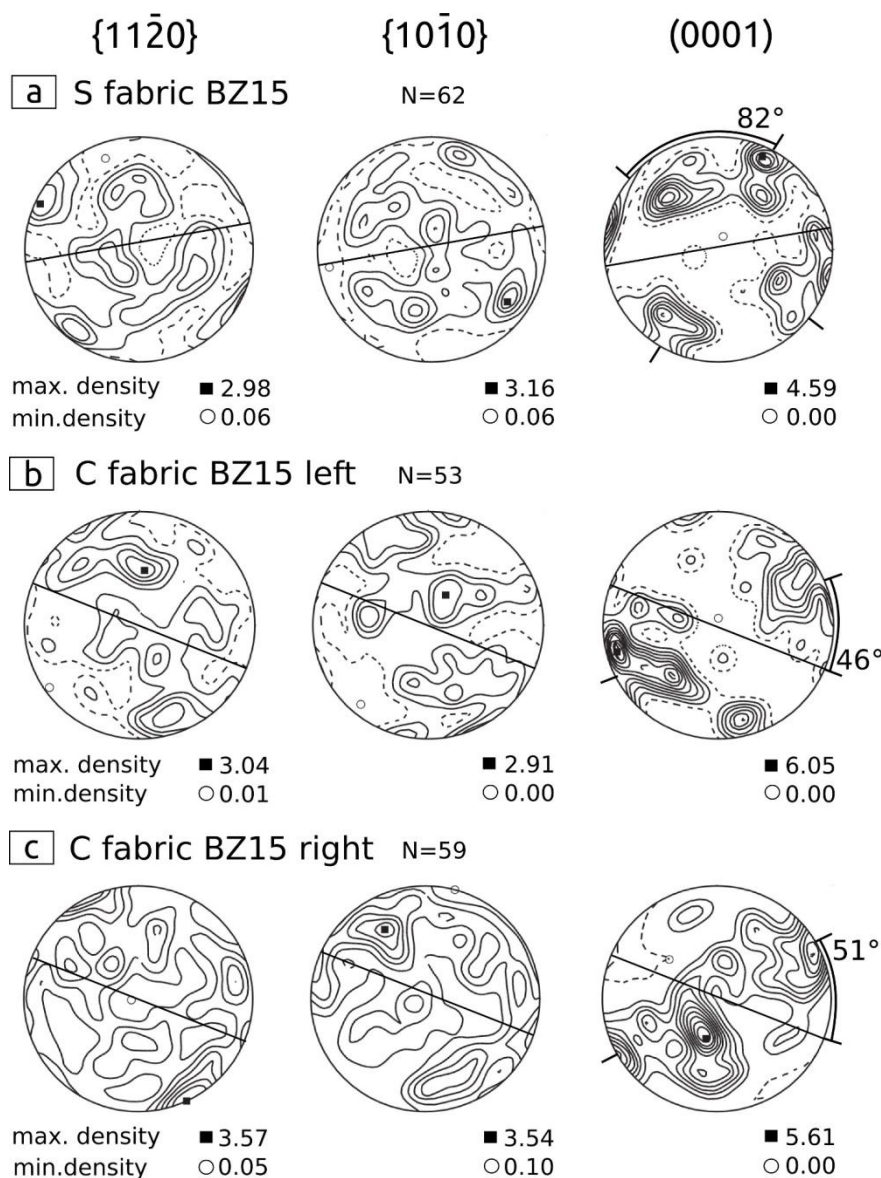


Fig. 4 The lattice preferred orientation data of recrystallized quartz within S aggregate a) and C tail b), c) in sample BZ15 (same region as in Fig. 3, a)-centre, b)-left, c)-right) obtained by means of electron back-scattered diffraction (EBSD). Each pole figure in lower hemisphere equal area projection contains number of measured grains, minimum and maximum of the density distribution and contours corresponding to 0.5 multiples of uniform distribution.

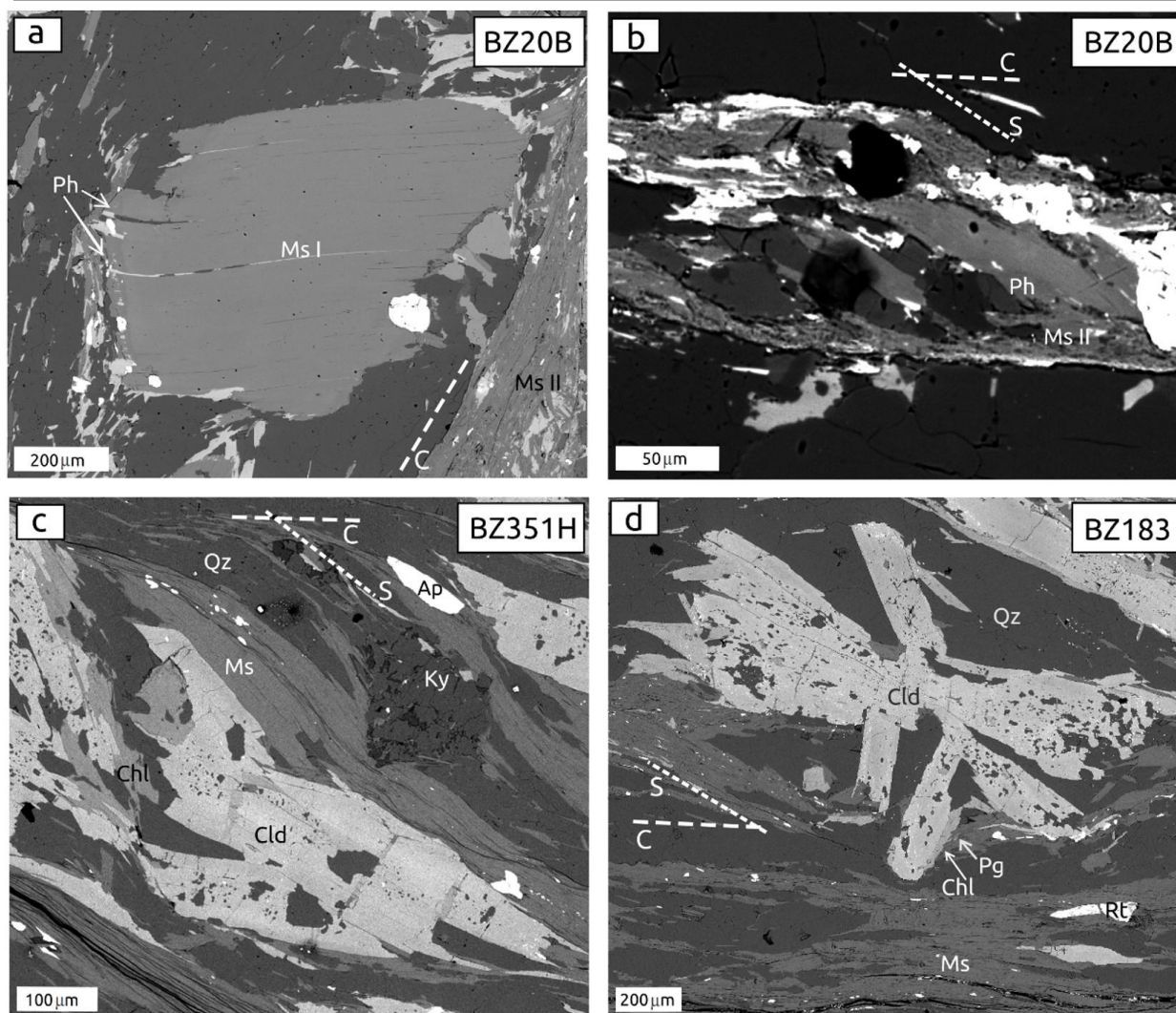


Fig. 5 BSE images showing white micas in orthogneiss sample BZ20B (a, b) and mineral assemblage in chloritoid schist samples BZ351H (c) and BZ183 (d) and their relation to S-C fabrics. a) Large muscovite grain (Ms I) overgrown by phengite (Ph) and younger muscovite (Ms II) within C fabric. b) Phengite within S fabric replaced by muscovite II within C fabric. c), d) Peak assemblage of kyanite, chloritoid, white mica, chlorite and quartz in chloritoid-kyanite schist associated with S fabric being crosscut by C fabric defined by muscovite-chlorite. Mineral abbreviations: Ap - apatite, Chl - chlorite, Cld - chloritoid, Ky - kyanite, Ms - muscovite, Pg - paragonite, Ph - phengite, Qz - quartz, Rt - rutile.

In accordance to the classification of Tischendorf et al. (2004), this white mica is phengite and contains between 3.27-3.38 a.p.f.u. of Si (Table 1, Fig. 6a). The last generation of white mica (muscovite II) with 3.1-3.15 a.p.f.u. of Si (Table 1, Fig. 6a) replaces the earlier phengite and it is associated with the C fabrics (Fig. 5a, b). Identical compositional sequence of white mica was previously reported from the Vepor basement by Sulák et al. (2009), however in their study no relationship to the deformation structures has been revealed.

Overlying Vepor cover quartzite belonging to Rimavica formation (sample BZ171) consist of quartz, phengite, monazite, zircon and ilmenite. The chemical analysis of white mica did not reveal major compositional differences between S and C fabrics in individual samples.

White mica in quartzite samples located closer to the basement orthogneiss is phengite with 3.11-3.34 a.p.f.u. of Si (Fig. 6b).

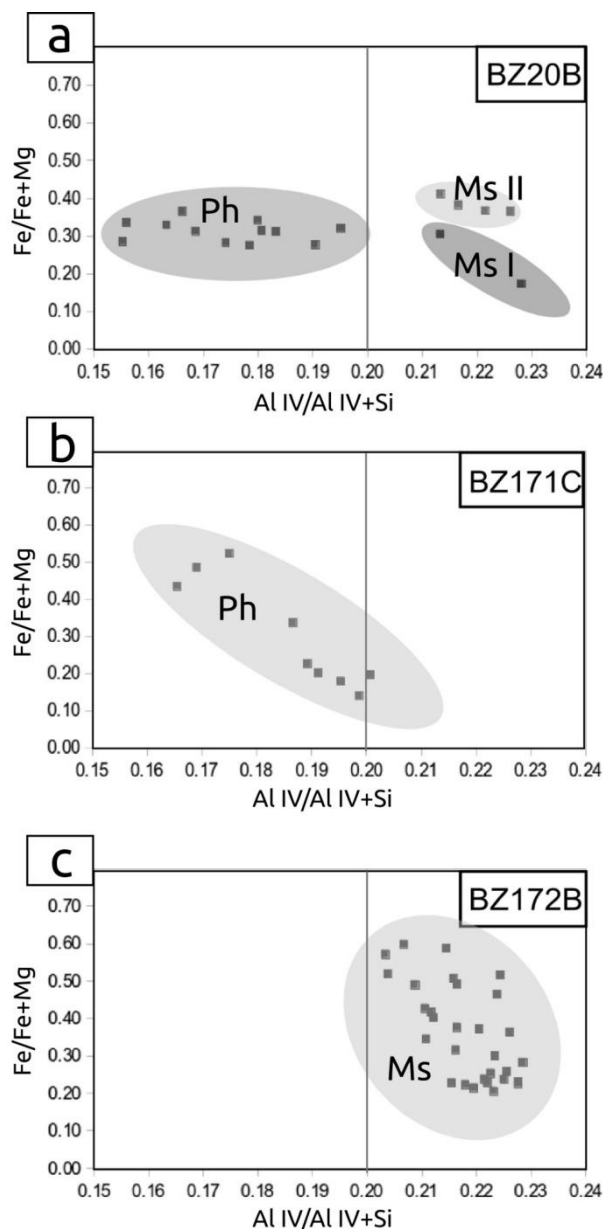


Fig. 6 Compositional diagram for white mica from a) orthogneiss sample BZ20B, b) quartzite sample BZ171C and c) arkose sample BZ172B (for location of samples see Fig. 1 and for representative white mica analyses see Table 1). The diagrams show (a) three white mica generations in orthogneiss: original magmatic muscovite (Ms I), phengite (Ph) from the S fabric and younger muscovite (Ms II) from the C fabric (see Fig. 5a, b) and (b, c) single generation of white mica represented by phengite in quartzite (b) and muscovite in arkose (c). The distinction between phengite and muscovite is based on Tischendorf et al. (2004).

mineral	Ms I	Ph	Ms II	Chl	Pg	Mrg	Cld	Ms	Chl
sample	BZ20B	BZ20B	BZ20B	BZ20B	BZ349	BZ351H	BZ351H	BZ183	BZ349
litology	orthogneiss				chloritoid-kyanite schist				
SiO ₂	45.85	50.80	47.72	35.99	45.09	37.01	23.09	46.06	23.89
TiO ₂	0.67	0.37	0.41	1.62	0.00	0.00	0.00	0.21	0.00
Cr ₂ O ₃	0.00	0.00	0.00	0.00	0.00	0.00	0.00	0.00	0.00
Al ₂ O ₃	32.68	29.63	34.21	17.12	40.55	46.80	38.97	36.29	21.74
FeO	2.43	1.85	1.91	16.12	0.73	1.01	22.71	2.18	24.36
MnO	0.00	0.00	0.00	0.18	0.00	0.00	0.41	0.00	0.00
NiO	0.00	0.00	0.00	0.00	0.00	0.00	0.00	0.00	0.00
MgO	1.91	2.59	1.53	11.57	0.00	0.08	4.00	0.55	14.42
CaO	0.00	0.00	0.00	0.00	0.55	6.57	0.00	0.00	0.00
Na ₂ O	0.27	0.11	0.23	0.00	6.77	3.26	0.00	1.13	0.00
K ₂ O	10.72	10.68	10.56	9.81	0.99	1.01	0.00	9.13	0.00
Total	94.52	96.02	96.57	92.42	94.67	95.75	89.17	95.54	84.42
Si	3.09	3.38	3.15	3.48	2.91	2.40	1.96	3.06	2.614
Ti	0.03	0.02	0.02	0.12	0.00	0.00	0.00	0.01	0.000
Cr	0.00	0.00	0.00	0.00	0.00	0.00	0.00	0.00	0.000
Al	2.59	2.32	2.66	1.95	3.08	3.58	3.90	2.84	2.804
Fe ³⁺	0.12	0.00	0.00	0.00	0.02	0.05	0.19	0.00	0.000
Fe ²⁺	0.02	0.10	0.11	1.30	0.02	0.00	1.42	0.12	2.229
Mn	0.00	0.00	0.00	0.01	0.00	0.00	0.03	0.00	0.000
Ni	0.00	0.00	0.00	0.00	0.00	0.00	0.00	0.00	0.000
Mg	0.19	0.26	0.15	1.67	0.00	0.01	0.51	0.05	2.352
Ca	0.00	0.00	0.00	0.00	0.04	0.46	0.00	0.00	0.000
Na	0.04	0.01	0.03	0.00	0.85	0.41	0.00	0.15	0.000
K	0.92	0.91	0.89	1.21	0.08	0.08	0.00	0.77	0.000
Total	7	7	7	10	7	7	8	7	10
X Mg	0.58	0.59	0.71	0.56	0.00	0.13	0.24	0.31	0.51

Tab. 1 Representative chemical analyses of muscovite (Ms), phengite (Ph) and chlorite (Chl) from orthogneiss sample BZ20B, chloritoid (Cld), chlorite (Chl), margarite (Mrg), paragonite (Pg) and muscovite (Ms) from chloritoid-kyanite schist samples BZ349 and BZ351H and garnet core and rim (GtI, GtII) from garnet-bearing schist BZ188 (for location of samples see Fig. 1).

The overlying garnet-bearing schist typically consists of quartz, biotite, muscovite, chlorite, ilmenite, ± garnet and ± tschermakite. In sample BZ188 located near the chloritoid-kyanite schists (Fig. 1b), the garnet consists of two compositional varieties (Fig. 7) with core garnet (GtI) rich in magnesium, manganese and iron (alm_{60-70} , sps_{9-13} , prp_{9-12} , grs_{5-6} , Fig. 7, Tab.1) and rim garnet (GtII) enriched in calcium (alm_{57-62} , grs_{20-22} , prp_{6-7} , sps_{5-6} , Fig. 7, Tab. 1). Such a compositional zoning has been previously described from identical garnet-bearing schist from the Blh Valley by Korikovsky et al. (1990) and Jeřábek et al. (2008). On the basis of PT calculations the later authors relate the garnet core and rim to the Variscan and Alpine metamorphism, respectively, implying the basement origin of these schists (Vrána, 1964, Korikovsky et al., 1990, Jeřábek et al., 2008).

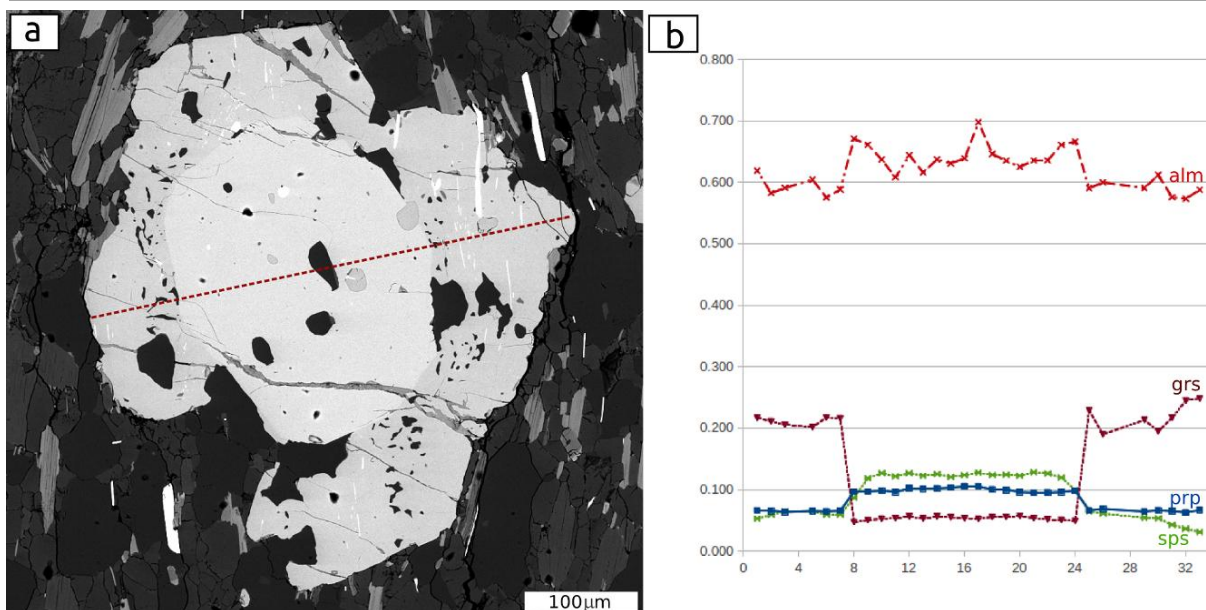


Fig. 7 a) BSE image showing garnet from tschermakite-garnet schist with orientation of compositional profile (sample BZ188). b) Compositional profile across garnet grain with content of almandine (alm), grossular (grs), pyrope (prp) and spessartine (sps) component.

The Vepor cover chloritoid-kyanite schist located at the contact between the basement schist and Permian cover quartzite (samples BZ351H, BZ345 and BZ183) consists of kyanite, chloritoid, white mica, chlorite, quartz ± tourmaline and accessory apatite, ilmenite, rutile, zircon ± monazite ± allanite ± xenotime (Fig. 5c, d). The chloritoids show radial-growth appearance which is commonly transversal to the S fabric and cross-cut by the C fabric (Figs. 2c, 5c, d). This indicates an inter-tectonic growth of the kyanite, chloritoid, white mica, chlorite, monazite and quartz assemblage. The chemical analyses of white mica revealed the presence of muscovite, paragonite and margarite, associated with chloritoid- and kyanite-bearing assemblage (Table 1, Fig. 6d). The X_{Mg} in chloritoid within different samples ranges between 0.17-0.34 and shows slight but irregular zoning. Within individual samples the X_{Mg} in chloritoid differs mostly by 0.02-0.09. The C fabrics are characterized by muscovite, chlorite and quartz assemblage. The chemical composition of chlorite and muscovite associated with S and C fabrics, respectively, did not reveal major differences so that the X_{Mg} in chlorite is ~0.51 and Si content in muscovitic mica ranges between 2.95-3.08 a.p.f.u.

The Permian Foederata cover quartzites and arkoses are formed by white mica-quartz ± chlorite ± albite and accessory ilmenite, rutile ± apatite ± zircon ± monazite (Fig. 2d). The chemical analysis of white mica did not reveal major compositional differences between S and C fabrics in individual samples. The rock is phengite absent comparing to the cover quartzites (BZ171). White mica is muscovite with 3.09-3.19 a.p.f.u. of Si (BZ172B in Fig. 6c; for location see Fig. 1).

8 Monazite dating

Monazite was identified in the chloritoid- and kyanite-bearing schist (sample BZ345; for location see Fig. 1) as subhedral to anhedral, usually elongated grains of ~50–100 μm in length. Monazite occurs either within the recrystallized quartz aggregates or as grains completely enclosed by muscovite. Many monazite grains show sharp, non-altered contacts with chloritoid and other mineral phases of this kyanite, chloritoid, white mica, chlorite and quartz assemblage (Fig. 8a, b), which suggests that monazite is stable member of this inter-tectonic (see above) assemblage. The high resolution back-scattered electron images of several monazite grains revealed some compositional variations (Fig. 8c), however the spatial resolution of laser ablation did not allow analysis of the small compositionally different domains. Monazite grains were analysed directly in polished thin sections (Fig. 8d). Ten selected monazite grains analysed in sample BZ345 (Table 2) yielded a pooled U-Th-Pb concordia age of $97 \pm 4 \text{ Ma}$ (± 2 sigma, Fig. 9, Table 2), which is interpreted as monazite crystallization age.

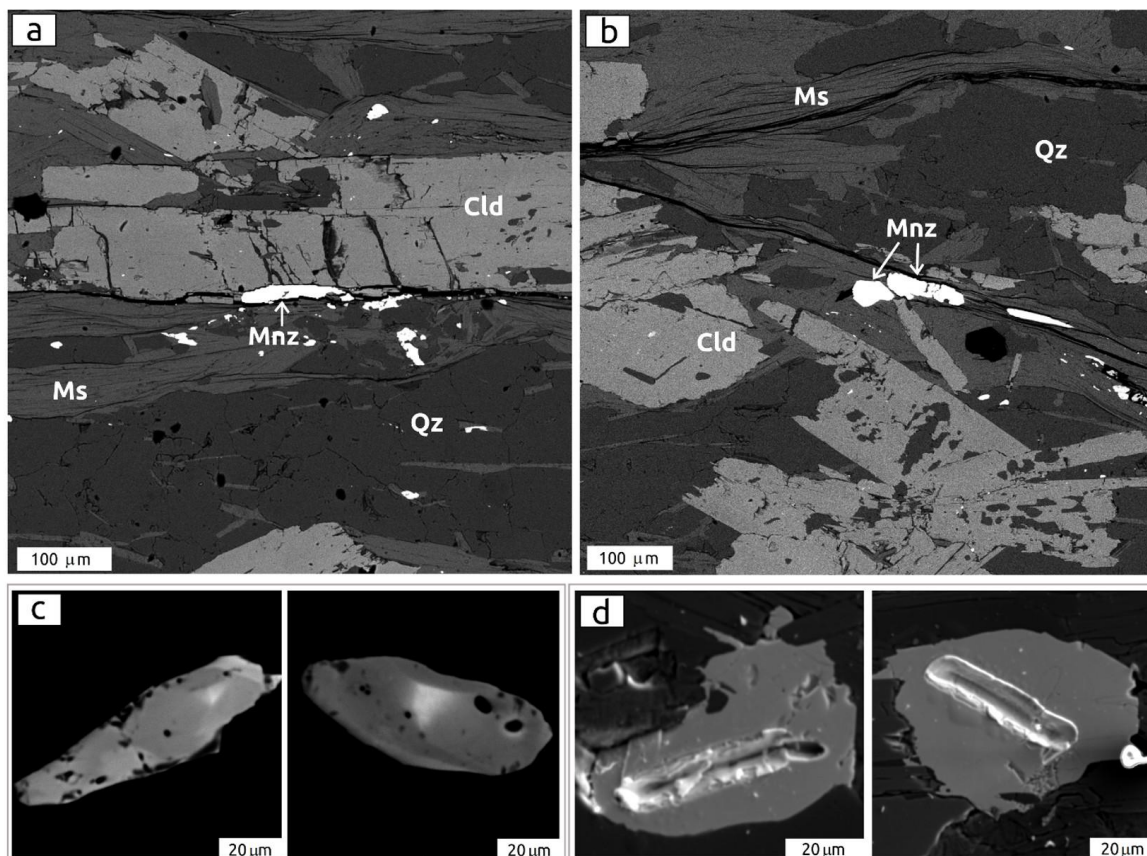


Fig. 8 a), b) BSE images showing close relationship of dated monazite (Mnz) and chloritoid in chloritoid-kyanite schist sample BZ345. c) Detailed BSE images show relatively homogeneous chemical composition of dated monazite grains. d) SE images show positions of analysed sections within monazite grains. For mineral abbreviations see Fig. 5. caption.

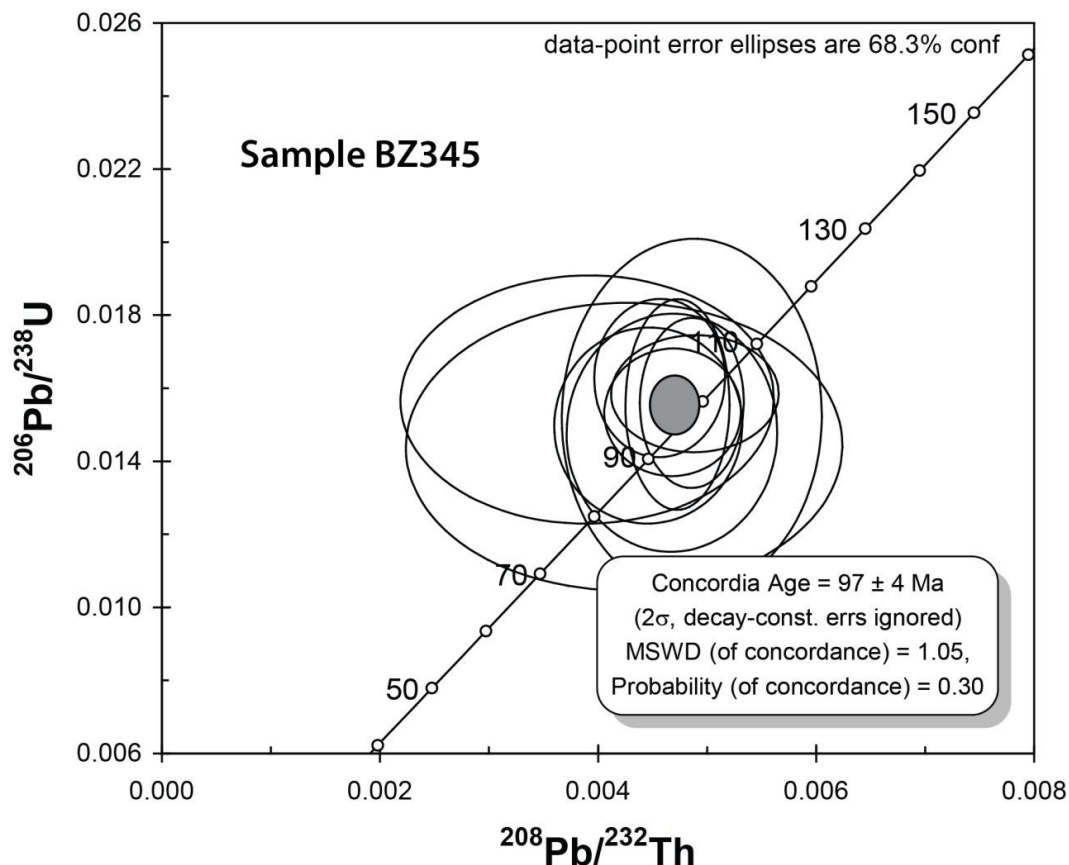


Fig. 9 U–Th–Pb concordia diagram for monazite from sample BZ345. For isotopic ratios see Table 2.

Analysis	ISOTOPIC RATIOS				CALCULATED AGES Ma			
	$^{208}\text{Pb}/^{232}\text{Th}$	± 1 sigma	$^{206}\text{Pb}/^{238}\text{U}$	± 1 sigma	$^{208}\text{Pb}/^{232}\text{Th}$	± 1 sigma	$^{206}\text{Pb}/^{238}\text{U}$	± 1 sigma
Sample BZ345								
# 1	0.0049	0.0005	0.0158	0.0011	99	10	101	7
# 2	0.0049	0.0003	0.0156	0.0015	98	6	100	10
# 3	0.0042	0.0013	0.0144	0.0026	86	27	92	17
# 4	0.0049	0.0008	0.0152	0.0032	98	16	97	20
# 5	0.0047	0.0004	0.0153	0.0012	94	8	98	7
# 6	0.0039	0.0011	0.0157	0.0022	79	23	100	14
# 7	0.0046	0.0004	0.0163	0.0014	92	8	104	9
# 8	0.0047	0.0003	0.0156	0.0019	95	6	100	12
# 9	0.0045	0.0006	0.0150	0.0018	90	11	96	11
# 10	0.0047	0.0006	0.0148	0.0022	94	13	95	14

Tab. 2 Laser ablation ICP–MS U–Th–Pb data for the sample BZ345. Only $^{208}\text{Pb}/^{232}\text{Th}$ and $^{206}\text{Pb}/^{238}\text{U}$ isotopic ratios and corresponding ages are presented. Determination of $^{207}\text{Pb}/^{206}\text{Pb}$ and $^{207}\text{Pb}/^{235}\text{U}$ ages was precluded by low signal intensity of ^{207}Pb .

9 Discussion

The S-C fabrics at the contact between Gemer and Vepor units have been previously interpreted as synkinematic and related to localization of deformation within the large scale detachment shear zone developed during unroofing and exhumation of the Vepor dome (Hók et al., 1993; Plašienka, 1993; Lupták et al., 2000; Janák et al., 2001). Indeed, the outcrop observations of S-C fabrics in the Vepor Unit show that lineations on both fabrics formed at high angle to the fabrics intersection, implying its continuous kinematically related single-event formation. In the following discussion we bring the petrography-petrology, deformation microstructure and geochronology-based evidence suggesting that the studied S and C fabrics in the Vepor Unit were in contrast formed during two independent and kinematically unrelated tectonic events.

As already mentioned in the structural description, the studied S fabric is related to subhorizontal Alpine metamorphic foliation S_{A1} identified elsewhere throughout the Vepor Unit. In the basement, this fabric is associated with phengite, garnet, chloritoid, staurolite and kyanite bearing assemblages with estimated PT conditions ranging between 5-11 kbar and 430-620 °C (e.g. Janák et al., 2001; Jeřábek et al., 2008). In addition, Jeřábek et al. (2008) documented that S_{A1} foliation is associated with the growth of Ca-rich garnets marked by prograde compositional zoning. The thermodynamic P-T calculations revealed that the core to rim compositional change in these garnets corresponds to an increase in both pressure and temperature of up to 1.5 kbar and 50 °C (Jeřábek et al., 2008). Based on this evidence, they concluded that the formation of subhorizontal S_{A1} fabric is associated with burial of the Vepor Unit and not its exhumation as previously thought (Snopko, 1967; 1971; Hók, 1993; Plašienka, 1993). Furthermore, it has been proposed that the Vepor Unit experienced an Early Cretaceous pure shear dominated E-W orogen-parallel flow in the lower crust triggered by the orogenic thickening due to overthrusting of the Gemer Unit from the south (Jeřábek et al., 2008, 2012).

The thrusting along the Gemer-Vepor interface most likely led to the formation of imbricated structure revealed in the studied area by the bottom to top structural succession of basement orthogneiss, cover quartzite, garnet bearing schist, chloritoid-kyanite schist and cover quartzite (Plašienka, 1980; 1984). The subhorizontal S- S_{A1} fabric in these rocks is associated with the growth of phengite and garnet bearing assemblages (Figs. 5, 6). The garnets in the garnet bearing schist sample BZ188 are characterized by two compositional

varieties, which show identical chemical composition and zoning patterns as garnets that were previously reported from the Blh Valley to the southwest from the studied area (Vozárová and Krištín, 1985; Korikovský et al., 1990; Jeřábek et al., 2008). There, the garnet I cores and garnet II rims have been interpreted as Variscan and Alpine with P-T estimates of ~580 °C at ~6 kbar and 510-540 °C at 8-9 kbar, respectively (Jeřábek et al., 2008). Based on the presence of the two generations garnet in the studied schists, we interpret these rocks as parts of an imbricated Veporic basement that overthrusts Permian cover quartzites. This interpretation contrasts with previously assumed Carboniferous deposition age and Veporic cover affinity (Planderová and Vozárová, 1978; Vozárová and Vozár, 1988) or Gemic affinity of these schists (Plašienka, 1984).

The observed transversal growth of chloritoid and kyanite with respect to the S fabric (Fig. 6d) documented in the chloritoid-kyanite schist suggests an inter-tectonic growth of this assemblage, thus distinctly separating the formation of S and C fabrics (see also Jeřábek et al., 2012). The chloritoid and kyanite bearing assemblage in these schists has been used to constrain metamorphic P-T conditions of 6-8 kbar and 530-560 °C (Lupták et al., 2000). The distinct white mica compositions revealed from the structurally lower and upper belt of cover quartzites (Fig. 1, 6) might indicate a difference in metamorphic grade that is most likely related to the hanging wall and footwall position of the two belts with respect to the detachment shear zone crosscutting the imbricated structure of the Gemer-Vepor contact zone.

The S-C_{A2} fabrics developed within this shear zone are defined by lower grade chlorite- and muscovite bearing assemblage (Figs. 5, 6) and show systematic top-to-the-east sense of shear observed either macroscopically (Fig. 2) or inferred from the inclination of quartz c-axis single girdle CPO's (Fig. 3b). These metamorphic and kinematic observations are consistent with the activity of the major detachment shear zone at the Gemer-Vepor boundary associated with exhumation and unroofing of the Vepor basement (Plašienka et al., 1999; Janák et al., 2001; Jeřábek et al., 2012). The Alpine metamorphic field gradient across this detachment is characterized by rapid transition from low grade metamorphism in the hanging wall Gemer Unit and Veporic Permo-Triassic Foederata cover to higher grade metamorphism within the footwall Permian quartzites and arkoses, and Vepor basement (Lupták et al., 2000; 2003). The main detachment is located within the Permian quartzitic-arkosic rocks as suggested by sharp metamorphic contrast between the muscovite bearing arkose sample BZ172 and chloritoid-kyanite schist samples BZ183, BZ345 and BZ351 (for the position of the detachment see map

in Fig. 1b). Towards the structural footwall in the west, the garnet bearing basement schist (sample BZ188, Fig. 1) and underlying phengite bearing Permian quartzite (sample BZ171, Fig. 1) are expected to record similar metamorphic conditions as the chloritoid-kyanite schists, which are in turn fairly similar to the basement metamorphic conditions in the west.

Quartz microstructures and textures from S and C fabrics corroborate well the above-discussed metamorphic character of both fabrics. Larger quartz grain size together with the transition from basal $\langle a \rangle$ to prism $\langle c \rangle$ slip systems within the S fabric point to medium metamorphic conditions and water saturated environment (Okudaira et al., 1995), which is consistent with 550 °C obtained from the fabric opening thermometer (Kruhl, 1996; 1998; Morgan and Law, 2004). On the other hand, the smaller quartz grain size and the activity of rhomb $\langle a \rangle$ and prism $\langle a \rangle$ slip systems within the C fabric is characteristic for greenschist facies metamorphic conditions (e.g. Stipp et al., 2002). Following the interpretation of (Kilian et al., 2011), the inclination of the surface ODF maximum with respect to orientation of particle ODF maximum and C fabric (Fig. 3) is related to quartz crystal preferred orientation being dominated by rhomb $\langle a \rangle$ and prism $\langle a \rangle$ slip systems. Thus it is suggested that the surface ODF maximum together with overall monocline symmetry of surface ODF within the recrystallized C tails is promoted by high amount of rhombohedral grain boundaries (Kuntcheva et al., 2006).

The dated monazite appears in close association with the inter-tectonic chloritoid and kyanite bearing assemblage (Fig. 8a, b) indicating that monazite formation post-dates the burial-related S fabric. For this reason, the U-Th-Pb concordia age of 97 ± 4 Ma (Fig. 9) should be treated as the limiting age for the development of S fabric in this region. On the contrary, the C fabrics are associated with exhumation of the Vepor Unit and thus their formation age can be constrained by the previously published $^{40}\text{Ar}/^{39}\text{Ar}$ cooling ages. The in situ $^{40}\text{Ar}/^{39}\text{Ar}$ UV laser probe dating of white mica (Janák et al., 2001) from chloritoid-kyanite schist below the main detachment provided mean age of 73 ± 8 Ma (± 1 sigma, sample HAN2). The same authors obtained similar ages of 72 ± 7 Ma and 77 ± 9 Ma from two other basement metapelite samples to the west of the studied area. On the other hand, large number of $^{40}\text{Ar}/^{39}\text{Ar}$ cooling ages obtained by step-heating method from micas in the Veporic basement and cover concentrate between 87-83 Ma (Maluski et al., 1993; Dallmeyer et al., 1996; Kováčik et al., 1996; Putiš et al., 2009) indicating slightly older age of the exhumation process. One way or the other, these geochronological constraints indicate at least 10 million years time gap between the formation of S and C fabrics.

10 Conclusions

Independent, kinematically unrelated S-C fabrics have been identified in the Alpine metamorphosed rocks of the Central West Carpathians along the boundary between major basement-cover Gemer and Vepor units. The S-C fabrics occur within a major detachment shear zone, which crosscuts the earlier imbricated structure related to overthrusting of the Gemer Unit over Vepor. The evidence from deformation microstructures, petrology and geochronology, suggests that the S fabric formed during Early Cretaceous subhorizontal lateral flow associated with overthrusting of the Gemer Unit and burial of the Vepor Unit, while the C fabric originated via Late Cretaceous extensional shearing within the major detachment shear zone associated with exhumation of the Vepor Unit.

Acknowledgements

This work was supported by the research grant from the Czech Science Foundation GACR 205/09/1041, the Ministry of Education, Youth and Sports of the Czech Republic Research Plan No. MSM0021620855 and Charles University Science Foundation GAUK 5041/2012. F. Finger and R. Vojtko are thanked for their careful reviews and D. Plašienka for editorial work.

References

- Aftalion, M., Bibikova, E.V., Bowes, D.R., Hopgood, A.M., Perchuk, L.L. (1991). Timing of early Proterozoic collisional and extensional events in the granulite-gneiss-charnockite-granite complex, Lake Baikal, USSR: A U-Pb, Rb-Sr and Sm-Nd isotopic study. *Journal of Geology* 99, 851-861.
- Aftalion, M., Bowes, D.R., Dash, B., Dempster, T.J. (1988). Late Proterozoic charnockites in Orissa, India: A U-Pb and Rb-Sr isotopic study. *Journal of Geology* 96, 663-676.
- Agard, P., Augier, R., Monié, P. (2011). Shear band formation and strain localization on a regional scale: Evidence from anisotropic rocks below a major detachment (Betic Cordilleras, Spain). *Journal of Structural Geology* 33, 114-131.
- Berthé, D., Choukroune, P., Jegouzo, P. (1979). Orthogneiss, mylonite and noncoaxial deformation of granites: the example of the South Armorican Shear Zone. *Journal of Structural Geology* 1, 31-42.
- Bibikova, E.V., Cambel, B., Korikovskiy, S.P., Broska, I., Gracheva, T.V., Makarov, V.A., Arakeljants M.M., (1988). U-Pb and K-Ar isotopic dating of Sinec (Rimavica) granites (Kohút zone of Veporides). *Geologica Carpathica* 41, 427-436.

Dallmeyer, R.D., Neubauer, F., Handler, R., Fritz, H., Muller, W., Pana, D., Putiš, M. (1996). Tectonothermal evolution of the internal Alps and Carpathians: Evidence from $^{40}\text{Ar}/^{39}\text{Ar}$ mineral and whole-rock data. *Eclogae Geologicae Helvetiae* 89, 203–228.

Faryad, S.W. (1990). Gneiss-amphibolite complex of the Gemericum. *Mineralia Slovaca* 22, 303-318.

Faryad, S.W. (1991). Pre-Alpine metamorphic events in Gemericum. *Mineralia Slovaca* 23, 395-402.

Faryad, S.W., Henjes-Kunst, F. (1997). Petrological and K-Ar and ^{40}Ar - ^{39}Ar age constraints for the tectonothermal evolution of the high-pressure Meliata unit, Western Carpathians (Slovakia). *Tectonophysics* 280, 141-156.

Gapais, D., White, S.H. (1982). Ductile shear bands in naturally deformed quartzite. *Textures and Microstructures* 5, 1-17.

Heilbronner, R., (2000). Automatic grain boundary detection and grain size analysis using polarization micrographs or orientation images. *Journal of Structural Geology* 22, 969-981.

Hók, J., Kováč, P., Madarás, J. (1993). Extensional tectonics of the western part of the contact area between Veporicum and Gemericum (Western Carpathians). *Mineralia Slovaca* 25, 172-176 (in Slovak with English summary).

Hovorka, D., Ivan, P., Jilemnická, L., Spišiak, J. (1988). Petrology and geochemistry of metabasalts from Rakovec (Paleozoic of Gemeric Group, Inner Western Carpathians). *Geologica Carpathica* 39, 395-425.

Hraško, L., Kotov, A.B., Salnikova, E.B., Kovach, V.P. (1998). Enclaves in the Rochovce granite intrusion as indicators of the temperature and origin of the magma. *Geologica Carpathica* 49, 2, 125-138.

Janák, M., Plašienka, D., Frey, M., Cosca, M., Schmidt, S.T., Lupták, B., Méres, Š. (2001). Cretaceous evolution of a metamorphic core complex, the Veporic unit, Western Carpathians (Slovakia): P–T conditions and in situ $^{40}\text{Ar}/^{39}\text{Ar}$ UV laser probe dating of metapelites. *Journal of Metamorphic Geology* 19, 197–216.

Jeřábek, P., Faryad, S.W., Schulmann, K., Lexa, O., Tajčmanová, L. (2008). Alpine burial and heterogeneous exhumation of Variscan crust in the West Carpathians: insight from thermodynamic and argon diffusion modelling. *Journal of Geological Society London* 165, 479-498.

Jeřábek, P., Lexa, O., Schulmann, K., Plašienka, D. (2012). Inverse ductile thinning via lower crustal flow and fold-induced doming in the West Carpathian Eo-Alpine collisional wedge. *Tectonics*, 31 (5), doi:10.1029/2012TC003097.

Kamenický, L. (1977). Contact metamorphism in the aureole of the Rimavica granite (West Carpathians Mts.). *Mineralia Slovaca* 9, 3, 161-178.

Keller, L.M., Stipp, M. (2011). The single-slip hypothesis revisited: Crystal-preferred

orientations of sheared quartz aggregates with increasing strain in nature and numerical simulation. *Journal of Structural Geology* 33, 1491-1500.

Kilian, R., Heilbronner, R., Stünitz, H. (2011). Quartz microstructures and crystallographic preferred orientation: Which shear sense do they indicate? *Journal of Structural Geology* 33, 1446-1466.

Klinec, A. (1966). On the structure and evolution of the Veporic crystalline unit. *Západné Karpaty* 6, 7-28 (in Slovak).

Klinec, A., Macek, J., Dávidová, Š., Kamenický, L. (1980). Rochovce granite in the contact zone between the Veporicum and Gemericum Units. *Geologické Práce, Správy*, 74, 130-112 (in Slovak).

Korikovskiy, S.P., Dupej, J., Boronikhin, V.A., Zinovieva, N.G. (1990). Zoned garnets and their equilibria in mica schists and gneisses of Kohút crystalline complex, Hnúšťa region, Western Carpathians. *Geologica Carpathica* 41, 2, 99-124.

Košler, J., Tubrett, M., Sylvester, P. (2001). Application of laser ablation ICP-MS to U–Th–Pb dating of monazite. *Geostandards Newsletter* 25, 375-386.

Kováčik, M., Král', J., Maluski, H. (1996). Metamorphic rocks in the Southern Veporicum basement: their Alpine metamorphism and thermochronologic evolution. *Mineralia Slovaca* 28, 185-202 (in Slovak with English summary).

Kozur, H., Mock, R. (1973). Zum Alter und zur tektonischen Stellung der Meliata-Serie des Slowakischen Karstes. *Geologický zborník Geologica Carpathica* 24, 365–374.

Kruhl, J.H. (1996). Prism- and basal-plane parallel subgrain boundaries in quartz: a microstructural geothermobarometer. *Journal of Metamorphic Geology* 14, 581-589.

Kruhl, J.H. (1998). Reply to: Okudaira T., Takeshita T. and Toriumi T. 1998: Prism- and basal-plane parallel subgrain boundaries in quartz : a microstructural geothermobarometer. *Journal of Metamorphic Geology* 16, 141-146.

Kuntcheva, B., Kruhl, J.H., Kunze, K. (2006). Crystallographic orientations of high-angle grain boundaries in dynamically recrystallized quartz: first results. *Tectonophysics* 421, 331-346.

Lexa, O. (2003). Numerical approach in structural and microstructural analyses. PhD Thesis, Charles University in Prague.

Lexa, O., Schulmann, K., Ježek, J. (2003). Cretaceous collision and indentation in the West Carpathians: View based on structural analysis and numerical modeling. *Tectonics* 22, 1066-1081.

Lister, G.S., Snoke, A.W. (1984). S-C Mylonites. *Journal of Structural Geology* 6, 617-638.

Lister, G.S., Williams, P.F. (1979). Fabric development in shear zones: theoretical controls and observed phenomena. *Journal of Structural Geology* 1, 283-297.

Lupták, B., Janák, M., Plašienka, D., Schmidt, S.T. (2000). Chloritoid-kyanite schists from the Veporic unit, Western Carpathians, Slovakia: implications for Alpine (Cretaceous) metamorphism. *Schweiz. Mineral. Petrogr. Mitteilungen* 213-223.

Lupták, B., Janák, M., Plašienka, D., Schmidt, S.T. (2003). Alpine low-grade metamorphism of the Permian-Triassic sedimentary rocks from the Vepor Superunit, western Carpathians: phyllosilicate composition and “crystallinity” data. *Geologica Carpathica* 54, 367-375.

Maluski, H., Rajlich, P., Matte, P. (1993). ^{40}Ar - ^{39}Ar dating of the Inner Carpathians Variscan basement and Alpine mylonitic overprinting. *Tectonophysics* 223, 313–337.

Michalko, J., Bezák, V., Král', J., Huhma, H., Mantari, I., Vaasjoki, M., Broska, I., Hraško L. (1998). U/Pb data of the Veporic granitoids (Western Carpathians). *Krystalinikum* 24, 91-104.

Montel, J.-M., Foret, S., Veschambre, M., Nicollet, C., Provost, A. (1996). Electron microprobe dating of monazite. *Chemical Geology* 131, 37–53.

Morgan, S.S., Law, R.D. (2004). Unusual transition in quartzite dislocation creep regimes and crystal slip systems in the aureole of the Eureka Valley–Joshua Flat–Beer Creek pluton, California: a case for anhydrous conditions created by decarbonation reactions. *Tectonophysics* 384, 209-231.

Okudaira, T., Takeshita, T., Hara, I., Ando, J.-I. (1995). A new estimate of the conditions for transition from basal $\langle a \rangle$ to prism $[c]$ slip in naturally deformed quartz. *Tectonophysics* 250, 31-46.

Panozzo, R. (1983). Two-dimensional analysis of shape-fabric using projections of digitized lines in a plane. *Tectonophysics* 95, 279-294.

Panozzo, R. (1984). Two-dimensional strain from the orientation of lines in a plane. *Journal of Structural Geology* 6, 215-221.

Panozzo Heilbronner, R., Pauli, C. (1993). Integrated spatial and orientation analysis of quartz c-axes by computer-aided microscopy. *Journal of Structural Geology* 15, 369-382.

Passchier, C.W., Trouw, R.A.J. (2005). *Microtectonics*, 2nd ed. Springer Verlag.

Petrasová, K., Faryad, S.W., Jeřábek, P., Žáčková, E. (2007). Origin and metamorphic evolution of magnesite-talc and adjacent rocks near Gemerská Poloma, Slovak Republic. *Journal of Geosciences* 52, 125-132.

Planderová, E., Vozárová, A. (1978). Upper Carboniferous in southern Veporides. *Geologické Práce, Správy* 70, 129-141.

Plašienka, D. (1980). Nappe position of the Hladomorná dolina Group on the Foederata Group in the Dobšiná half-window. *Geologický Zborník Geologica Carpathica* 31, 4, 609-617.

Plašienka, D. (1984). Represents the Markuška nappe an interconnecting element between the Veporic and Gemeric units? *Mineralia Slovaca* 16, 2, 187-193 (in Slovak with English summary).

Plašienka, D. (1993). Structural pattern and partitioning of deformation in the Veporic Foederata cover unit (Central Western Carpathians), in: Rakús M. and Vozár J. (Eds.): *Geodynamic Model and Deep Structure of the Western Carpathians*. pp. 269-277.

Plašienka, D., Grecula, P., Putiš, M., Kováč, M., Hovorka, D. (1997). Evolution and structure of the Western Carpathians: an overview. In: Grecula P., Hovorka M., Putiš M. (Eds.), *Geological evolution of the Western Carpathians*. *Mineralia Slovaca - Monograph*, pp. 1-24i.

Plašienka, D., Janák, M., Lupták, B., Milovský, R., Frey, R. (1999). Kinematics and metamorphism of a Cretaceous core complex: the Veporic unit of the Western Carpathians. *Phys. Chem. Earth (A)* 24, 651-658.

Platt, J.P. (1979). Extensional crenulation cleavage. In: Cobbold P.R. and Fergusson C.C. (Eds.): *Description and Origin of Spatial Periodicity in Tectonic Structures*, Report on a Tectonic Studies Group Conference. *Journal of Structural Geology* 1. Pergamon, Oxford - New York, International, pp.95-96.

Platt, J.P. (1984). Secondary cleavages in ductile shear zones. *Journal of Structural Geology* 6, 439-442.

Platt J.P., Vissers, R.L.M. (1980). Extensional structures in anisotropic rocks. *Journal of Structural Geology* 2, 397-410.

Poller, U., Uher, P., Janák, M., Plašienka, D., Kohút, M. (2001). Late Cretaceous age of the Rochovce granite, Western Carpathians, constrained by U-Pb single zircon dating with cathodoluminescence imaging. *Geologica Carpathica* 52, 41-47.

Ponce L.M.I., Choukroune, P. (1980). Shear zones in the Iberian Arc. *Journal of Structural Geology* 2, 63-68.

Putiš, M., Frank, W., Plašienka, D., Siman, P., Sulák, M., Biroň, A. (2009). Progradation of the Alpidic Central Western Carpathians orogenic wedge related to two subductions: constrained by $^{40}\text{Ar}/^{39}\text{Ar}$ ages of white micas. *Geodinamica Acta* 1-3, 31-56.

Rozlosznik, P. (1935). Die geologische Verhaeltnisse der Gegend von Dobšiná. *Geologica Hungarica*, Budapest 1-118.

Schmid, S.M., Casey, M. (1986). Complete fabric analysis of some commonly observed quartz c-axis patterns. In: Hobbs B.E. and Heard H.C. (Eds.): *Mineral and Rock Deformation: Laboratory Studies; the Paterson Volume*, *Geophysical Monograph Series*, vol. 36. American Geophysical Union, Washington DC, pp. 263-286.

Schönenberg, R. (1946). Geologische Untersuchungen am Nordwestrand des Zips-Gömörer Erzgebirges (Karpaten). *Zeit. Dtsch. Geol. Gesell.*, 98, 70-119.

Simpson, C., Schmid, S.M. (1983). An evaluation criteria to deduce the sense of movement in sheared rocks. *Geol. Soc. Am. Bull.* 94, 1281-1288.

Snopko, L. (1967). Die Bedeutung der kleintektonischen Elemente bei der Lösung einiger geologischen Probleme des gemeriden Paläozoikum. *Sborník geologických vied, Západné Karpaty*, 8, 7-49 (in Slovak with German summary).

Snopko, L. (1971). The course of schistosity in the Paleozoic of the Spišsko-Gemerské Rudohorie Mountains. *Geologické práce, Správy.* 57, 207-213 (in Slovak with English summary).

Stipp, M. (2002). The eastern Tonale fault zone: a “natural laboratory” for crystal plastic deformation of quartz over a temperature range from 250 to 700°C. *Journal of Structural Geology* 24, 1861-1884.

Sulák, M., Kaindl, R., Putiš, M., Sitek, J., Krenn, K., Tóth, I. (2009). Chemical and spectroscopic characteristics of potassium white micas related to polystage evolution of the Central Western Carpathians orogenic wedge. *Lithos* 113, 709-730.

Tischendorf, G., Rieder, M., Foerster, H.-J., Gottesmann, B., Guidotti, C.V. (2004). A new graphical presentation and subdivision of potassium micas. *Mineralogical Magazine* 68, 649-667.

Tomek, Č. (1993). Deep crustal structure beneath the central and inner West Carpathians. *Tectonophysics* 226, 417–431.

Vozárová, A. (1990). Development of metamorphism in the Veporic/Gemeric contact zone (Western Carpathians). *Geologický Zborník Geologica Carpathica* 41, 475-502.

Vozárová, A., Krištín, J. (1985). Changes in chemical composition of garnets and biotites from contact aureole of Alpine granitoides in southern part of Veporicum. *Západné Karpaty, sér. mineralógia, petrografia, geochemia, metalogenéza*, 10, 199-221 (in Slovak with English summary.)

Vozárová, A., Vozár, J. (1988). Late Paleozoic in West Carpathians. *GÚDŠ*, Bratislava.

Vrána, S. (1964). Chloritoid and kyanite zone of Alpine metamorphism on the boundary of the Gemerides and the Veporides (Slovakia). *Krystalinikum* 2, 125-143.

Vrána, S. (1966). Alpidische metamorphose der granitoiden und der Foederata Serie im mittelteil der Veporiden. *Zborník geologických vied, Západné Karpaty* 6, 29-84.

White, S.H. (1979). Grain and sub-grain size variations across a mylonite zone. *Contributions to Mineralogy and Petrology* 70, 193-202.

White, S.H., Burrows, S.E., Carreras, J., Shaw, N.D., Humphreys, F.J. (1980). On mylonites in ductile shear zones. *Journal of Structural Geology* 2, 175-187.

MAJOR SOFTENING AT BRITTLE-PLASTIC TRANSITION DUE TO INTERPLAY BETWEEN CHEMICAL AND DEFORMATION PROCESSES: AN INSIGHT FROM EVOLUTION OF SHEAR BANDS IN THE SOUTH ARMORICAN SHEAR ZONE

Zita Bukovská^{1,2}, Petr Jeřábek^{1,2}, Luiz F.G. Morales³

¹ Charles University in Prague, Faculty of Science, Institute of Petrology and Structural Geology, Albertov 6, 12843 Prague 2, Czech Republic

² Czech Geological Survey, Klárov 3, 118 21 Prague 1, Czech Republic

³ Helmholtz Centre Potsdam, German Research Centre GFZ, Section 3.2, Telegrafenberg, 14476 Potsdam, Germany

Abstract

The formation of S-C fabrics in the South Armorican Shear Zone has been evaluated by detailed microstructural study. Our observations suggest that the two fabrics formed at distinct P-T conditions indicating conditions >550 °C for the S fabric and 300-350 °C at 100-400 MPa for the C fabric/shear bands. The evolving microstructure within shear bands revealed switches in deformation mechanisms related to positive feedbacks between deformation and chemical processes and imposed mechanical constraints on evolution of the brittle-plastic transition. Three stages of shear band evolution were identified. Stage I documents initiation of shear bands via formation of microcracks with possible yielding differential stresses up to 250 MPa. Stage II is associated with subgrain rotation recrystallization of quartz and coeval dissolution-precipitation creep of microcline. Recrystallized quartz grains show continual increase in size, and decrease in stress and strain rates from 94 MPa to 17-26 MPa and $1.8 \cdot 10^{-14} \text{ s}^{-1}$ - $9 \cdot 10^{-17} \text{ s}^{-1}$ associated with deformation partitioning into weaker microcline layer. Data from quartz allowed us to set some mechanical constrains for dissolution-precipitation creep of microcline which at our estimated P-T conditions suggests creep at 17-26 MPa differential stress and $1.8 \cdot 10^{-15} \text{ s}^{-1}$ strain rate. Stage III is characterized by localized slip along white mica bands accommodated by dislocation creep at strain rate $1.8 \cdot 10^{-14} \text{ s}^{-1}$ and stress 5.75 MPa. Our mechanical data point to dynamic evolution of the brittle-plastic transition characterized by major weakening to strengths >10 MPa. Such non-steady-state evolution may be common in crustal shear zones especially when phase transformations are involved.

Keywords: *Brittle-plastic transition, dissolution-precipitation creep, quartz and mica plasticity, rheology, S-C fabrics, shear bands, South Armorican Shear Zone*

1 Introduction

Zones of intense deformation such as faults and shear zones are an expression of strain localization (e.g. White et al., 1980; Schmid, 1982; Rutter et al., 2001; Gueydan et al., 2003). The phenomenon of localization has been recognized across the entire lithosphere (e.g. Karato, 1983; Wilks and Carter, 1990; Crider and Peacock, 2004) thus the overall rheological response of the lithosphere to applied stress is strongly influenced by this process (Rutter, 1999; Bercovici, 2003). It is generally accepted that deformation is more distributed with increasing depth and temperature which, in the context of the lithosphere compositional stratification, implies several vertically alternating layers of either localized or distributed deformation (e.g. Platt and Behr, 2011). In contrast, recent studies demonstrated that highly localized deformation can be maintained under conditions of presumed distributed deformation (e.g. Chopin et al., 2012; Menegon et al., 2013; Okudaira et al., 2015). In simple terms, the maintenance of localized shear in ultramylonites demonstrates high strength contrast between the weaker shear zone and stronger wall rock whereas the two strengths must be comparable in the case of distributed shear in mylonites (Platt and Behr, 2011). The maintenance of localized shear will thus lead to an underestimation of the integral lithospheric strength. Recently, numerous small-scale studies have concentrated on rheological aspects of initiation and evolution of shear zones mainly in quartzo-feldspathic rocks (Pennacchioni and Mancktelow, 2007; Oliot et al., 2010; Kilian et al., 2011; Chopin et al., 2012; Goncalves et al., 2012; Menegon et al., 2013; Oliot et al., 2014). The initiation of shear zones is controlled by mechanical yielding of a rock (Ranalli, 1987) while their subsequent evolution is controlled by grain-scale processes which reflect complex interaction between metamorphism, metasomatism and deformation so typical for natural shear zones (Keller et al., 2004; Jeřábek et al., 2007; Oliot et al., 2010; Goncalves et al., 2012).

Small scale shear zones, called shear bands, C or C' fabrics, or extensional crenulation cleavage, crosscutting a metamorphic foliation at gentle to moderate angles are frequent phenomenon in major shear zones (Berthé et al., 1979 a, b; Platt and Vissers, 1980; White et al., 1980; Gapais and White, 1982; Platt, 1984). These extensively studied deformation structures clearly indicate localization of deformation associated with (i) pre-existing fractures or discontinuities (e.g. Means, 1995; Fousseis and Handy, 2008), (ii) strain partitioning (Krohe, 1990; Passchier, 1991) or (iii) reaction softening (Stünitz and Tullis, 2001). In contrast to recent studies on standard shear zones, most of the studies of shear bands focussed on their initiation and geometry and not on their subsequent evolution.

In this study, we present detailed characterization of formation and evolution of shear bands in granitoids from the type-locality in the South Armorican Shear Zone (Berthé et al., 1979 a, b). The analysis of microstructure, texture and chemistry of minerals from the studied shear bands revealed the effects of positive feedback between deformation and chemical processes resulting into switches in dominant deformation mechanism and consequently to dramatic weakening of these small-scale shear zones in the conditions of brittle-plastic transition. Furthermore, the evolution of studied shear bands documents that rheology of these shear zones may be rather dynamic allowing for switches between localized and distributed deformation behaviour, which is also relevant for the evolution of large-scale shear zones.

2 Sample localization and description

South Armorican Shear Zone (SASZ) in European Variscides represents a major tectonic zone separating Central Armorican and South Armorican Massif in France (e.g. Ballèvre et al. 2009, Gumiaux et al., 2004). The subvertical shear zone has approximately WSW-ENE strike with similar branches extending over several hundred kilometres from westernmost Brittany to Vendée-Poitou region (Fig. 1). In the studied area, the shear zone affects Variscan and Early Palaeozoic intrusive rocks emplaced to 3-12 km depth (338-329 Ma) (Tartèse and Boulvais, 2010; Tartèse et al., 2012) and can be traced also into the sedimentary cover. The SASZ is right-lateral shear zone with a steep foliation and horizontal to subhorizontal lineation showing approximately 40 km of displacement in its northern branch (Gumiaux et al., 2004). The shear zone shows the development of structures called S-C or S-C fabrics which were originally described from Plumelec and Gorvello massif by Berthé et al. (1979 a, b). It has been suggested that the shear deformation in the SASZ records an evolution from ductile to brittle conditions and occurred at 315 – 300 Ma (Tartèse et al., 2012).

The studied orthogneisses to ultramytonites formed from Variscan white mica granites. The studied samples were collected from quarries situated within the SASZ (Fig. 1) with the aim to cover different stages of shear band evolution marked by increasing strain. The studied samples were collected from Lizio granite in the Plumelec abandoned quarry (Fig. 1, SB2; original locality of Berthé et al. (1979 a, b), from Questembert granite in the Lescastel quarry (SB4) and from the Guéhenno granite in the Pasdrun abandoned quarry (SB7) (Fig. 1).

The studied S-C fabrics (Fig. 2a) comprise metamorphic foliation (S fabric) which is crosscut by shear bands (C fabric). Macroscopically, the S fabric is defined by shape preferred orientation of quartz aggregates and porphyroclasts of K-feldspar, white mica and plagioclase.

The S fabric bears stretching lineation defined by shape of quartz aggregates. The C fabric is characterized by discrete zones occupied by fine grained mixture of phases. The C fabric bears mineral lineation defined by spatial arrangement of small white mica grains. The shear bands show regular spacing and the distance between individual shear surfaces decreases with increasing intensity of shear band overprint (Fig. 2a, 3). Both S and C fabrics are steep, generally E-W trending in case of S fabric and NW-SE trending in case of C fabric (Fig. 1). The lineations of both fabrics are horizontal to subhorizontal. The studied thin sections were cut perpendicular to both S and C fabrics, and their intersection, as well as parallel to both (S and C) lineations.

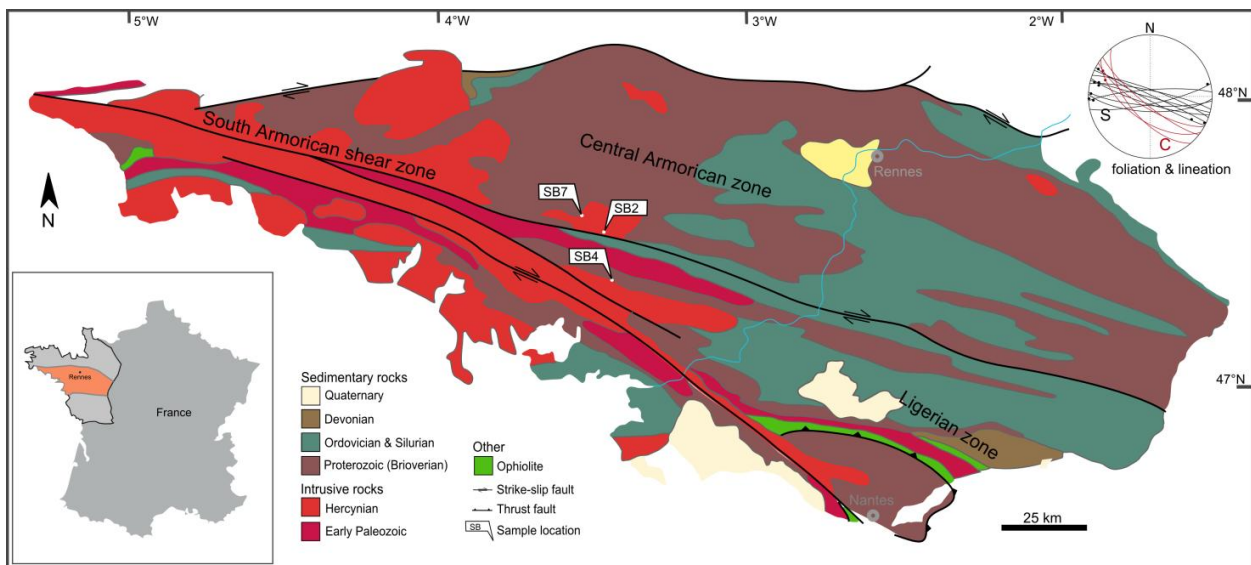


Fig. 1 Simplified geological map of the studied area with location of the studied samples (map modified from Wikimedia Commons, GNU Free Documentation License). The measured orientation of S and C fabrics is shown in the equal area lower hemisphere pole figure. The black and red dots in the pole figure show the orientation of respective lineations.

3 Analytical methods

The characterization of S-C fabrics was performed by using optical and scanning electron microscopes at the Institute of Petrology and Structural Geology, Charles University in Prague. The geometry of S-C fabrics and quantitative microstructural analysis has been evaluated from digitized micrographs by using the polyLX Matlab™ toolbox (Lexa, 2003).

The cathodoluminescence analysis was performed using the TESCAN Vega scanning electron microscope (SEM) at the Charles University in Prague and hot cathodoluminescence at optical microscope Olympus TH3 with HC2-LM system at the Masaryk University in Brno. Semi-quantitative mineral chemistry analyses were initially carried out via EDS analyses

using an Oxford X-Max 50 EDS detector attached to the TESCAN SEM. These analyses were then complemented with quantitative analyses in selected samples using a microprobe JEOL JXA 8200 Superprobe with EDS and WDS operating at Department of Earth Sciences, Free University in Berlin. Chemical data were plotted using the GCDkit (Janoušek et al., 2006). The effective bulk rock chemical analysis of shear bands used for thermodynamic modelling were obtained directly from thin sections by area scanning electron microscopy using the TESCAN Vega at the Institute of Petrology and Structural Geology in Prague.

Electron backscattered diffraction analysis (EBSD) was carried out using the FEI Quanta 3D FEG dual beam machine with an EDAX/TSL EBSD camera and OIM software operating at the GFZ Potsdam. The thin sections were first polished with diamond paste up to a 0.25 μm and then treated with chemical polish using the standard alkaline solution of colloidal silica of 0.015 μm for 4 hours. The operating conditions of the SEM/EBSD were: accelerating voltage of 20 kV, beam current of 8 nm and sample tilt of 70°. In individual EBSD scans, the working distance varied between 12 and 15 mm and the step size varied between 5 and 20 μm . The EBSD data were plotted using the MTEX toolbox in MatlabTM (Hielscher and Schaeben, 2008). The transmission electron microscopy was performed for three thin foils (0.15 μm thick) cut across phase boundaries of quartz – K-feldspar by using the FEI Tecnai G2 F20 X-Twin TEM at GFZ Potsdam. For details related to TEM foil preparation see Wirth (2009).

4 Characterization of S-C fabrics

The studied thin sections revealed that the two fabrics are characterized by distinct microstructures and minerals, which in case of K-feldspar and white mica show two generations. The S fabric is defined by shape preferred orientation of relatively coarse-grained recrystallized quartz aggregates (Fig. 2b) and larger grains of K-feldspar I, plagioclase and white mica I (ca. 0.5-4 mm in size). In contrast, the C fabric shear bands are represented by zones of fine-grained matrix comprising mixed K-feldspar II, quartz and white mica II grains, and in some samples also chlorite (Fig. 2c, d). The studied samples were sorted into series on the basis of increasing intensity of shear band overprint manifested by increasing proportion of C fabric-related matrix at the expense of S fabric-related porphyroclasts and aggregates (Fig. 3). Although it is difficult to directly link the intensity of overprint with strain due to the lack of clear displacement markers, the increasing proportion of C fabric matrix most likely reflects the progressive evolution of shear bands. The series SB4 from the Lescastel quarry (Fig. 1) exemplify the typical proportion of C fabric matrix associated with individual

evolutionary stages (I-III) (Fig. 3d). Stages I and III in most series are characterized by the proportion of C fabric matrix below and above 1.5 % and 8 %, respectively, and stage II has the matrix proportion in between the two values.

Generally, samples characterized by low shear band overprint show short and discrete/thin shear bands while with increasing degree of overprint, shear bands become longer, wider and interconnected. The angle between mean orientation of C and S fabrics in most series shows a gradual increase from $\sim 35^\circ$ for stage I up to $\sim 42^\circ$ for stage III (see rose diagrams in Fig. 3d). Moreover, samples with higher intensity of shear band overprint show greater scatter in orientation of both C and S fabrics (Fig. 3c). It is important to note that with the increasing shear band overprint in stage III when the proportion of C-fabric matrix reaches 13 %, the angle between S and C starts to decrease and both fabrics become parallel/indistinguishable in the ultramylonite samples.

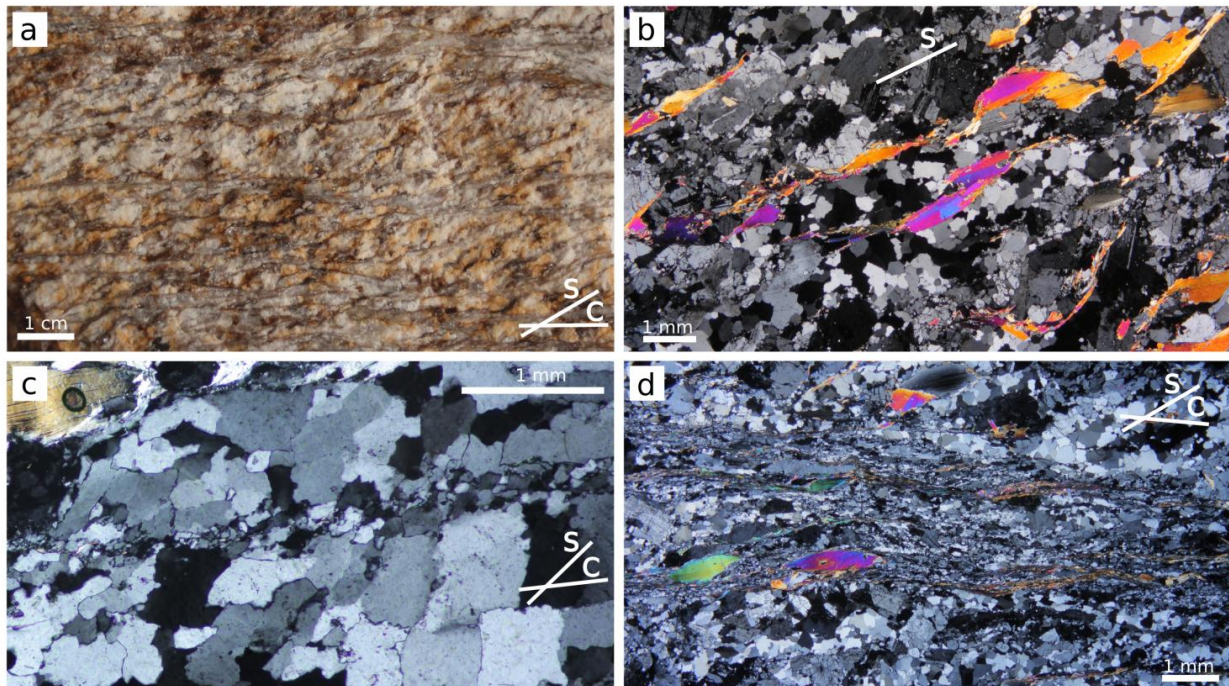


Fig. 2 a) Macrophotograph of orthogneiss sample SB4H showing S-C fabric geometry. b) Microphotograph of S fabric defined by porphyroclasts of K-feldspar, plagioclase, white mica and recrystallized quartz aggregates (sample SB4H, crossed polarizers). c) Microphotograph of thin shear band crosscutting the quartz aggregate (sample SB4H, crossed polarizers). d) Microphotograph of well developed shear band reworking the original S fabric (sample SB4H, crossed polarizers). General orientation of S and C fabrics for each image is indicated by white lines.

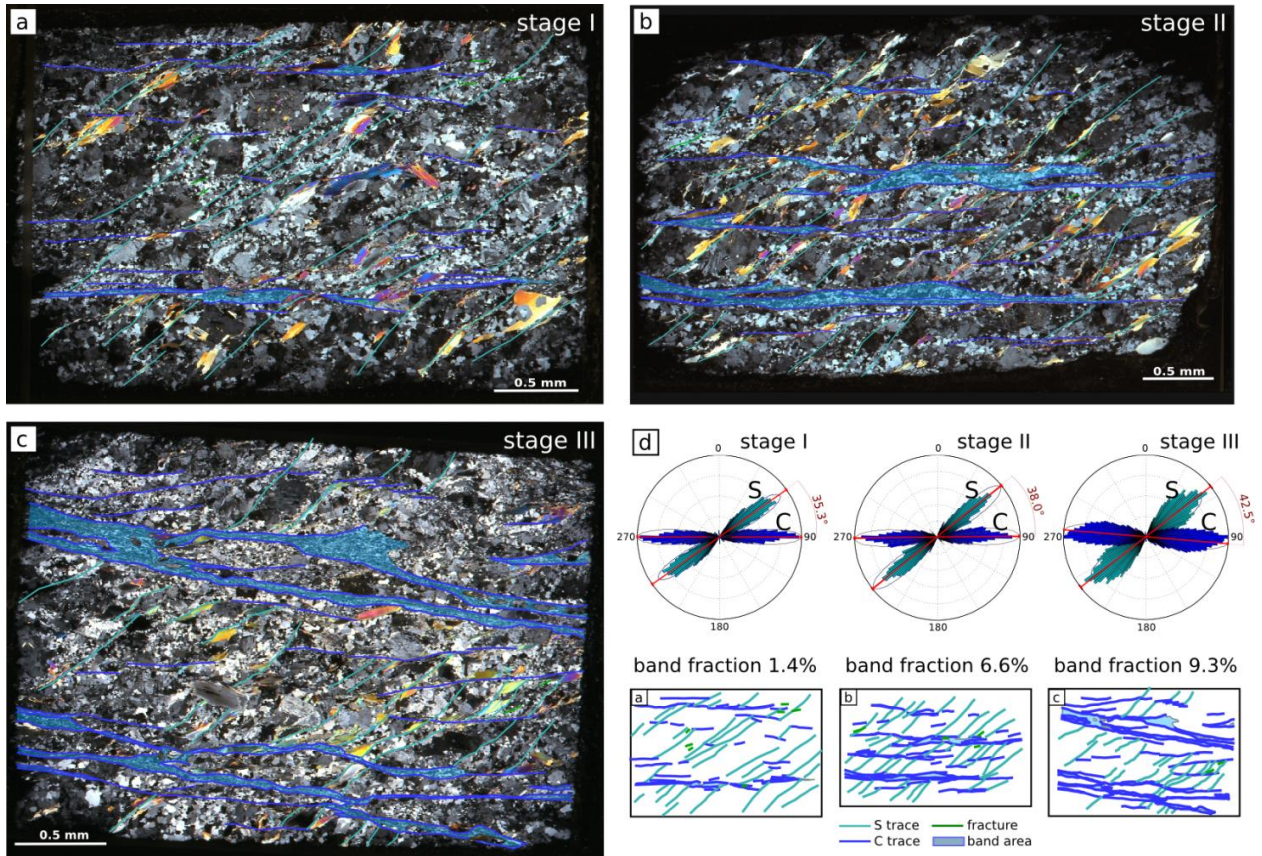


Fig. 3 Thin section scans of three samples (series SB4) show typical evolutionary stages of shear band overprint from lowest in sample SB4B (stage I, a), intermediate in sample SB4D (stage II, b), to highest in sample SB4H (stage III, c). Traces of S-C fabrics are marked in light blue (S) and dark blue (C), and the area occupied by the shear band matrix is highlighted by transparent blue. Microcracks are marked in green. d) The length weighted rose diagrams of segmented traces of S and C fabrics demonstrate orientation relationship between the two fabrics for the three stages (a-c). Mean preferred orientation of S and C is indicated by the thick red line and the standard deviation of orientation 1σ is shown by the red sections along the periphery of diagrams. The angle between mean orientation of S and C fabrics increases towards stage III and the orientation of both fabrics becomes more scattered. The small thin section insets in (d) demonstrate the increasing proportion of shear band matrix from stage I to stage III in (a-c).

4.1 Microcracks and shear bands

Independent of the degree of shear band overprint, all studied samples contain cracks which cross-cut the S fabric and show systematic orientations close to the orientation of shear bands (Fig. 4). The microcracks can be clearly distinguished when cross-cutting the recrystallized quartz aggregates and are best preserved in samples with lower intensity of shear band overprint i.e. in stage I samples. The microcracks typically occur in the vicinity of large white mica I and plagioclase grains, enclosed within quartz aggregates, where they cross-cut quartz grains or follow the existing grain boundaries (Fig. 4a). The orientation of microcracks was traced in the thin section plane from five samples covering the three evolutionary stages. The orientation of traces of microcracks was characterized with respect to

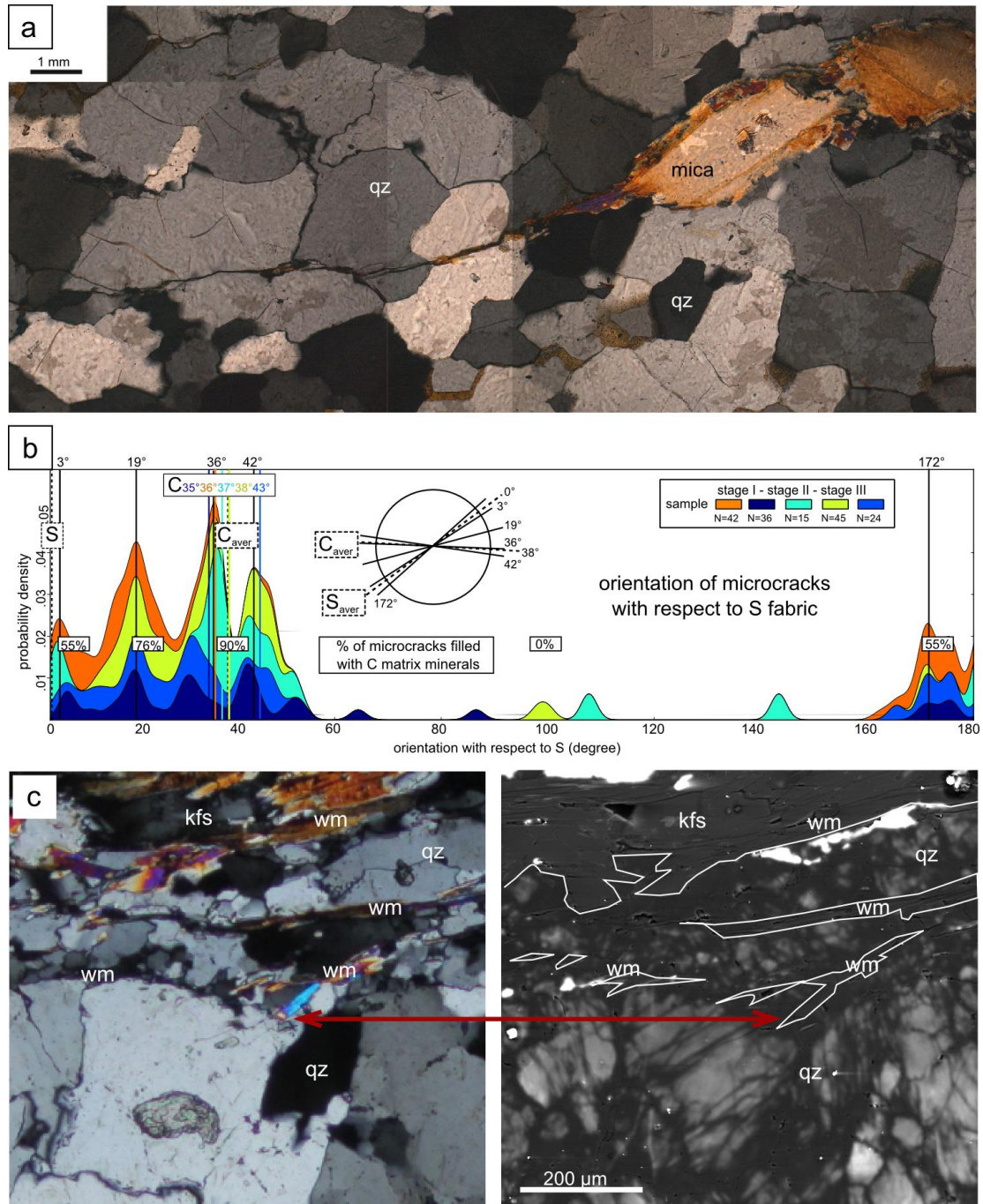


Fig. 4 a) Microphotograph of a microcrack crosscutting recrystallized quartz aggregate. The microcrack is created at the tip of white mica porphyroclast. b) Probability density function of microcrack orientation with respect to the S fabric. The orientation of microcracks was determined in five samples covering all stages of shear band evolution (stage I – III). Individual colours in the diagram correspond to individual samples (SB2A, SB4B, SB4D1, SB4F, SB4H) and N indicates number of measured microcracks in each sample. The S fabric corresponds to 0° orientation while C fabric orientation is indicated by coloured lines for individual samples and black dotted line for average orientation. Summary diagram highlighting the peaks in orientation density of microcracks with respect to the average orientation of S and C fabrics is shown in the circular diagram. c) Optical micrograph and the corresponding cathodoluminescence image show the disruption of quartz aggregate microstructure in the vicinity of a shear band (sample SB4D). The lighter parts of quartz grains correspond to original microstructure, while the darker parts indicate disruption of quartz grains associated with shear bands.

the reference line represented by the S fabric trace and it is shown for all five samples in the cumulative histogram in figure 4b. Here the angles between microcracks and S fabric are plotted using the probability density function. The resulting histogram shows poly-modal orientation distribution with majority of the microcracks occurring close to the orientation of shear bands i.e. at angles between 25° and 45° from the S fabric (Fig. 4b). Other preferred orientations of microcracks are represented by the peak located in between the S and C fabric orientations at 12-25° from S and by two subordinate peaks close to S orientation at angles between 5° and 15° from S (Fig. 4b). Microcracks at high angle to the S fabric are extremely rare. The microcracks are frequently filled with minerals typical from the assemblage observed in the studied shear bands. On the other hand, not all the microcracks are filled and there seem to be a systematic relationship between orientation of microcracks and presence/absence of infill. 55% of microcracks oriented close to the S fabric have the mineral infill with mainly white mica II and sometimes chlorite. Microcracks oriented at 12-25° to S show higher proportion of filled microcracks reaching 76 %, which further increases to 90 % for microcracks close to the shear band orientation (Fig. 4b). These latter microcracks are filled by typical shear band assemblage represented by K-feldspar II, white mica II and chlorite. The microcracks oriented at high angles to the S fabric lack the mineral infill completely. From these observations it is clear that the microcracks have some relationship to shear bands and that they most likely represent their thin precursors. The inflection of coarse-grained quartz microstructure in the recrystallized aggregates was further documented by the cold cathodoluminescence revealing damage of quartz in the vicinity of microcracks (Fig. 4c).

4.2 Mineral chemistry of S and C fabrics

The studied orthogneiss is composed of quartz, K-feldspar, plagioclase, white mica, apatite, zircon, sometimes also chlorite, and accessory tourmaline, monazite, rutile enclosed within biotite, hematite and ilmenite (further description of these rocks can be found in Tartèse and Boulvais (2010)). As the white mica, K-feldspar and plagioclase represent dominant components of the rock as well as the S and C fabrics building elements, our chemical analysis focused on these phases to characterize chemical differences between the two fabrics.

White mica occurs in all studied samples and has been identified in both S and C fabrics. In the S fabric, the white mica I has a form of large grains up to 4 mm in size (Fig. 2b). When affected by the shear bands, the white mica I porphyroclasts bends towards the orientation of C-fabric and/or recrystallize into fine grained white mica II (Fig. 2d). Moreover, small grains

of white mica II form also outside the shear bands. The composition of both varieties of white mica corresponds to muscovite although the white mica II is little more phengitic (Tab. 1). Chemical analyses revealed further compositional differences between the two white micas demonstrated by variation in magnesium, titanium and sodium contents (Fig. 5a). The white mica I has the highest content of titanium (up to 0.08 atoms per formula unit – a.p.f.u.) and sodium (up to 0.07 a.p.f.u.) while the white mica II is low in titanium (up to 0.02 a.p.f.u.) and sodium (up to 0.03 a.p.f.u.), and rich in magnesium (up to 0.17 a.p.f.u., Tab 1, Fig. 5a). The observed differences follow the previously proposed distinction between primary (magmatic) and secondary (metamorphic) muscovites (Miller et al., 1981; Tartèse and Boulvais, 2010). The diagram in Figure 5a shows that some smaller white mica grains in the shear bands have comparable composition to white mica I porphyroclasts implying the presence of reworked porphyroclast relics inside the shear bands. In addition, the white mica II in microcracks is a little higher in magnesium (up to 0.23 a.p.f.u.) and more phengitic (Si up to 3.33 a.p.f.u.) compared to white mica II in the well developed shear bands (Si up to 3.13 a.p.f.u., Tab. 1).

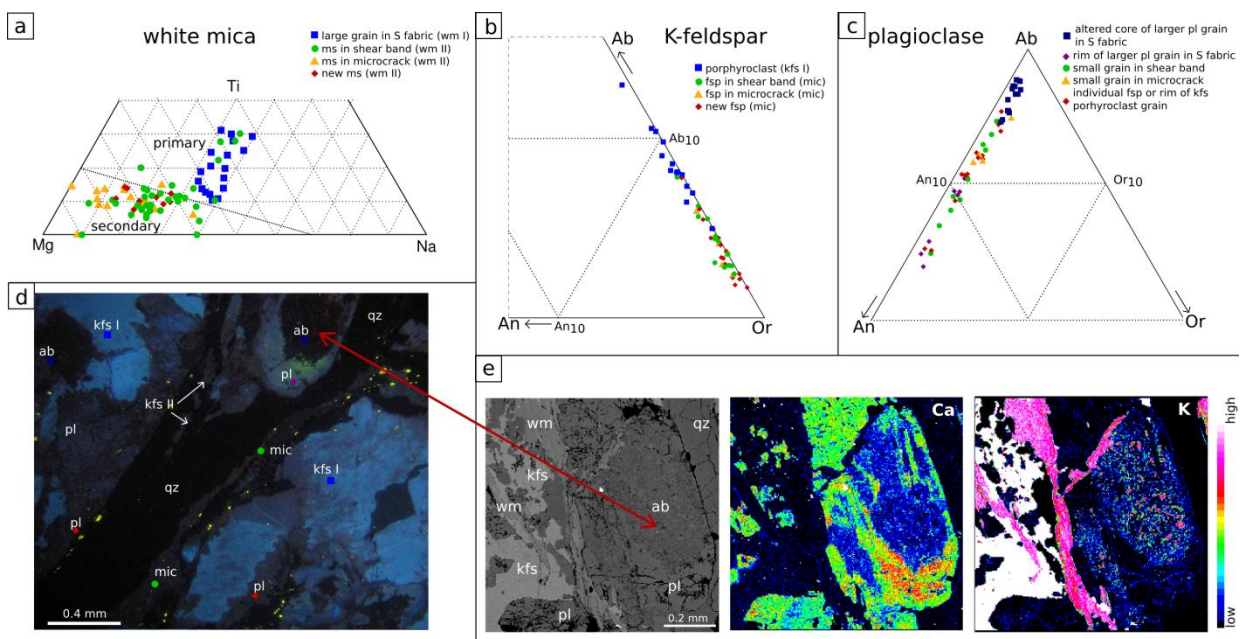


Fig. 5 Chemical composition of white mica and feldspars: a) Mg-Ti-Na ternary diagram shows compositions of white mica grains from different samples and from distinct locations with respect to the C fabric (for colour coding see legend and example in d). b) Anorthite-Albite-Orthoclase ternary diagram shows composition of K-feldspar grains (for colour coding see legend and example in d). c) Anorthite-Albite-Orthoclase ternary diagram shows composition of plagioclase grains (for colour coding see legend and example in d). d) Cathodoluminescence image of a selected region in the vicinity of a shear band (sample SB7C) demonstrates distinct cathodoluminescence for different generations of feldspar grains. For symbols and colour coding of different feldspars see legend in b) and c). e) BSE image and corresponding calcium and potassium element maps from the vicinity of a shear band. Mineral abbreviations used in the figure are: kfs - K-feldspar, pl – plagioclase, qz – quartz, wm – white mica.

K-feldspar occurs in two varieties represented by larger grains (kfs I) with their shape preferred orientation parallel to S fabric and smaller irregular grains (kfs II) within shear bands (Fig. 5). The K-feldspar have composition is similar to the binary solution with orthoclase component in the range of 86.7 – 99.6 %, albite component between 1.7 - 12.9 % and negligible anorthite component between 0 – 0.9% (Fig. 5b, Tab. 1). The large K-feldspar I grains are characterized by higher albite content between 7-13 % while in the K-feldspar II albite component is lower (Fig. 5b). The K-feldspar I is frequently replaced/encircled by irregular rims of plagioclase (Fig. 5c). In some samples these plagioclase rims are mixed with quartz (myrmekites) and form parallel to the S fabric. The Transmission Electron Microscopy revealed that the K-feldspar II in microcracks and shear bands is represented by microcline.

Plagioclase is represented by larger grains with their shape preferred orientation parallel to S fabric (Figs. 2 and 3) and by smaller grains within the S fabric as well as within shear bands. The composition of plagioclase ranges from oligoclase to albite with 80.0 – 97.7% of albite component, 1.7 – 19.5 % anorthite component and minor orthoclase component between 0.4 – 1.9 % (Fig. 5c, Tab. 1). The larger plagioclase grains show systematic zoning pattern with albite rich cores and more anorthite rich rims (Fig. 5d, e). The cores, however, are formed by a mixture of albite and small white mica II grains (Fig. 5e). The rims have the composition of oligoclase which is common also for smaller plagioclase grains in the S fabric and plagioclase rims around K-feldspar I porphyroclast (Fig. 5c, d, e). Small plagioclase grains that are locally present within shear bands have similar compositional range as the above-mentioned S-related plagioclase (Fig. 5c) and thus could represent relict grains that were reworked by shear bands. On the other hand, some of the smaller plagioclase grains in microcracks show more albite rich composition (Fig. 5c) suggesting that albite forms synchronously with shear bands as a stable part of the C fabric related assemblage.

Chlorite is present in a form of individual grains, which are found in microcracks and in the shear bands and their vicinity. The chlorite grains are small, typically up to 0.5 mm, and their XMg content reaches 0.15 – 0.21 (Tab. 1).

4.3 P-T conditions of shear band formation

Phase equilibrium approach was used to characterize P-T conditions of shear band formation at locality SB4 in the Questembert granite (Fig. 1). The bulk chemical composition (Tab. 2) of the studied shear bands was estimated by using the scanning mode of the electron microscope and by covering/averaging several shear band domains in thin sections from stage

mineral	K-feldspar				plagioclase			white mica			chlorite
	porphyroclast	grain in microcrack	grain in shear band	newly grown grain	larger grain rim	grain in shear band	larger grain altered core	large grain core	grain in microcrack	grain in shear band	
generation	kfs I	kfs II (mic)	kfs II (mic)	kfs II (mic)	pl	pl	ab	wm I	wm II	wm II	chl
SiO ₂	64.26	64.66	64.11	63.95	64.61	64.61	67.28	45.87	49.73	46.32	37.48
TiO ₂	0.04	0.00	0.02	0.00	0.00	0.00	0.00	0.60	0.00	0.34	1.33
Cr ₂ O ₃	0.01	0.01	0.03	0.01	0.00	0.00	0.04	0.01	0.00	0.02	0.00
Al ₂ O ₃	18.51	18.53	18.02	18.13	21.75	21.75	19.93	34.21	34.57	33.30	21.80
FeO	0.02	0.00	0.02	0.00	0.01	0.01	0.00	1.82	0.50	2.38	19.70
MnO	0.03	0.00	0.04	0.03	0.01	0.01	0.01	0.04	0.00	0.05	0.43
MgO	0.00	0.00	0.02	0.00	0.00	0.00	0.00	0.67	0.82	1.00	1.99
CaO	0.04	0.09	0.03	0.03	2.80	2.80	0.52	0.01	0.00	0.01	0.21
Na ₂ O	0.89	0.46	0.32	0.24	9.63	9.63	11.13	0.44	0.07	0.33	0.08
K ₂ O	15.45	16.22	16.24	16.46	0.21	0.21	0.07	10.77	9.95	10.96	5.53
sum	99.25	99.97	98.84	98.84	99.03	99.03	98.99	94.44	95.65	94.71	88.55
Si	2.98	2.99	3.00	3.00	2.87	2.88	2.98	3.09	3.32	3.12	4.10
Ti	0.00	0.00	0.00	0.00	0.00	0.00	0.00	0.03	0.00	0.02	0.11
Cr	0.00	0.00	0.00	0.00	0.00	0.00	0.00	0.00	0.00	0.00	0.00
Al	1.01	1.01	0.99	1.00	1.14	1.14	1.04	2.72	2.72	2.64	2.81
Fe ³⁺	0.00	0.00	0.00	0.00	0.00	0.00	0.00	0.02	0.00	0.07	0.00
Fe ²⁺	0.00	0.00	0.00	0.00	0.01	0.00	0.00	0.08	0.03	0.06	1.80
Mn	0.00	0.00	0.00	0.00	0.00	0.00	0.00	0.00	0.00	0.00	0.04
Mg	0.00	0.00	0.00	0.00	0.00	0.00	0.00	0.07	0.08	0.10	0.32
Ca	0.00	0.00	0.00	0.00	0.13	0.13	0.02	0.00	0.00	0.00	0.02
Na	0.08	0.04	0.03	0.02	0.83	0.83	0.95	0.06	0.01	0.04	0.02
K	0.92	0.96	0.97	0.98	0.02	0.01	0.00	0.93	0.85	0.94	0.77
sum	5.00	5.00	5.00	5.00	5.00	5.00	5.00	7.00	7.00	7.00	10.00
X Mg								0.40	0.74	0.43	0.15

Tab. 1 Representative mineral chemistry analyses of K-feldspar, plagioclase, white mica and chlorite obtained with electron microprobe and SEM.

III shear bands. The P-T section and compositional isopleths were calculated using the *Perple_X* thermodynamic software (Connolly, 2005), version 6.6.8, with the internally consistent thermodynamic data set of Holland and Powell (1998: version 2004). The preferred system for calculation was $\text{Na}_2\text{O} - \text{CaO} - \text{K}_2\text{O} - \text{FeO} - \text{MgO} - \text{Al}_2\text{O}_3 - \text{SiO}_2 - \text{H}_2\text{O}$ (NCKFMASH) with water in excess. The resulting P-T section has been calculated with following solution models: Ti-Fe-Mg-Mn biotite (extended from Powell and Holland, 1999), chlorite (extended from Holland et al., 1998), white mica (Coggon and Holland, 2002; Auzanneau et al., 2010), plagioclase (Newton et al., 1980) and garnet (Holland and Powell, 1998).

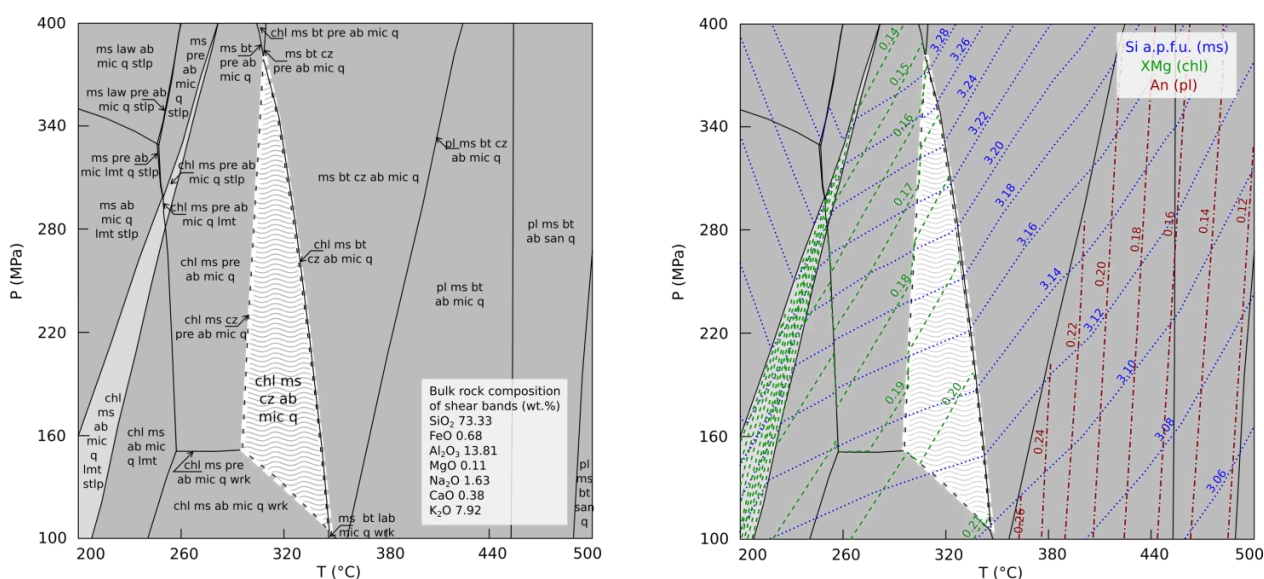


Fig. 6 P-T section calculated for shear band composition in sample SB4H by using thermodynamic software *Perplex* version 6.6.8 (Connolly, 2005) in the MnNCKFMASH system with water in excess. The compositional isopleths of XMg in chlorite, Si in white mica and anorthite component in plagioclase are shown in the image to the right. The stability field of observed shear band assemblage is highlighted by dashed white line and its range corresponds to the resulting P-T estimate.

In the resulting P-T section (Fig. 6, the observed shear band assemblage of white mica II, chlorite, albite and microcline best matches the stability field of white mica, chlorite, albite, microcline and clinozoisite. In the lower temperature parts of the P-T section, the Ca-bearing phase is represented by clinozoisite, which appears when oligoclase is replaced by albite (Fig. 6). In the studied rocks, however, clinozoisite was not observed. Instead the lower temperature Ca-bearing phase may be represented by apatite, which on the other hand is not present in the thermodynamic dataset and cannot be used in the modelling. For this reason the modelled assemblage of white mica-chlorite-albite-microcline-clinozoisite is considered as roughly corresponding to the observed assemblage. The stability of the white mica-chlorite-albite-microcline-clinozoisite field is limited by disappearance of chlorite towards higher

temperatures and by appearance of prehnite towards lower temperatures. The compositional range for chlorite and white mica II in the studied rocks fits well with the assumed stability field. However, because XMg in chlorite ranges between 0.15 – 0.21 and Si content in white mica II ranges between 3.08 – 3.29 apfu, the compositional isopleths cover full range of the assumed stability field and further restriction of P-T estimate was not possible. Thus the resulting P-T conditions for shear band assemblage correspond to the extent of the white mica-chlorite-albite-microcline-clinozoisite stability field i.e. to 300 – 350 °C and 100 – 400 MPa (Fig. 6). The plagioclase associated with the S fabric shows compositional range between 6 – 16 % of anorthite component, which in the calculated P-T section corresponds to temperatures higher than 445 °C (Fig. 6). This rough temperature estimate for the S fabric formation is in a good agreement with the relatively high temperature (~500-550 °C) (cf. Stipp et al., 2002), quartz deformation microstructure in the recrystallized aggregates related to S fabric (Fig. 2b-c).

4.4 Microstructure of shear bands

In the following text we describe microstructural relationships in the shear bands for each of the evolutionary stages I-III, documented from samples with increasing intensity of shear band overprint. The thin and separated bands in samples with low intensity of shear band overprint are characteristic for stage I, better represented by microstructure of filled microcracks (Fig. 7a). The stages II and III are associated with well developed shear bands characterized by microstructure in thicker and more interconnected bands (Fig. 7b-f).

The filled microcracks of stage I show individual small grains of albitic plagioclase, microcline, white mica II and/or chlorite decorating microcrack surfaces (Fig. 7a). Stage II show shear band widening associated with formation of microcline, and the bands are dominated by fine-grained mixture of microcline and quartz (Fig. 7b-c). The contact of the two phases is characterized by typical curved shaped or bulged grain boundaries suggesting that microcline is invading quartz (Fig. 8b). This observation is further supported by cathodoluminescence images where small quartz grains which are completely surrounded by the newly formed microcline still preserve cores with identical luminescence to the large quartz grains in the recrystallized aggregates (Fig. 8a).

Thus the original quartz microstructure of S fabric aggregates seems to be disintegrated by invading microcline which replaces quartz along shear bands and quartz grain boundaries (Figs. 7b-c, 8b).

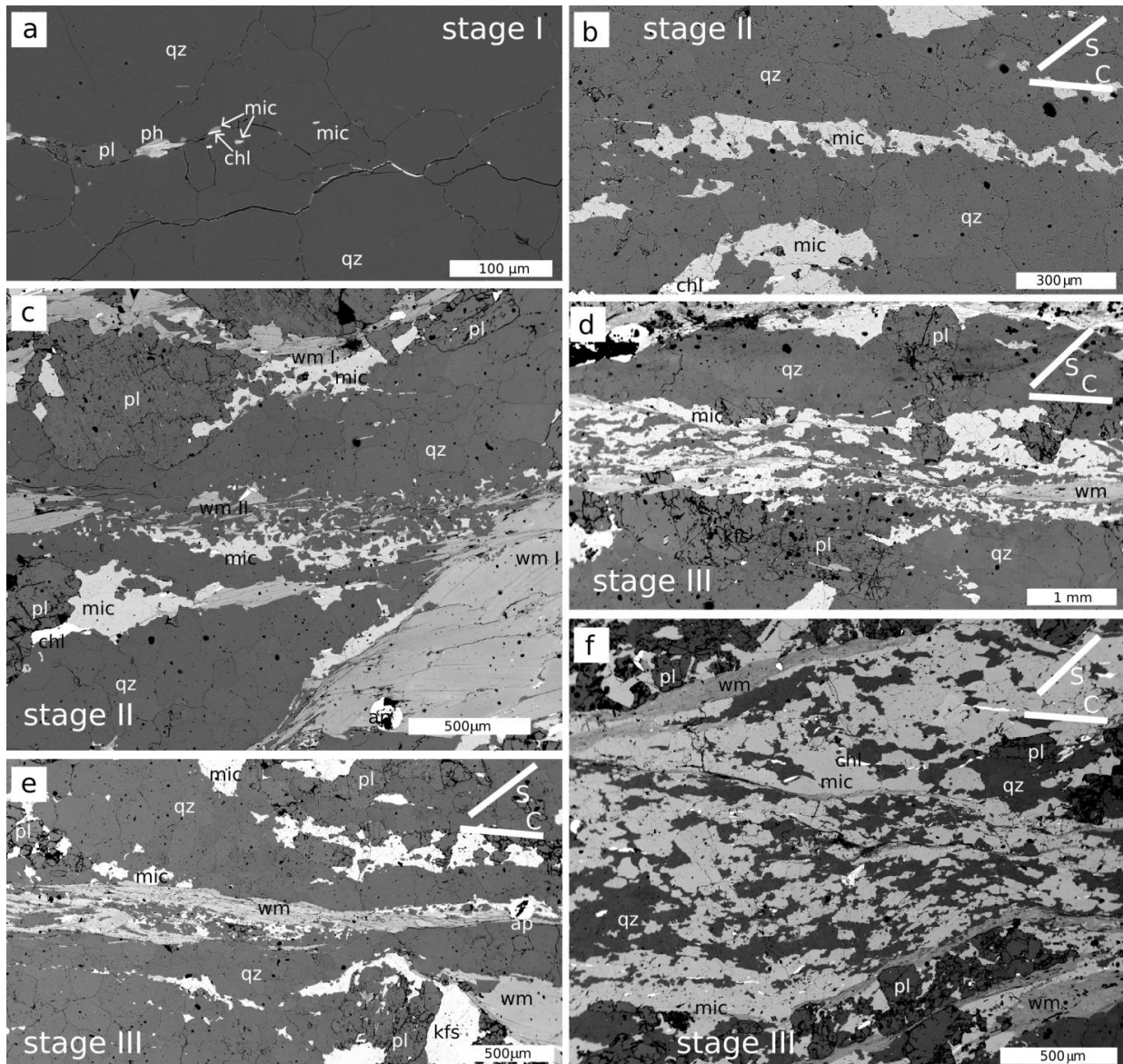


Fig. 7 BSE images showing characteristic microstructures for individual stages I-III of shear band development. The particular stages of shear band evolution and general orientation of C and S fabrics are indicated in each image. a) Microcrack crosscutting the quartz aggregate in stage I is filled with phengitic white mica II, microcline, plagioclase and chlorite (sample SB2A). b) Microcline replaces quartz along shear bands in stage II (sample SB4D). c) Quartz aggregate, plagioclase and white mica I porphyroclasts from the S fabric are reworked/replaced by shear band matrix composed of quartz white mica II and microcline in stage II (sample SB4D). d-f) White mica grains form interconnected bands crosscutting the earlier shear band microstructure composed of microcline – quartz in stage III (d, f - sample SB4H, e - sample SB4D). The white mica bands overprint thin e) as well as thick f) shear bands. Mineral abbreviations used: ap – apatite, chl - chlorite, mic - microcline, ph – phengite, pl - plagioclase, qz – quartz, wm – white mica.

Towards the stage III, white mica II starts to be frequent in the C-fabric matrix (Fig. 7c-d). The microstructure associated with stage III is characterized by bands of interconnected white mica that in a number of cases intersects and offsets quartz and microcline grains (Figs. 7d, e). The increasing proportion of white mica and the progressive interconnection in the direction

parallel to shear bands leads to the separation of domains, where mixtures of quartz and microcline represent the inactive relict microstructure related to stage II deformation. In the micaceous bands the white mica II shows features characteristic for dissolution of quartz and K-feldspar (Fig. 8d). The progress of shear band widening and interconnection (Fig. 7f) may eventually lead to formation of ultramylonites characterized by significant decrease in grain size and complete phase mixture.

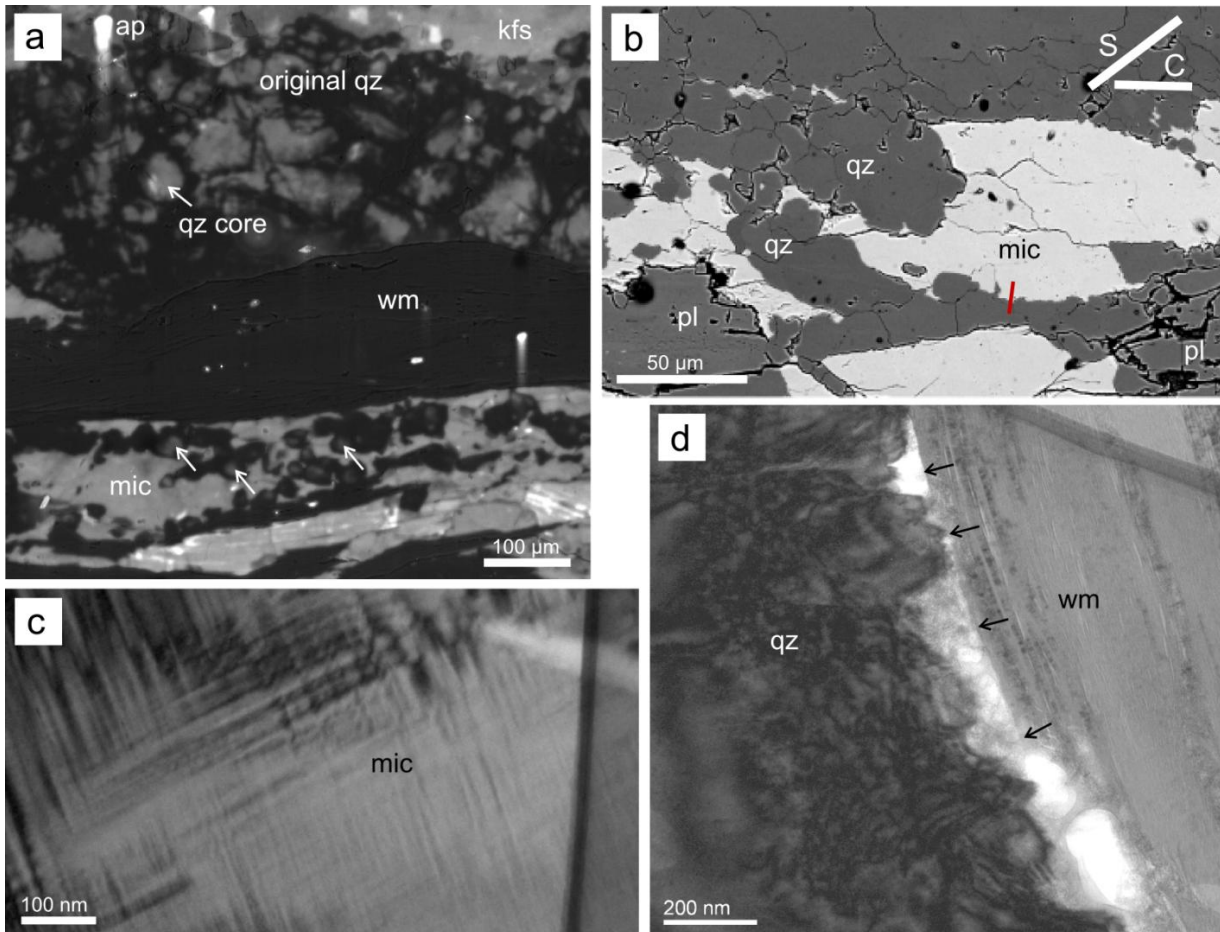


Fig. 8 a) Cathodoluminescence image from the boundary between shear band (lower part) and quartz aggregate (upper part) in sample SB4H. The upper part of the image shows disintegration of the quartz aggregate microstructure while the lower part of the image shows individual quartz grains enclosed by microcline inside the shear band. The cores of these individual grains exhibit identical luminescence as the original quartz grains in aggregates. b) BSE image of microcline – quartz microstructure in stage II showing locations of TEM foil (red line). c) The microcline twinning within the precipitated microcline in stage II shear bands. d) The interface of white mica and quartz, where white mica precipitation causes dissolution of quartz and formation of porosity (white – filled with epoxy in the sample).

4.5 Quantitative microstructural analysis of shear bands

The microstructures of mixed quartz and microcline related to the three stages of shear band evolution (Fig. 9a) have been evaluated from digitized BSE and optical micrographs at localities SB2 and SB4 (Fig. 1) by comparing grain parameters such as size, shape preferred

orientation and contact frequency. The grain diameter is specified as diameter of a circle with the grain equivalent area and it was determined for both quartz and microcline (Fig. 9b). The median grain size (and inter-quartile range IQR) of microcline steadily increases from 7 μm (IQR = 5-12 μm) for stage I, to 18 μm (IQR = 12-28 μm) for stage II and 17 μm (IQR = 8-25 μm) in the stage III (Fig. 8 b). In contrast, the median grain size of quartz decreases from 46 μm (IQR = 23-85 μm) for stage I, to 45 μm (IQR = 19-103 μm) for stage II, to 19 μm (IQR = 11-23 μm) for stage III manifesting the continual reduction of grains associated with the S fabric. The length weighted orientations of grain boundaries presented in rose diagrams (Fig. 9c) have been evaluated separately for alike and unlike phase contacts, i.e. for quartz – quartz, microcline – microcline and quartz – microcline contacts (Fig. 9c). From stage I to stage III, the rose diagrams clearly demonstrate the change in shape of microcline grains from equiaxed to elongated, with long axes parallel to shear bands while quartz grains generally maintain the equiaxed shape. The quartz – microcline phase contacts in all three stages show preferred orientation parallel to shear bands (Fig. 9c). The grain contact frequency for alike and unlike phase contacts was evaluated using the grain contact frequency method of Kretz (1969, 1994). In his method, the grain contact frequency number (χ) expresses a deviation from random distribution of phases. For alike phase contacts χ is positive for aggregate, zero for random and negative for regular distributions, and this relationship is reversed for unlike phase contacts. The results of grain contact frequency analysis of quartz – quartz, microcline – microcline and quartz – microcline contacts show identical trends in evolution from stage I to stage III (Fig. 9d). The transition from stage I to stage II indicates randomization of the inherited aggregate distribution of phases (Fig. 9d). In contrast, the transition from stage II to stage III show reversed trend and the evolution from more random towards more aggregate distribution of quartz and feldspar. At the same time the grain boundary preferred orientation of microcline becomes stronger while the one of quartz weakens. The intersecting crystallization relationships of white mica II with respect to quartz and microcline in the late period of stage III suggests that the growth of mica post-dated the above-described mixing/unmixing of quartz and microcline phases.

The crystallographic preferred orientation (CPO) of quartz aggregates show single maxima and single girdle patterns (Fig. 10a). In the [0001] c-axis diagrams, the CPO maxima are located at the periphery of the pole figures at 60-70° angle from the S fabric (Fig. 10a). These maxima suggest activity of basal $\langle a \rangle$ slip system. At the same time, weak single girdles of c-axis occur close to the orientation of S fabric with maxima in the vicinity of its lineation

suggesting activation of prism [c] slip (Fig. 10a). Indeed, if the tilt boundaries are assumed the axes of low angle misorientations plotted into the inverse pole figure (Fig. 10b) suggest dominant basal <a> or prism [c] and some contribution of rhomb <a> slip systems. As the misorientation analysis cannot distinguish between basal <a> or prism [c] (Lloyd, 2004), the universal stage was applied to confirm or disprove the two slip systems by measuring the angle between the orientation of subgrain boundaries and c-axes of subgrains (e.g. Okudaira et al., 1995). At least twenty pairs of subgrain boundary - subgrain c-axis from each of the three samples at locality SB4 (Fig. 1) were analyzed (Fig. 10 c) indicating that the c-axes are mostly subparallel to subgrain boundaries. This confirmed the prevalence of the basal <a> slip and excluded the operation of prism [c] slip (cf. Okudaira et al., 1995).

It is interesting to note that the single maxima related to basal <a> slip show both synthetic and antithetic rotations with respect to overall shear sense indicated by the S-C fabrics geometry (Fig. 10a). The presence of weak subordinate c-axis girdle in most analyzed samples remains unclear as it may either correspond to weak contribution of prism [c] slip during the formation of S fabric or it may be related to the subsequent overprint associated with formation of shear bands.

4.5.1 Crystallographic preferred orientation in shear bands

The CPO of quartz in the vicinity of shear bands documents modification/overprint of the aggregate CPO in the S fabric. In the early stages of shear band formation (stage I) associated with microcracking the overprint is insignificant and the aggregates still preserve the original CPO (aggregate grains in light blue; Fig. 11a). This changes towards stage II when the microcracks become active slip surfaces and impose recrystallization of coarse-grained quartz microstructure in the vicinity of microcracks (recrystallized grains in red; Fig. 11b). The misorientation angle profile AA' in figure 11b shows the presence of subgrains inside the quartz aggregate grains and demonstrates continuous rotation of the lattice of smaller recrystallized grains away from the orientation of parent grains. These observations point to the rotation recrystallization mechanism that is active during the slip along the shear bands. The misorientation axis between parent and recrystallized grains occurs in the shear band plane and is perpendicular to the shear band lineation (star in the centre of pole figures in Fig. 11) indicating the formation of tilt boundaries and activity of basal <a> slip system (e.g. Neumann, 2000). In addition, the clockwise rotation of lattice of the recrystallized grains away from the orientation of aggregate grains (black arrows in Fig. 11) is consistent with the

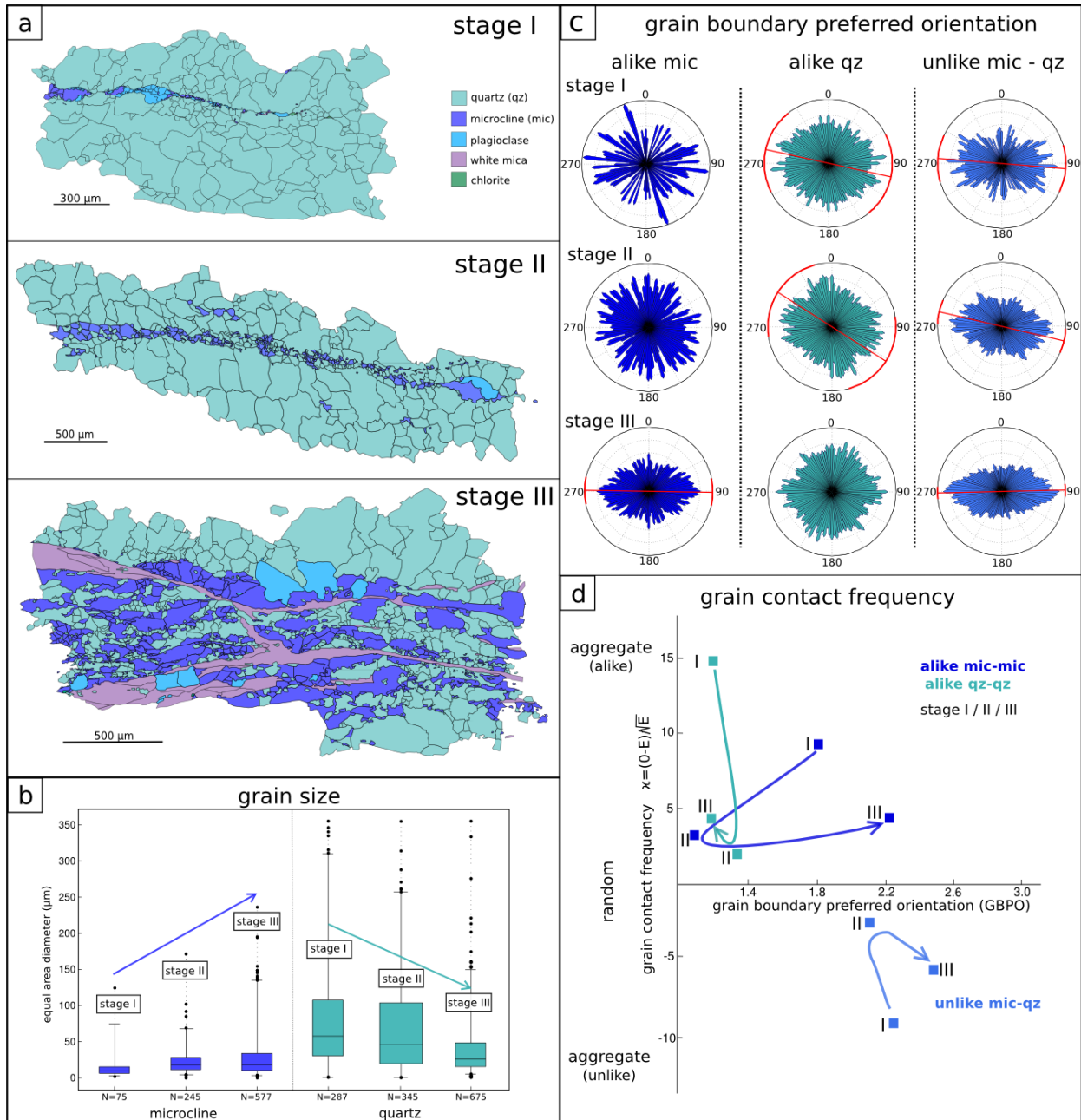


Fig. 9 Results of quantitative microstructural analysis from a) digitized microstructures related to stage I (sample SB2A), stage II (sample SB4D) and stage III (sample SB4H) of shear band evolution. b) The boxplots for microcline and quartz grain size from individual stages I-III demonstrate an increase in size of microcline grains and decrease of quartz grains from stage I to III. N - number of analyzed grains. c) Weighted rose diagrams show grain boundary preferred orientation obtained from the digitized grain maps of microcline alike boundaries, quartz alike boundaries and microcline – quartz unlike boundaries for individual stages I-III. The red line in diagrams shows mean orientation and the red sections along the periphery of the diagrams show the orientation within standard deviation (1σ). d) The results of grain contact frequency analysis (Kretz, 1969) of alike and unlike boundaries for microcline and quartz for individual stages I-III plotted against grain boundary preferred orientation. All analyzed contacts show similar trends i.e. from aggregate distribution in stage I via randomization in stage II to more aggregate distribution in stage III.

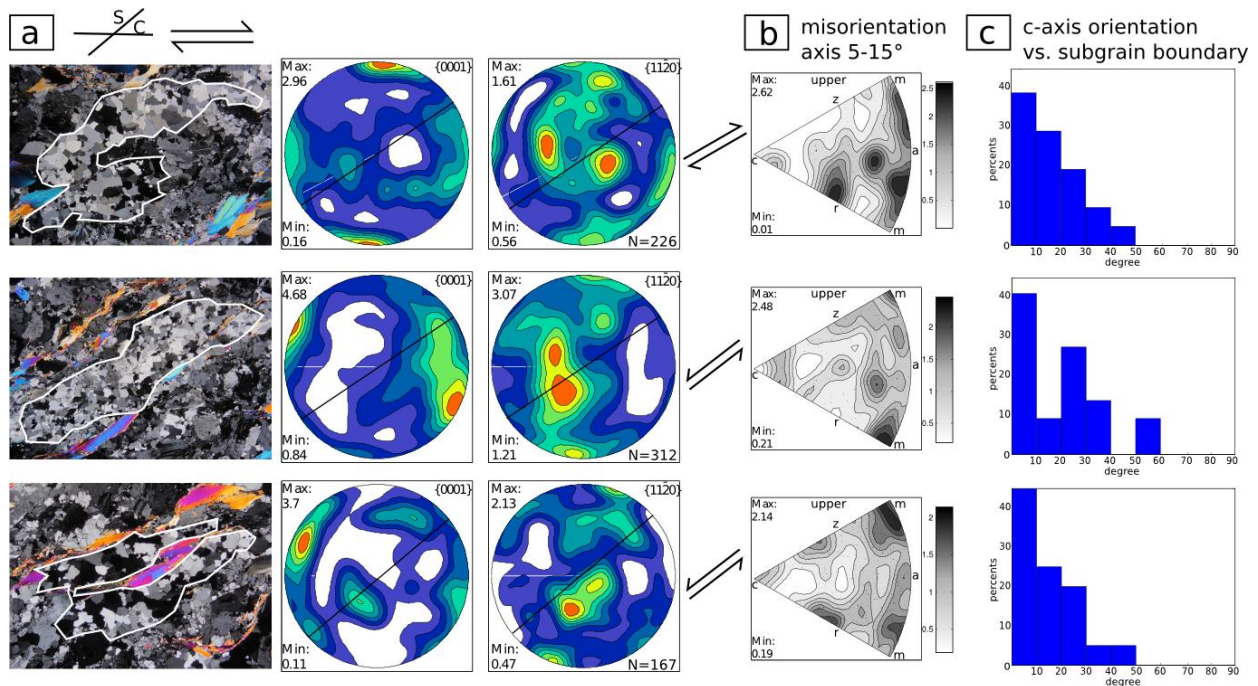


Fig. 10 Results of crystal preferred orientation (CPO) analysis of quartz aggregates defining the S fabric. a) Microphotographs of quartz aggregates used for EBSD mapping and corresponding pole figures of quartz CPO's. The orientation of C and S fabrics is indicated in the microphotographs and orientation of S fabric is indicated by solid black line in each pole figure. The overall kinematic frame can be compared with the shear sense determined from the S fabric aggregates for each sample by using the criterion of inclination of CPO with respect to orientation of the S fabric. b) Inverse pole figures show position of misorientation axes with respect to the crystal reference frame for the 5-15° misorientation interval. c) The histograms showing angular relationship between C-axis of subgrains and trace of subgrain boundaries determined by U-stage from quartz aggregates defining the S fabric in corresponding samples in a). The histograms show prevailing low angle relationships suggesting operation of basal $\langle a \rangle$ slip system.

dextral shearing along shear bands and thus documents the relationship between recrystallization and slip along the microcracks.

The stage II of shear band development is marked by the formation of microcline disintegrating the recrystallized quartz microstructure along shear bands. This process leads to separation/isolation of parts of recrystallized quartz microstructure being surrounded by the newly formed microcline (recrystallized grains attached to aggregates in green and recrystallized grains enclosed by microcline in dark blue; Fig. 11c). At the same time, slip along shear bands and quartz recrystallization continued as documented 1) by the presence of recrystallized quartz grains along the contacts between aggregates and shear bands and 2) by randomization of quartz CPO shown by isolated quartz grains within shear bands (Fig. 11c, d). The CPO of microcline is very weak to absent (Fig. 11c, d).

The grain size of recrystallized quartz grains along the contact between an aggregate and shear band (red grains in Fig. 11) increases with increasing width of shear bands from stage I to stage III (Fig. 11e). The stage III of shear band development is associated with formation of interconnected white mica bands. The white mica show strong CPO with their basal planes oriented sub-parallel to shear bands (Fig. 11d).

On next page:

Fig. 11. Crystallographic preferred orientation of main phases for individual stages I-III of shear band evolution. a) Stage I (sample SB2A) shows quartz aggregate (light blue) crosscut by microcrack filled with microcline, white mica and chlorite (shown in grey). The corresponding pole figures show CPO of quartz aggregate related to formation of S fabric and CPO of microcline grains in the microcrack. b) Stage I (sample SB4E) showing recrystallization of quartz aggregate along microcrack (black). The quartz grain map shows parent (light blue) and recrystallized (red) grains along the microcrack. Identical color-coding has been used in the pole figures. The recrystallized grains with respect to the parent grains show clockwise rotation around misorientation axis indicated by yellow star in the pole figure. The misorientation profile AA' marked in the grain map shows evolution in misorientation angle from parent grain towards fracture (blue line) as well as relative misorientation angle between individual grains (red line). c) Stage II sample SB4D) show portions of recrystallized quartz grains encircled by microcline within the shear band (dark blue quartz, grey microcline), quartz grains within the shear band maintaining the contact with aggregate (green) and recrystallized quartz grains (red) along the contact between shear band and quartz aggregate (light blue). The corresponding CPO's of these distinct quartz grains are shown in pole figures using identical color-coding. The misorientation axis between parent and recrystallized grains is indicated by yellow star. The pole figures for microcline show weak CPO. d) Stage III (sample SB4H, corresponds to Fig. 9a and part of Fig. 6d) show grain maps and pole figures with identical color-coding as in c). The misorientation axis between parent (light blue) and recrystallized (red) quartz grains is again indicated by yellow star. The CPO of quartz grains (green and blue) encircled by microcline show scattering of orientations away from the orientations of recrystallized grains (red) along the contact between shear band and quartz aggregate. K-feldspar in the shear band is characterized by random CPO, while white mica reveals strong CPO with basal planes being mostly parallel to the shear band. The pole figures represent projection on upper hemisphere. e) Grain size (equal area diameter) increase from stage I to stage III of quartz grains at the contact with aggregate (grains shown in red in b – d) with the mean size given aside the boxplots.

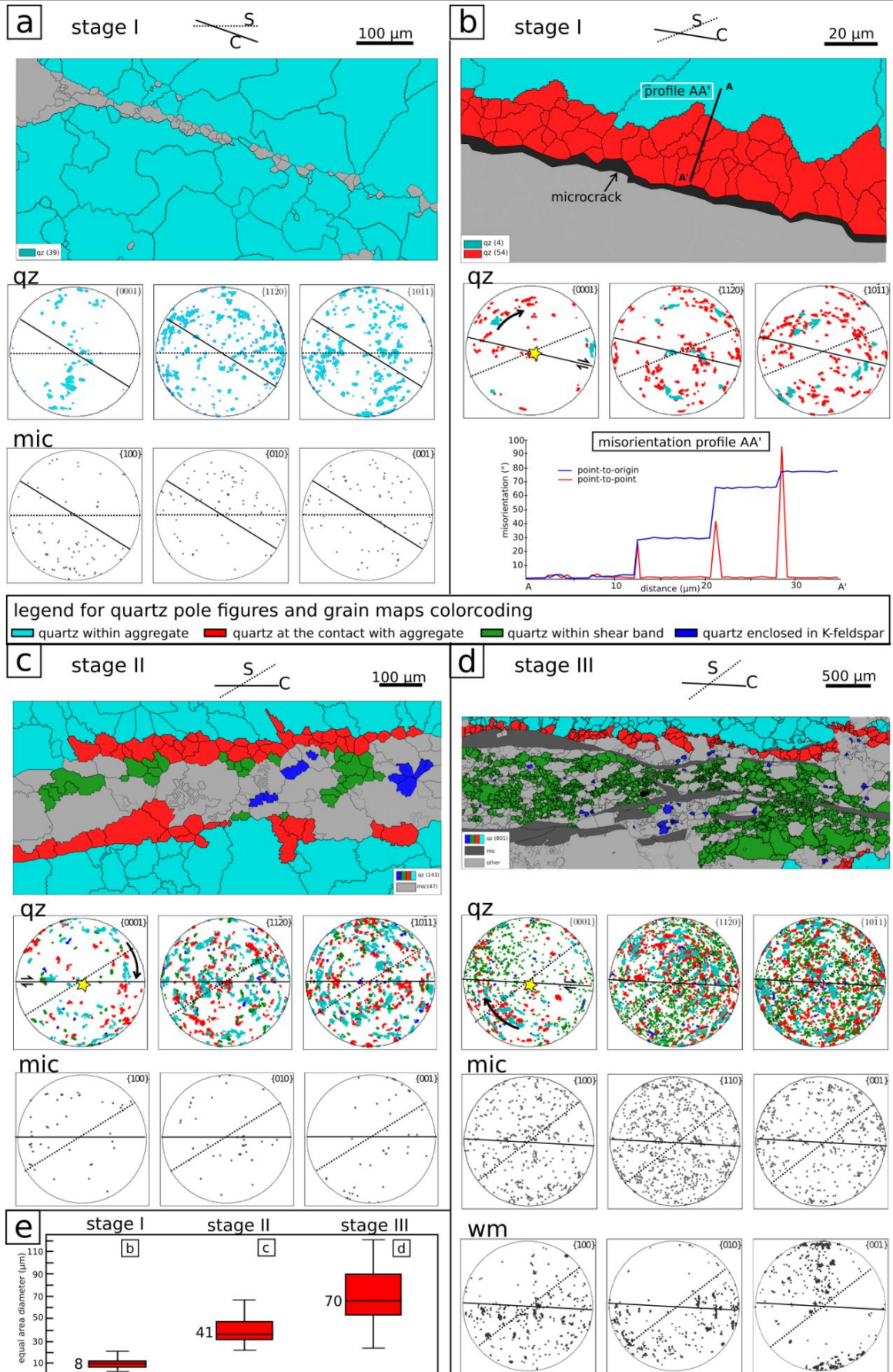


Fig. 11 For description see previous page.

5 Discussion

5.1 S-C fabrics in the South Armorican Shear Zone: their origin and geometry

The origin and mechanical importance of S-C fabrics has been discussed for decades since their first recognition in the South Armorican Shear Zone by Berthé et al. (1979 a, b). Two principal scenarios explaining the formation of S and C fabrics as synchronous or diachronous are commonly assumed (e.g. Lister and Snoke, 1984). The synchronous S-C/C' fabrics are usually reported from major crustal shear zones where their evolution is associated with partitioning of deformation or variation in the intensity of shear strain (Berthé et al., 1979 a; Platt, 1984; Blenkinsop and Treloar, 1995; Schulmann et al., 1996; Füsseis and Handy, 2008). The diachronous S-C fabrics are explained either as sequential overprint of metamorphic foliation (S) by narrow shear bands (C/C') formed during single kinematic event due to cooling and localization (e.g. White et al., 1980; Gapais and White, 1982; Knipe and Wintsch, 1985; Gapais, 1989; Gillam et al., 2014) or as cleavage overprinting an earlier and kinematically unrelated metamorphic foliation (e.g. Platt and Vissers, 1980; Bukovská et al., 2013).

The studied S-C fabrics in the major right-lateral South Armorican Shear Zone develop in granitoid plutons that were emplaced synkinematically relative to SASZ between 338-329 Ma and affected by shearing as late as 300 Ma (Tartèse et al., 2011; 2012). These S-C fabrics were previously interpreted as synchronous (Berthé et al., 1979 a, b) or diachronous and resulting from single kinematic event as a result of cooling of granitoids (Lister and Snoke, 1984; Gapais, 1989). The diachronous origin of the two fabrics is also suggested by our data indicating distinct metamorphic grade associated with the S and C fabrics, respectively. The S fabric is defined by shape preferred orientation of magmatic minerals such as large grains of white mica I and porphyroclasts of K-feldspar I and plagioclase (with unknown composition due to subsequent replacement by mixture of albite and white mica) which in the same fabric are overgrown/replaced by the newly formed plagioclase with anorthite component between 6 and 16 mol% (Fig. 5). Furthermore, the S fabric is defined by shape preferred orientation of recrystallized quartz aggregates dominated by grain boundary migration microstructure (Figs. 2, 10) that is typical for high temperature deformation >550 °C (Stipp et al., 2002). Because of these relatively high temperatures and overprinting relations, the S fabric can be interpreted as magmatic-subsolidus formed during emplacement/cooling of the SASZ granitoids. In

contrast, the C fabric is associated with albite-muscovite-chlorite-microcline assemblage with estimated P-T conditions of 100-400 MPa and 300-350 °C (Fig. 6). These temperatures are in a good agreement with subgrain rotation recrystallization of quartz, which is observed in association with slip along the shear bands (Figs. 2, 11). The above temperature estimates comply with synkinematic cooling of the SASZ plutons from >550 °C, marked by the S fabric, to 350 °C, marked by the C fabric. However, the absence of transitional microstructures between the two end member fabrics (S and C) implies two distinct periods of deformation.

In addition, the texture analysis of recrystallized quartz from both S and C fabrics also point to two distinct periods of deformation as they document kinematic criteria that are clearly dextral for shear bands but ambiguous for the S fabric. The basal <a> dominated asymmetric quartz CPO's (Fig. 10) obtained from the S fabric show both sinistral and dextral kinematics (cf. Lister and Williams, 1979; Simpson and Schmid, 1983). Thus although the asymmetry of quartz CPO is often used for kinematic interpretations (e.g. Law et al., 1990), the results have to be considered with caution due to the effects of pure shear component (e.g. Jeřábek et al., 2007) or heterogeneous distribution of strain and strain partitioning in the simple shear dominated deformation zones (Krohe, 1990; Kilian et al., 2011). Similarly our results of quartz texture analysis suggest a complex evolution of the S fabric in comparison with relatively simple kinematics related to the C fabric.

5.1.1 Initiation of shear bands

Our P-T estimates for the C fabric show relatively low temperatures (300-350 °C) and pressures (100-400 MPa) characteristic for the conditions of brittle-plastic mechanical transition in crustal rocks (e.g. Peč et al., 2012). Indeed, the studied rocks show intra-granular microcracks identified in the quartz aggregates so that they cross-cut the S fabric in an orientation close to the C bands (Fig. 4). Moreover, the microcracks sub-parallel to C fabric are filled by minerals typical for shear bands and therefore they are interpreted as shear band precursors (Fig. 4c, 7a). Microcracks have become frequently recognized as precursors of ductile shear zones affecting mid-crustal granitoids (e.g. Pennacchioni and Mancktelow, 2007; Fousseis and Handy, 2008; Mancktelow and Pennacchioni, 2013), but also lower crustal rocks (Menegon et al., 2013; Okudaira et al., 2015). The microcracking is typically explained by stress concentrations where the effective viscosity contrasts between weak and strong phases are high, e.g. at the tips of phyllosilicates (Holyoke and Tullis 2006) or in material with the same composition but very different grain size (Rybacki et al., 2014). Similarly, the

observed microcracks from SASZ are often associated with large white mica I grains elongated parallel to S and occurring within or in the vicinity of quartz aggregates (Fig. 4a). The analysis of microcrack orientations show their dominant occurrence at an angle of 36° with respect to S followed by two subordinate peaks at 19° and 42° (Fig. 4b). Microcracks with these orientations commonly show the C fabric matrix mineral infill (Figs. 4c, 7a) while microcracks of other orientations are usually infill-free. The relationship between orientation and infill suggest that the microcracks oriented at dihedral angles higher than 15° from S are suitably oriented for mineral precipitation and thus indicate an opening of microcracks formed at $36 \pm 15^\circ$ with respect to S (Fig. 4b). Similar microcracks have been reported from deformation experiments of quartz aggregates (Hirth and Tullis, 1994) where the observed mode II cracks concentrated at $\pm 15^\circ$ with respect to main axial stress. Assuming that the observed microcracks in SASZ formed by similar mechanism, local orientation of main principal stress in the moment of cracking should be subparallel to the orientation of shear bands. On the other hand, in order to maintain the observed right-lateral shear displacement along the shear bands the main principal stress vector should be at least slightly clockwise rotated with respect to shear bands, i.e. NNW–SSE trending in geographic coordinates (Fig. 12a). Assuming that the stress concentration and cracking are related to dislocation glide along the (001) plane of large white mica grains in S the highest Schmid factor of 0.5 corresponds to orientation of main principal stress at 45° with respect to S. Such slip would allow cracking at the tips of white mica (see e.g. Misra, 2011) and also satisfies the observed dextral shear sense along shear bands (Fig. 12a). The opening microcracks and associated precipitation/crystallization of minerals lubricating the crack plane lead to the switch into viscous shearing along the microcracks. Thus although the microcracking is initially an important mechanism for localization of deformation its importance later decreases, with the deformation being accommodated by slip along thin shear bands (Fusseis and Handy, 2008).

5.1.2 Geometry of S-C fabrics

It is interesting to note the changes in dihedral angle between the S and C fabrics towards higher degree of shear band overprint manifested mainly by the increasing proportion of shear band matrix at the expense of porphyroclasts in S (Fig. 3). As summarized in Fig. 12b, the average dihedral angle between S and C fabrics increases from 35° when the C bands are thin and isolated to 42° when the C bands increase their width and become interconnected. On the other hand, with further increase of shear band matrix proportion $>13\%$ the dihedral angle starts to decrease and both fabrics become parallel/indistinguishable in the ultramytonite

samples. The low dihedral angles for thin and isolated shear bands are in a good agreement with the most frequent orientation of microcracks indicating dihedral angles of 36° . This suggests that the initial orientation of shear bands is associated with relatively constant orientation of C with respect to S at $\sim 35^\circ$. Similar initial dihedral angles have been previously reported by Agard et al. (2011) from Betic Cordilleras and Gillam et al. (2014) from New Zealand. The subsequent increase in dihedral angle is contrary to commonly observed decrease of the angle with increasing displacement along shear bands (e.g. Berthé et al., 1979 a; Agard et al., 2011) and provides room for several alternatives: 1) antithetic rotation of S due to highly localized slip along interconnected white mica bands at stage III (Gapais et al., 1991), 2) rotation of the sub-stable S-C fabric geometry towards orientation of main principal stress so that the S fabric starts to buckle (Michibayashi and Murakami, 2007), or 3) formation of C' shear bands at low angles with respect to C shear bands and spatial overlap of both types (Blenkinsop and Treloar, 1995). The latter option is further supported by the increased scatter in the C fabric orientation (Fig. 3d).

5.2 Mechanisms related to formation and evolution of shear bands

Formation of shear bands at conditions of green schist to lower amphibolite facies is commonly associated with both brittle and crystal-plastic processes (e.g. Passchier, 1984). In the original study of Berthé et al. (1979 a,b) from the South Armorican Shear Zone the formation of mylonites in the S fabric is associated with recrystallization of feldspars and quartz while the formation of shear bands (the C fabric) is associated with cataclasis and comminution of quartz, feldspars and micas porphyroclasts. In their concept the concomitant development of both fabrics at $\sim 450^\circ\text{C}$ was interpreted as a consequence of progressive variation in the intensity of shear strain. In contrast, Gapais and White (1982) interpreted the formation of shear bands in association with dynamic recrystallization of quartz followed by softening associated with grain boundary sliding within the shear bands. These authors argued that the localization of deformation into shear bands occurs when the temperature decreases below the biotite isograd. Similarly also in this work, the formation of shear bands is associated with relatively low temperatures $300\text{-}350^\circ\text{C}$ (Fig. 6). On the other hand it is important to state that the below-described evolution of shear bands is not related to temperature or pressure changes because 1) no major differences in assemblage or composition of shear band matrix minerals was detected amongst individual evolutionary stages and 2) the strike-slip character of SASZ prevents major changes in depth/pressure. The latter is supported by the similarity of our estimated pressures (100-400 MPa) for shear band

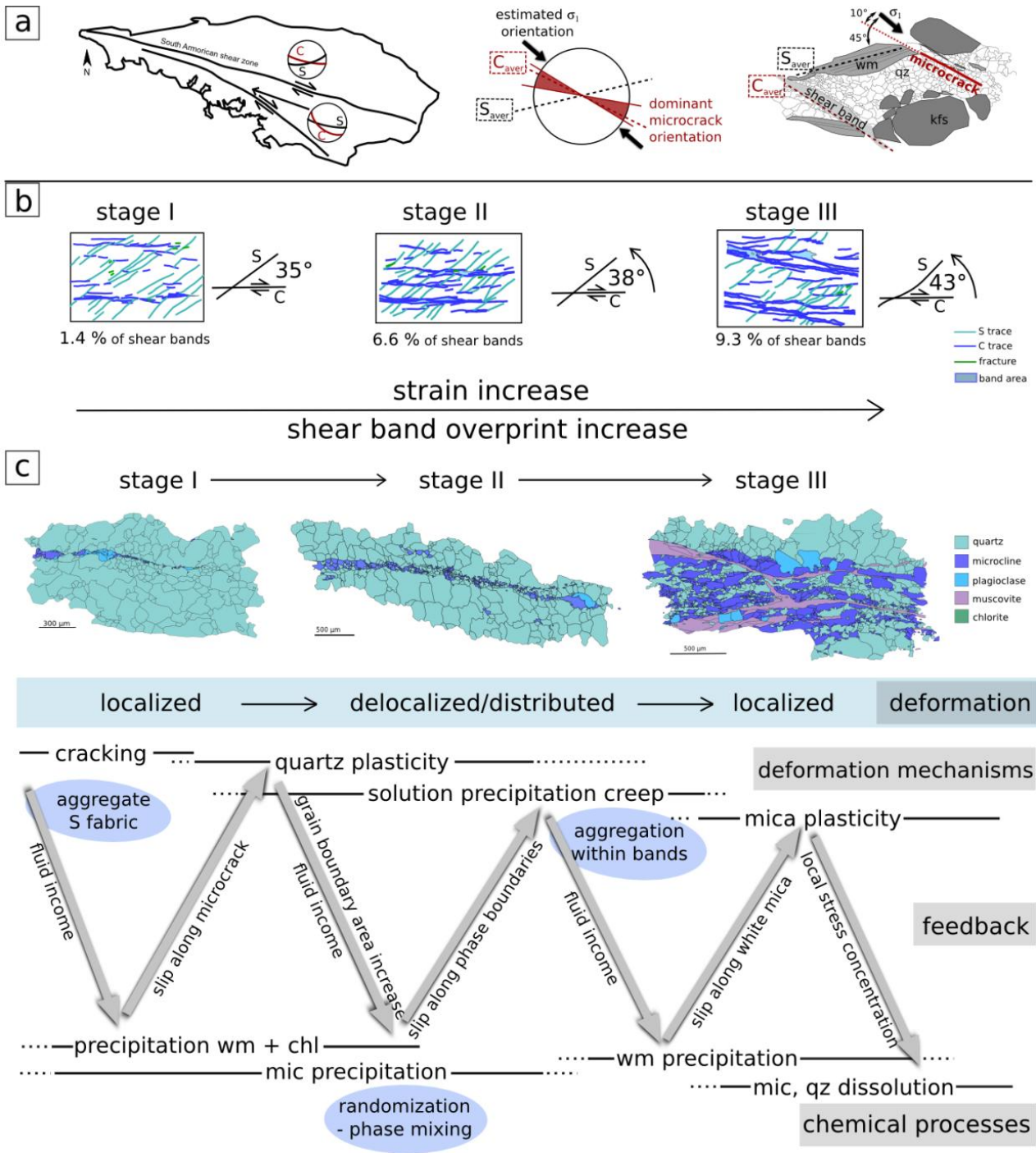


Fig. 12 Overview on shear band evolution. a) Orientation of S and C fabrics on regional scale on two main branches of South Armorian Shear Zone and on microscale. The corresponding orientation of average S and C fabrics from geometry analyses (Fig. 3) with dominant microcrack orientation and estimated orientation of maximum compressional stress (σ_1). Microcracks are assumed to be oriented at ca. 10° to σ_1 , while S fabric at 45°. b) Evolution of the S-C fabric geometry with increasing strain and shear band overprint on the scale of thin section. The respective angle of S-C fabric increases up to some 13% of the rock is reworked by shear bands. c) Microstructural overview on shear band evolution. The changed in three stage evolution is shown with respect to the deformation (de)localization, deformation mechanisms acting in distinct stages as well as chemical processes and the feedback.

assemblage in sample SB4 from the Questembert granite and its synkinematic emplacement to pressures of 100-200 MPa (Tartèse and Boulvais, 2010).

The evolution of shear bands in the SASZ was divided into three stages based on microstructural differences reflecting activation of different deformation mechanisms while the switches between individual deformation mechanisms were controlled by the interplay and positive feedback between

deformation and fluid-controlled chemical processes (Fig. 12c). As discussed above the initiation stage I evolution of shear bands is associated with brittle deformation manifested by the presence of microcracks sub-parallel to later shear bands (Fig. 12c, stage I). The microcracks opened pathways for fluids bringing in the elements to precipitate white mica, chlorite, microcline and albite along the microcracks (Fig. 7a). These newly precipitated phases acted as a lubricant facilitating the highly localized deformation and slip along the microcracks. Towards the stage II, slip along microcracks induced crystal plasticity in the neighbouring large quartz grains associated with the S fabric. Here the dislocation glide and activity of basal $\langle a \rangle$ slip system led to formation of subgrains and recrystallized grains with considerably smaller grain size compared to the S fabric microstructure (Fig. 11b). The lattice clockwise rotation of recrystallized quartz grains away from the orientation of parent grains is consistent with dextral sense of shearing along the shear bands (Fig. 11b). Dynamic recrystallization of quartz and associated increase in the density of grain boundaries facilitated an income of fluids and precipitation of microcline, whose appearance is characteristic for stage II of shear band evolution (Fig. 12c, stage II). The precipitating microcline along the recrystallized quartz grain boundaries resulted in randomization of originally aggregate distribution of phases (Fig. 9d), complete isolation of some quartz grains inside the shear bands (Fig. 8a, b), and decrease in quartz grain size inside the shear bands (Fig. 9b). Similar mechanism of phase mixing and reduction of quartz grain size by dissolution-replacement has been previously described from ultramylonitic shear zones in the Gran Paradiso by Kilian et al. (2011).

The continuing slip along shear bands at stage II is demonstrated by the loss and randomization of the originally host controlled CPO of the recrystallized quartz grains isolated within the microcline dominated matrix inside the shear bands (Fig. 11c, d). At the same time, dynamic recrystallization of quartz at the boundaries between shear bands and quartz aggregates is still active and the above-described positive feedback between quartz recrystallization, fluid infiltration and microcline precipitation leads to progressive widening

of the shear bands. Thus distributed/delocalized deformation is characteristic for stage II. The observed replacement and precipitation inside the shear bands together with the lack of CPO and absence of dislocations in microcline (Figs. 8c and 11d) suggest that the deformation at stage II is accommodated by dissolution-precipitation creep and some contribution of grain boundary sliding (Wintsch and Yi, 2002; Menegon et al., 2008; Fukuda et al., 2012). The contribution of grain boundary sliding and associated cavitation (Čadek, 1988) allowed for income of fluids and precipitation of isolated white mica grains in dilatant sites (Fig. 7c). As no substantial increase in white mica proportion was observed, it is likely that the newly formed white mica II reprecipitated/recrystallized from large grains of white mica I (see Fig. 7c). At the same time, the grain boundary sliding along phase boundaries may have led to rearrangement of grains towards more aggregate phase distribution (Hiraga et al., 2013) observed at the late stage II of shear band evolution (Fig. 9d).

Towards stage III, the isolated white mica grains with suitable orientation sub-parallel to shear bands started to interconnect partly as a result of crystal plasticity and the activation of the easy glide system along (001) planes. As the proportion of white mica in the studied samples remains near-constant, the reaction softening mechanism due to metamorphic transformation of K-feldspar to white mica (Wintsch et al., 1995; Wintsch and Yeh, 2013) does not seem to be the key mechanism for the observed transition from stage II to stage III of shear band evolution. In contrast, it is the dispersion of reprecipitated white mica along the microcline-quartz boundaries together with its plasticity that could lead to their interconnection and thus accommodate the stage II to stage III switch (cf. Fig. 7c and e). The interconnected white mica bands, typical for stage III (Fig. 12c, stage III), cross-cut and offset the previous "frozen" microstructure of mixed quartz and microcline of stage II (Fig. 7e) suggesting that the entire deformation within shear bands at stage III is accommodated by dislocation creep of white mica (Fig. 11d). At the same time, this stage is characterized by highly localized deformation along white mica bands. Consequently, the slip along these bands leads to local stress concentrations along restraining bends inducing pressure solution of quartz and microcline occurring at the interfaces with white mica (Fig. 8d); see Bukovská et al. (in press).

5.3 Rheological implications

The above-described four principal deformation mechanisms that are sequentially activated in the studied shear bands (Fig. 12c) allowed us to evaluate rheology of these microscale shear zones and their strength contrast with respect to shear zone walls at individual stages of

shear band evolution. For this purpose we applied experimentally derived flow laws (Tab. 2) for dislocation creep in quartz (Paterson and Luan, 1990) and micas (Kronenberg et al., 1990; Mares and Kronenberg, 1993; Mariani et al., 2006). The temperatures and pressures used in rheological predictions were taken as average values from our P-T estimates, i.e. 250 MPa and 325°C (Fig. 6). For the period of shear band evolution, these values are considered as near-constant because of identical assemblage that was documented in all evolutionary stages (constant temperature) and strike slip character of the SASZ (constant pressure). The differential stresses and strain rates calculated from the well defined piezometric and creep relations for quartz were used to shed some light on the relatively unknown mechanical behaviour of dissolution-precipitation creep in microcline and on the less well constrained behaviour of white mica. This goal was achieved by combining the mechanical data with observed changes in width of shear bands at individual stages (Fig. 13a) under the assumption of at least temporarily constant displacement rate along the SASZ.

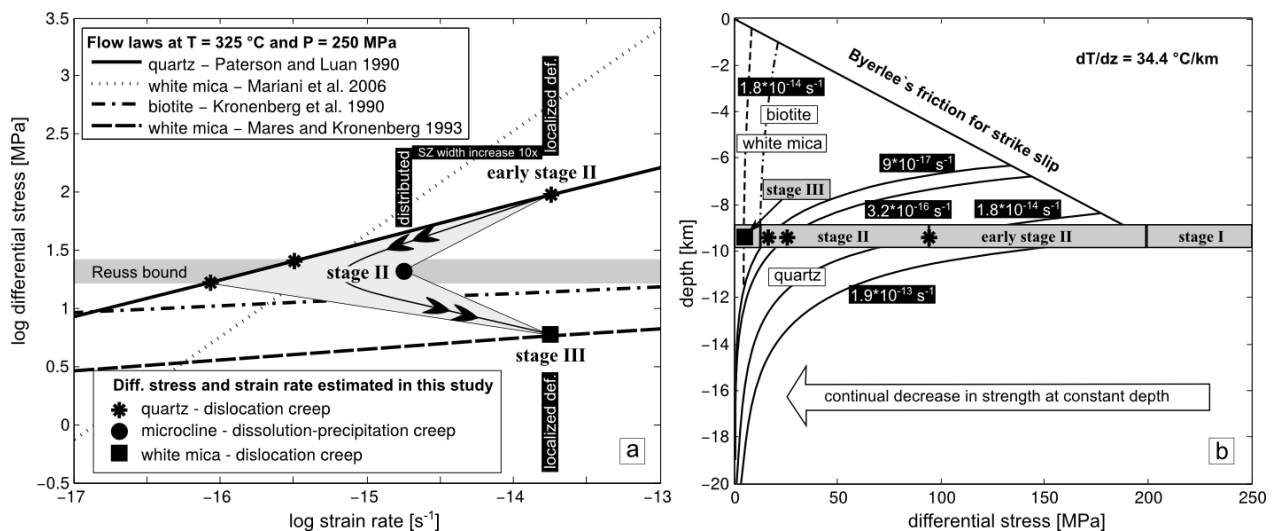


Fig. 13 Rheological implications for brittle-plastic transition: a) Changes in differential stress and strain rate during the evolution of shear bands revealed by the observed deformation microstructures and experimentally derived flow laws (Tab. 2). b) Evolution of strength of the brittle-plastic transition recorded in the South Armorican Shear Zone during formation of shear bands. The strength curves are based on Byerlee's frictional envelope for strike-slip faults ($\mu = 0.85$, hydrostatic pore pressure, $\sigma_2 =$ mean stress) and on dislocation creep envelope derived from flow laws used in b).

The identified sequence of deformation mechanisms from stage I to stage III of shear band evolution indicate transition from brittle to plastic behaviour and continual decrease in strength of the SASZ (Fig. 13b). Relatively high differential stresses are expected for initiation of shear bands via cracking at stage I. For our averaged P-T estimates, the yielding differential stress can be up to 250 MPa as reported from experiments on cracking of quartz single crystals (Tarantola et al., 2012; Diamond and Tarantola, 2015).

Dynamic recrystallization of quartz via dislocation creep in the vicinity of microcracks and shear bands at stage II allowed us to evaluate stresses and strain rates by using the recrystallized quartz grains paleopiezometer of Stipp and Tullis (2003), corrected after Holyoke and Kronenberg (2010), and the flow law of Paterson and Luan (1990) (combination of flow laws and piezometers after Boutonnet et al. (2013)). For the early phases of stage II characterized by exclusive recrystallization of quartz due to slip along microcracks, the average grain size of 8 microns (Fig. 11e; red grains in grain map in 11b) indicate differential stress of 94 MPa and strain rate $1.8 \cdot 10^{-14} \text{ s}^{-1}$ (Fig. 13a). For later phases of stage II when recrystallization of quartz is accompanied by dissolution-precipitation creep of microcline, the average grain size of recrystallized quartz increases to 41 and 81 microns (Fig. 11e), which corresponds to decrease in differential stresses to 26 and 17 MPa and strain rates to $3.2 \cdot 10^{-16} \text{ s}^{-1}$ and $9 \cdot 10^{-17} \text{ s}^{-1}$, respectively.

The decrease in stresses and strain rates recorded by the recrystallized quartz layer at late phases of stage II is clearly related to strain partitioning into weaker dissolution-precipitation creep dominated layer of microcline (Fig. 11c). At the same time, assuming that both layers deform at constant stress conditions (Reuss bound), the flow stresses for dissolution-precipitation creep of microcline are identical to quartz and range between 26 and 17 MPa (Fig. 13a). In addition, assuming a constant displacement rate along SASZ and approximate 10 times increase in width of shear bands at stage II with respect to stage I implies 10 times decrease in strain rate. Thus for given P-T conditions and stresses the dissolution-precipitation in microcline would accommodate deformation at strain rates $1.8 \cdot 10^{-15} \text{ s}^{-1}$ (Fig. 13a). The stage III is characterized by localization of deformation into white mica bands, which must have been accompanied by a substantial drop in stress as the deformation in walls of these newly established micro-shear zones stopped. At the same time the localization of deformation would lead to an increase in strain rate in such bands to the initial values of $1.8 \cdot 10^{-14} \text{ s}^{-1}$ obtained for the localized deformation at stage I. By plotting the existing mica flow laws into the stress and strain rate space, for the given temperatures and strain rates the substantial stress decrease is fully satisfied only by the flow law of Mares and Kronenberg (1993) showing 5.75 MPa at $1.8 \cdot 10^{-14} \text{ s}^{-1}$ (Fig. 13a.).

Table 2. Material constants and form of flow laws used in Fig. 13

mineral	reference	A [MPa ⁻ⁿ s ⁻¹]	Q [KJ*mol ⁻¹]	n	flow law
quartz	Paterson and Luan, 1990	6.5*10 ⁻⁸	135	3.1	$\dot{\epsilon}=A*\sigma^{n*f_{(H_2O)}}*e^{-Q/RT}$
white mica	Mares and Kronenberg, 1993	4*10 ⁻²⁰	31	11	$\dot{\epsilon}=A*\sigma^n*e^{-Q/RT}$
white mica	Mariani et al., 2006	10 ^{7.23}	270	1.13	$\dot{\epsilon}=A*\sigma^{-(n+1)/2}*e^{-Q/RT}$
biotite	Kronenberg et al., 1990	1.2*10 ⁻³⁰	51	18	$\dot{\epsilon}=A*\sigma^n*e^{-Q/RT}$

Tab. 2 Experimentally derived material constants and form of flow laws used in Figure 13. In order to compare individual flow laws, the flow law for white mica of Mariani et al. (2006) relating shear strain rate and shear stress was rewritten into formula relating equivalent strain rate and equivalent stress. The power law form of the flow law for white mica of Mares and Kronenberg (1993) was obtained by fitting their original data, except for the experiments performed at $2.3*10^{-4} \text{ s}^{-1}$ in their strain rate-stepping series as these show unrealistic low stresses (see their table 3).

5.4 Strength evolution at brittle-plastic transition

Strength of crustal rocks at brittle-plastic transition is controlled by their composition, interconnectivity of weak material and preferred deformation mechanism (e.g. Handy, 1990; Shea and Kronenberg, 1993; Kohlsted et al., 1995). When mechanical behaviour of quartz is chosen to approximate the strength of crust, it can be concluded that ductile shearing accommodated by plasticity of quartz near the brittle-plastic transition requires the highest yielding stresses and therefore represents the strongest part of the continental crust (Behr and Platt, 2014). However when phyllosilicates are used instead, it is the frictional strength of faults that controls the crustal strength (Mariani et al., 2006; Wintsch and Yeh, 2013). The above-described decrease of rock strength in SASZ implies that rheology of the brittle-plastic transition may be rather dynamic and not steady-state, and that the crustal strength evolves in time and eventually can be reduced to extremely small values <10 MPa (Fig. 13b). The observed decrease in strength is mainly due to switches in deformation mechanisms and changes in mineral phases accommodating deformation. Phase transformations thus appears as one of the key mechanism for reaction softening and/or deviation from steady-state behaviour (Stünitz and Tullis, 2001; Oliot et al., 2010; Goncalves et al., 2012; Okudaira et al., 2015), especially at the brittle-plastic transition where sufficient permeability and income of acidic meteoric water may lead to substantial increase in the white mica content (Wintsch et al., 1995; Wintsch and Yeh, 2013). On the other hand, as demonstrated in this work it is also the crystal plastic and brittle processes in combination with neocrystallization that lead to efficient phase mixing and formation of relatively weak matrix bands. In addition, the documented evolution in these micro-scale shear zones indicate that shear zones can both become wider or narrower during the same deformation event and therefore the constant stress and steady-state approach used for estimates on width of major crustal shear zones

(Platt and Behr, 2011) may not be applicable in evolving shear zones.

6 Conclusions

Formation and evolution of S-C fabrics in the South Armorican Shear Zone have been evaluated by detailed microstructural study including determination of mineral chemistry, quantitative microstructural analysis, transmission electron microscopy and textural analysis by EBSD method. Our observations suggest that the two fabrics formed at distinct P-T conditions indicating magmatic-subsolidus conditions >550 °C for the S fabric and 300-350 °C at 100-400 MPa for the C fabric/shear bands. The evolving microstructure within shear bands revealed important switches in deformation mechanisms related to positive feedbacks between deformation and chemical processes and imposing mechanical constraints on evolution of the brittle-plastic transition. Three stages of shear band evolution were identified. Stage I is associated with initiation of shear bands via formation of microcracks acting as precursors for shear bands. For the estimated P-T conditions, the yielding differential stresses for cracking can be up to 250 MPa. The initial phases of stage II are associated with localized slip along microcracks which triggered subgrain rotation recrystallization via dislocation creep in neighbouring quartz at relatively high differential stresses of 94 MPa and strain rate $1.8 \cdot 10^{-14} \text{ s}^{-1}$. The recrystallization facilitated income of fluids and precipitation of microcline along quartz grain boundaries, which resulted in phase mixing and widening of shear bands. The slip along shear bands at later phases of stage II was mainly accommodated by dissolution-precipitation creep of microcline with some contribution of grain boundary sliding. Coeval recrystallization of quartz shows increase in grain size/decrease in stress which by using the isostress Reuss bounding behaviour allowed us to quantify stresses for dissolution-precipitation creep in the range of 17-26 MPa accommodating deformation at strain rate $1.8 \cdot 10^{-15} \text{ s}^{-1}$. Stage III is characterized by precipitation and interconnection of white mica grains resulting into localized slip along white mica bands. The deformation in white mica is accommodated by dislocation creep at strain rate $1.8 \cdot 10^{-14} \text{ s}^{-1}$ and stress 5.75 MPa. These mechanical data point to non-steady-state evolution of the brittle-plastic transition in the South Armorican Shear Zone characterized by major weakening to strengths lower than 10 MPa.

Acknowledgements

This work was supported by research grants from Charles University Grant Agency

(GAUK) 5041/2012 and the Czech Science Foundation (GACR) 14-15632S. Ralf Milke and Ondrej Lexa are thanked for numerous valuable discussions on this topic. Richard Wirth and Anja Schreiber are thanked for the help with TEM study.

References

Agard, P., Augier, R., Monié, P. (2011). Shear band formation and strain localization on a regional scale: Evidence from anisotropic rocks below a major detachment (Betic Cordilleras, Spain), *Journal of Structural geology*, 33, 114-131.

Auzanneau, E., Schmidt, M. W., Vielzeuf, D., Connolly, J.A.D. (2010). Titanium in phengite: a geobarometer for high temperature eclogites, *Contributions to Mineralogy and Petrology* 159:1-24.

Ballèvre, M., Bosse, V., Ducassou, C., Pitra, P. (2009). Palaeozoic history of the Armorican Massif: models for the tectonic evolution of the suture zones, *Comptes Rendus Geoscience*, 341 (2), 174-201.

Behr, W. M., Platt, J. P. (2014). Brittle faults are weak, yet the ductile middle crust is strong: Implications for lithospheric mechanics, *Geophysical Research Letters*, 41 (22), 8067-8075.

Bercovici, D. (2003). The generation of plate tectonics from mantle convection, *Earth and Planetary Science Letters*, 205(3), 107-121.

Berthé, D., Choukroune, P., Jegouzo, P. (1979 a). Orthogneiss, mylonite and non coaxial deformation of granites: the example of the South Armorican Shear Zone, *Journal of Structural Geology* 1, 1, 31-42.

Berthé, D., Choukroune, P., Gapais, D. (1979 b). Orientations préférentielles du quartz et orthogneissification progressive en régime cisailant: l'exemple du cisaillement sud-armoricain, *Bull. Minéral.* 102, 265-272.

Blenkinsop, T.G., Treloar, P.J. (1995). Geometry, classification and kinematics of S-C and S-C' nfabrics in the Mushandike area, Zimbabwe, *Journal of Structural Geology*, 17 (3), 397-408.

Boutonnet, E., Leloup, P. H., Sassier, C., Gardien, V., Ricard, Y. (2013). Ductile strain rate measurements document long-term strain localization in the continental crust, *Geology*, 41(8), 819-822.

Bukovská, Z., Jeřábek, P., Lexa, O., Konopásek, J., Janák, M., Košler, J. (2013). Kinematically unrelated C—S fabrics: an example of extensional shear band cleavage from the Veporic Unit (Western Carpathians), *Geologica Carpathica*, 64 (2), 103-116.

Čadek, J. (1988). *Creep in Metallic Materials*, 372 pp., Elsevier, Amsterdam, Netherlands.

Chopin, F., Schulmann, K., Skrzypek, E., Lehmann, J., Dujardin, J. R., Martelat, J. E., Lexa, O., Corsini M., Edel, J. B., Štípská, P., Pitra, P. (2012). Crustal influx, indentation, ductile thinning and gravity redistribution in a continental wedge: Building a Moldanubian mantled gneiss dome with underthrust Saxothuringian material (European Variscan belt), *Tectonics*, 31(1), doi:10.1029/2011TC002951.

Coggon, R., Holland, T. (2002). Mixing properties of phengitic micas and revised garnet-phengite thermobarometers, *Journal of Metamorphic Geology*, 20, 683-96.

Connolly, J.A.D. (2005). Computation of phase equilibria by linear programming: a tool for geodynamic modeling and its application to subduction zone decarbonation, *Earth and Planetary Science Letters*, 236 (1), 524-541.

Crider, J.G., Peacock, D.C. (2004). Initiation of brittle faults in the upper crust: a review of field observations, *Journal of Structural Geology*, 26(4), 691-707.

Diamond, L.W., Tarantola, A. (2015). Interpretation of fluid inclusions in quartz deformed by weak ductile shearing: Reconstruction of differential stress magnitudes and pre-deformation fluid properties, *Earth and Planetary Science Letters*, 417, 107-119.

Fukuda, J.I., Okudaira, T., Satsukawa, T., Michibayashi, K. (2012). Solution–precipitation of K-feldspar in deformed granitoids and its relationship to the distribution of water, *Tectonophysics*, 532, 175-185.

Fusseis, F., Handy, M. (2008). Micromechanisms of shear zone propagation at the brittle-viscous transition, *Journal of Structural Geology* 30, 1242-1253.

Gapais, D. (1989). Shear structures within deformed granites: Mechanical and thermal indicators, *Geology* 17, 1144-1147.

Gapais, D., White, S.H. (1982). Ductile shear bands in a naturally deformed quartzite, *Textures and Microstructures*, 5, 1-17.

Gapais, D., Fiquet, G., Cobbold, P.R. (1991). Slip system domains, 3. New insights in fault kinematics from plane-strain sandbox experiments, *Tectonophysics*, 188 (1), 143-157.

Gillam, B. G., Little, T. A., Smith, E., Toy, V.G. (2013). Reprint of Extensional shear band development on the outer margin of the Alpine mylonite zone, Tatare Stream, Southern Alps, New Zealand, *Journal of Structural Geology*, 64, 115-134.

Goncalves, P., Oliot, E., Marquer, D., Connolly, J.A.D. (2012). Role of chemical processes on shear zone formation: an example from the Grimsel metagranodiorite (Aar massif, Central Alps), *Journal of Metamorphic Geology*, 30 (7), 703-722.

Gueydan, F., Leroy, Y. M., Jolivet, L., Agard, P. (2003). Analysis of continental midcrustal strain localization induced by microfracturing and reaction-softening, *Journal of Geophysical Research: Solid Earth* (1978–2012), 108(B2), doi: 10.1029/2001JB000611.

Gumiaux, C., Gapais, D., Brun, J. P., Chantaine, J., Ruffet, G. (2004). Tectonic history of the Hercynian Armorican shear belt (Brittany, France), *Geodinamica Acta*, 17 (4), 289-307.

Hielscher, R., Schaeben, H. (2008). A novel pole figure inversion method: specification of the MTEX algorithm, *Journal of Applied Crystallography*, 41 (6), 1024–1037.

Hiraga, T., Miyazaki, T., Yoshida, H., Zimmerman, M.E. (2013). Comparison of microstructures in superplastically deformed synthetic materials and natural mylonites: Mineral aggregation via grain boundary sliding, *Geology*, 41(9), 959-962.

Hirth, G., Tullis, J. (1994). The brittle-plastic transition in experimentally deformed quartz aggregates, *Journal of Geophysical Research: Solid Earth* (1978–2012), 99 (B6), 11731-11747.

Holland, T., Baker, J., Powell, R. (1998). Mixing properties and activity-composition relationships of chlorites in the system MgO-FeO-Al₂O₃-SiO₂-H₂O, *European Journal of Mineralogy*, 10, 395-406.

Holland T., Powell, R. (1998). An internally consistent thermodynamic data set for phases of petrological interest, *Journal of Metamorphic Geology*, 16, 309-43.

Holyoke, C. W., Kronenberg, A.K. (2010) Accurate differential stress measurement using the molten salt cell and solid salt assemblies in the Griggs apparatus with applications to strength, piezometers and rheology, *Tectonophysics*, 494(1), 17-31.

Holyoke, C. W., Tullis, J. (2006). Mechanisms of weak phase interconnection and the effects of phase strength contrast on fabric development, *Journal of Structural Geology*, 28 (4), 621-640.

Janoušek, V., Farrow, C. M., Erban, V. (2006). Interpretation of whole-rock geochemical data in igneous geochemistry: introducing Geochemical Data Toolkit (GCDkit), *Journal of Petrology*, 47, 1255-1259.

Jeřábek, P., Stünitz, H., Heilbronner, R., Lexa, O., Schulmann, K. (2007). Microstructural-deformation record of an orogen-parallel extension in the Vepor Unit, West Carpathians, *Journal of Structural Geology*, 29 (11), 1722-1743.

Karato, S. (1983). Importance of anelasticity in the interpretation of seismic tomography, *Geophysical Research Letters*, 20 (15), 1623–1626.

Keller, L. M., Abart, R., Stünitz, H., De Capitani, C. (2004). Deformation, mass transfer and mineral reactions in an eclogite facies shear zone in a polymetamorphic metapelite (Monte Rosa nappe, western Alps), *Journal of Metamorphic Geology*, 22 (2), 97–118.

Kilian, R., Heilbronner, R., Stünitz, H. (2011). Quartz grain size reduction in a granitoid rock and the transition from dislocation to diffusion creep, *Journal of Structural Geology*, 33, 1265-1284.

Knipe, R. J., Wintsch, R.P. (1985). Heterogeneous deformation, foliation development, and metamorphic processes in a polyphase mylonite, in *Metamorphic Reactions*, Springer New York, pp. 180-210.

Kohlstedt, D. L., Evans, B., Mackwell, S.J. (1995). Strength of the lithosphere: constraints

imposed by laboratory experiments. *Journal of Geophysical Research*, 100, 17-587.

Kretz, R. (1969). On the spatial distribution of crystals in rocks, *Lithos*, 2, 39-66.

Kretz, R. (1994). *Metamorphic crystallization*. Wiley.

Krohe, A. (1990). Local variations in quartz [c]-axis orientations in non-coaxial regimes and their significance for the mechanics of S-C fabrics, *Journal of Structural Geology*, 12, 8, 995-1004.

Kronenberg, A. K., Kirby, S. H., Pinkston, J. (1990). Basal slip and mechanical anisotropy of biotite, *Journal of Geophysical Research: Solid Earth* (1978–2012), 95 (B12), 19257-19278.

Law, R. D., Schmid, S. M., Wheeler, J. (1990). Simple shear deformation and quartz crystallographic fabrics: a possible natural example from the Torridon area of NW Scotland, *Journal of Structural Geology*, 12 (1), 29-45.

Lexa, O. (2003). Numerical approach in structural and microstructural analyses. PhD Thesis, Charles University in Prague, 138 p.

Lister, G. S., Williams, P.F. (1979). The partitioning of deformation in flowing rock masses. *Tectonophysics*, 92(1), 1-33.

Lister G. S., Snoke, A.W. (1984). S-C Mylonites, *Journal of Structural Geology*, 6 (6), 617-638.

Lloyd, G. E. (2004). Microstructural evolution in a mylonitic quartz simple shear zone: the significant roles of dauphine twinning and misorientation, Geological Society, London, Special Publications, 224 (1), 39-61.

Mancktelow, N. S., Pennacchioni G. (2013). Late magmatic healed fractures in granitoids and their influence on subsequent solid-state deformation, *Journal of Structural Geology*, 57, 81-96.

Mariani, E., Brodie, K. H., Rutter, E.H. (2006). Experimental deformation of muscovite shear zones at high temperatures under hydrothermal conditions and the strength of phyllosilicate-bearing faults in nature, *Journal of Structural Geology*, 28 (9), 1569-1587.

Mares, V. M., Kronenberg, A.K. (1993). Experimental deformation of muscovite. *Journal of Structural Geology*, 15 (9), 1061-1075.

Means, W. D. (1995). Shear zones and rock history, *Tectonophysics*, 247, 157-160.

Menegon, L., Pennacchioni, G., Heilbronner, R., Pittarello, L. (2008). Evolution of quartz microstructure and c-axis crystallographic preferred orientation within ductilely deformed granitoids (Arolla unit, Western Alps), *Journal of Structural Geology*, 30 (11), 1332-1347.

Menegon, L., Stünitz, H., Nasipuri, P., Heilbronner, R., Svahnberg, H. (2013). Transition from fracturing to viscous flow in granulite facies perthitic feldspar (Lofoten, Norway), *Journal of Structural Geology*, 48, 95-112.

- Michibayashi, K., Murakami, M. (2007). Development of a shear band cleavage as a result of strain partitioning, *Journal of Structural Geology*, 29, 1070-1082.
- Miller, C. F., Stoddard, E. F., Bradfish, L. J., Dollase, W.A. (1981). Composition of plutonic muscovite: genetic implications, *Canadian Mineralogist*, 19, 25-34.
- Misra, S. (2011). Deformation localization at the tips of shear fractures: An analytical approach, *Tectonophysics*, 503, 182-187.
- Neumann, B. (2000). Texture development of recrystallised quartz polycrystals unravelled by orientation and misorientation characteristics, *Journal of Structural Geology*, 22 (11), 1695-1711.
- Newton, R. C., Charlu, T. V., Kleppa, O.J. (1980). Thermochemistry of the high structural state plagioclases, *Geochemica Cosmochimica Acta*, 44, 933-41.
- Okudaira, T., Takeshita, T., Hara, I., Ando, I.J. (1995). A new estimate of the conditions for transition from basal $\langle a \rangle$ to prism $[c]$ slip in naturally deformed quartz, *Tectonophysics*, 250 (1), 31-46.
- Okudaira, T., Jeřábek, P., Stünitz, H., Füsseis, F. (2015). High-temperature fracturing and subsequent grain-size-sensitive creep in lower crustal gabbros: Evidence for coseismic loading followed by creep during decaying stress in the lower crust?, *Journal of Geophysical Research: Solid Earth*.
- Oliot, E., Goncalves, P., Marquer, D. (2010). Role of plagioclase and reaction softening in a metagranite shear zone at mid-crustal conditions (Gotthard Massif, Swiss Central Alps), *Journal of Metamorphic Geology*, 28(8), 849-871.
- Oliot, E., Goncalves, P., Schulmann, K., Marquer, D., Lexa, O. (2014). Mid-crustal shear zone formation in granitic rocks: Constraints from quantitative textural and crystallographic preferred orientation analyses, *Tectonophysics*, 612-613, 63-80.
- Passchier, C.W. (1984). The generation of ductile and brittle shear bands in a low-angle mylonite zone. *Journal of Structural Geology*, 6 (3), 273-281.
- Passchier, C.W. (1991). Geometric constraints on the development of shear bands in rocks, *Geologie en Mijnbouw*, 70, 203-211.
- Paterson, M.S., Luan, F.C. (1990). Quartzite rheology under geological conditions, *Geological Society, London, Special Publications*, 54 (1), 299-307.
- Peč, M., Stünitz, H., Heilbronner, R. (2012). Semi-brittle deformation of granitoid gouges in shear experiments at elevated pressures and temperatures, *Journal of Structural Geology*, 38, 200-221.
- Pennacchioni, G., Mancktelow, N.S. (2007). Nucleation and initial growth of a shear zone network within compositionally and structurally heterogeneous granitoids under amphibolite facies conditions, *Journal of Structural Geology*, 29, 1757-1780.

Platt, J.P. (1984). Secondary cleavages in ductile shear zones, *Journal of Structural Geology*, 6 (4), 439-442.

Platt, J.P., Behr, W.M. (2011). Grain size evolution in ductile shear zones: Implications for strain localization and the strength of the lithosphere, *Journal of Structural Geology*, 33(4), 537-550.

Platt, J. P., Vissers, R.L.M. (1980). Extensional structures in anisotropic rocks, *Journal of Structural Geology*, 2 (4), 397–410.

Powell, R., Holland, T. (1999). Relating formulations of the thermodynamics of mineral solid solutions: Activity modeling of pyroxenes, amphiboles, and micas, *American Mineralogist*, 84, 1-14.

Ranalli, G. (1987). *Rheology of the Earth*, Allen and Unwin, Boston.

Rutter, E.H. (1999). On the relationship between the formation of shear zones and the form of the flow law for rocks undergoing dynamic recrystallization, *Tectonophysics*, 303 (1), 147-158.

Rutter, E.H., Holdsworth, R.E., Knipe, R.J. (2001). The nature and tectonic significance of fault-zone weakening: an introduction, Geological Society, London, Special Publications, 186 (1), 1-11.

Rybacki, E., Morales, L. F. G., Naumann, M., Dresen, G. (2014). Strain localization during high temperature creep of marble: The effect of inclusions, *Tectonophysics*, 634, 182-197, <http://doi.org/10.1016/j.tecto.2014.07.032>.

Schmid, S. M. (1982). Microfabric studies as indicators of deformation mechanisms and flow laws operative in mountain building, in *Mountain Building Processes*, edited by K. J. Hsii, Academic Press, London, 95-110.

Schulmann, K., Mlčoch, B., Melka, R. (1996). High-temperature microstructures and rheology of deformed granite, Erzgebirge, Bohemian Massif, *Journal of Structural Geology*, 18 (6), 719-733.

Shea, W. T., Kronenberg, A.K. (1993). Strength and anisotropy of foliated rocks with varied mica contents, *Journal of Structural Geology*, 15 (9), 1097-1121.

Simpson, C., Schmid, S.M. (1983). An evaluation of criteria to deduce the sense of movement in sheared rocks, *Geological Society of America Bulletin*, 94 (11), 1281-1288.

Stipp, M., Tullis, J. (2003). The recrystallized grain size piezometer for quartz, *Geophysical Research Letters*, 30 (21).

Stipp, M., Stünitz, H., Heilbronner, R., Schmid, S.M. (2002). The eastern Tonale fault zone: a 'natural laboratory' for crystal plastic deformation of quartz over a temperature range from 250 to 700 C, *Journal of Structural Geology*, 24 (12), 1861-1884.

Stünitz, H., Tullis, J. (2001). Weakening and strain localization produced by syn-deformational reaction of plagioclase, *Int J Earth Sciences (Geol Rundsch)*, 90, 136-148.

Tarantola, A., Diamond, L. W., Stünitz, H., Thust, A., Peč, M. (2012). Modification of fluid inclusions in quartz by deviatoric stress. III: influence of principal stresses on inclusion density and orientation, *Contributions to Mineralogy and Petrology*, 164 (3), 537-550.

Tartèse, R., Boulvais, P. (2010). Differentiation of peraluminous leucogranites “en route” to the surface, *Lithos*, 114, 353-368.

Tartèse, R., Poujol, M., Ruffet, G., Boulvais, P., Yamato, P., Košler, J. (2011). New U-Pb zircon and $40\text{ Ar}/39\text{ Ar}$ muscovite age constraints on the emplacement of the Lizio syn-tectonic granite (Armorican Massif, France), *Comptes Rendus Geoscience*, 343(7), 443-453.

Tartèse, R., Boulvais, P., Poujol, M., Chevalier, T., Paquette, J. L., Ireland, T. R., Deloule, E. (2012). Mylonites of the South Armorican Shear Zone: Insights for crustal-scale fluid flow and water–rock interaction processes, *Journal of Geodynamics*, 56, 86-107.

White, S.H., Burrows, S.E., Carreras, J., Shaw, N.D., Humphreys, F.J. (1980). On mylonites in ductile shear zones, *Journal of Structural Geology*, 2, 175-187.

Wilks, K.R., Carter, N.L. (1990). Rheology of some continental lower crustal rocks, *Tectonophysics*, 182 (1), 57-77.

Wintsch, R.P., Christoffersen, R., Kronenberg, A.K. (1995). Fluid-rock reaction weakening of fault zones, *Journal of Geophysical Research: Solid Earth (1978–2012)*, 100(B7), 13021-13032.

Wintsch R. P., Yeh, M.W. (2013). Oscillating brittle and viscous behavior through the earthquake cycle in the Red River Shear Zone: Monitoring flips between reaction and textural softening and hardening. *Tectonophysics*, 587, 46-62.

Wintsch, R. P., Yi, K. (2002). Dissolution and replacement creep: a significant deformation mechanism in mid-crustal rocks, *Journal of Structural Geology*, 24 (6), 1179-1193.

Wirth, R. (2009). Focused Ion Beam (FIB) combined with SEM and TEM: Advanced analytical tools for studies of chemical composition, microstructure and crystal structure in geomaterials on a nanometre scale, *Chemical Geology*, 261 (3), 217-229

PRESSURE SOLUTION IN ROCKS: FOCUSED ION BEAM/TRANSMISSION ELECTRON MICROSCOPY STUDY ON ORTHOGNEISS FROM SOUTH ARMORICAN SHEAR ZONE, FRANCE

Zita Bukovská^{1,2}, Richard Wirth³, Luiz F.G. Morales⁴

¹ Charles University in Prague, Faculty of Science, Institute of Petrology and Structural Geology, Albertov 6, 12843 Prague 2, Czech Republic

² Czech Geological Survey, Klárov 3, 118 21 Prague 1, Czech Republic

³ Helmholtz Centre Potsdam, German Research Centre GFZ, Section 3.3, Telegrafenberg, 14476 Potsdam, Germany

⁴ Helmholtz Centre Potsdam, German Research Centre GFZ, Section 3.2, Telegrafenberg, 14476 Potsdam, Germany

Abstract

In order to characterize the μm -to- nm structures related to operation of pressure solution on phase boundaries in naturally deformed rocks, we have performed a detailed focused ion beam/transmission electron microscopy study in ultramylonite samples from South Armorican Shear Zone (France) that focused on grain boundary scale. We have studied phase boundaries between quartz, K-feldspar and white mica both in 2 and 3D and compare our evidences with theoretical dissolution-precipitation models in the current literature. The dissolution (re)precipitation processes lead to the development of different features at different phase boundaries. In both quartz-white mica and quartz – K-feldspar phase boundaries, voids were ubiquitously observed. These voids have different shapes and the development of some of them is crystallographically controlled. In addition, part of these voids might be filled with vermiculite. Amorphous leached layers with kaolinite composition were observed at the boundaries of K-feldspar-quartz and K-feldspar–white mica. The development of different features along the phase boundaries is mainly controlled by the crystallography of the phases sharing a common interface, together with the presence of fluids that either leaches or directly dissolve the mineral phases. In addition, the local dislocation density in quartz may play an important role during pressure solution. We suggest that the nano-scale observations of the quartz – white mica phase boundaries show direct evidence for operation of island-and-channel model as described in Wassmann and Stöckhert (2013), while K-feldspar – quartz phase boundaries represents amorphous layers formed via interface-coupled dissolution-reprecipitation as described by Hellmann et al. (2012).

Keywords: *pressure solution, dissolution precipitation, transmission electron microscopy, focused ion beam, island and channel model, leached layer*

1 Introduction

Pressure solution is an important mass-transfer mechanism driven by dissolution and (re)precipitation in rocks that contain intergranular fluids and may operate in a wide range of rock types and temperature, pressure conditions (e.g. Rutter, 1976; Wheeler, 1987; Spiers and Schutjens, 1990; Stöckhert et al., 1999; Wassmann and Stöckhert, 2012; 2013; Gratier et al., 2013). Dissolution-precipitation is widely studied in laboratory experiments covering a broad scale of conditions. This includes studies on chemical and biochemical weathering (e.g. Hellmann et al., 2012; Daval et al., 2013; Bray, 2014), archaeological findings damage (e.g. Rodriguez-Navarro and Benning, 2013) or during mineral replacement (e.g. Putnis and Putnis, 2007; Putnis, 2009; Hövelmann et al., 2010; Putnis and John, 2010) where precipitation occurs in the absence of external stresses and the process is purely chemically driven. Once dissolution-precipitation occurs in presence of external stresses, such as in compaction studies (e.g. Renard et al., 2000; Miyakawa and Kawabe, 2014), we refer to pressure solution. It is a well-studied process that is driven not only by chemical changes but above all by deformation within the whole upper crust (e.g. Rutter, 1983; Knipe and Wintsch, 1985; Wintsch et al., 1991; Gratier et al., 2013). The effects of pressure solution have also been modelled in terms of shear zone initiation (e.g. Fletcher, 1998) and in relation to processes connected to faulting and crack sealing during earthquake ruptures (e.g. Gratier et al., 2003). The main indicative features for operation of pressure solution at microscale are truncated grains, displacement of layering on certain planes if the contact is indented, stylolites, fibrous vein fill, fibrous overgrowth of grains in strain shadows and truncated chemical zoning patterns (e.g. Rutter, 1983; Passchier and Trouw, 1996; Wassmann and Stöckhert, 2013). At the nanoscale strong evidence of dissolution-precipitation processes are rough surfaces of grains, where the surfaces of two adjacent grains across the partially opened phase boundary do not fit geometrically because their parts have been dissolved.

The general model for pressure solution at micro- to nanoscale suggests the presence of a thin fluid film/phase at the interface of different grains, so that these grains are completely wetted. However, pressure solution may occur as island and channel structures, where interconnected fluid pockets or films along the grain boundaries are separated by islands (e.g. Lehner, 1995; Wassmann and Stöckhert, 2013; and references therein). Adjacent grains within these islands form a regular grain or phase boundary. The model of island and channel flow by Wassmann and Stöckhert (2013) includes dissolution at interfaces with an electrochemically rendered surface layer that is followed by short range diffusional transport

in channels with diameter of 10 to 100 nm. The diffusional transport merge into fluid phase along channels connected to the grain edges by channels of 100 nm to 1 μm . The transport upscale through network of tubes and microcracks and later to large scale focused fluid flow in fractures. In this case the sinks might be represented by any free interface.

Grain and phase boundary dissolution normally occurs when these boundaries are inclined at high angle to an instantaneous shortening direction, leading to high differential stresses in the region in the vicinity of the interface. Dissolution is followed by diffusive transport of dissolved ions within the fluid film and eventual (re)precipitation that may or may not occur locally. For the operation of such mechanism, the space for fluid transport has to be available, either in the form of porosity, partially-opened grain boundaries or fractures. In natural rocks such as granites and quartzites, the grains and phase boundaries are usually not perfectly straight, and many grain and phase boundaries might be partially opened (Kruhl et al., 2013) thus forming an interconnected network. If a fluid phase is present at the grain/phase boundary and the interface is simultaneously subject to high differential stress, dissolution occurs at the surface where solubility of a phase is enhanced and higher density of crystal lattice defects occurs.

There is a number of studies focusing on the experimental aspects of the dissolution precipitation creep, most of them done on natural rocks. Some examples includes the importance of pressure solution on the fracture sealing (e.g. Knipe et al., 1993; Nelson et al., 1999), mylonite to ultramylonite development (e.g. Mancktelow et al., 1998; Menegon et al., 2008; Billia et al., 2013) and high pressure rocks (e.g. Wassmann and Stöckhert, 2012; 2013) however, the link to the pressure solution on grain boundary scale is lacking.

In the present study we show microstructural evidences for pressure solution within the common crustal phase system of mica - quartz – feldspathic rocks via transmission electron microscopy (TEM) coupled with focused ion beam scanning electron microscopy (FIB-SEM) methods. Although there is a number of papers focusing on dissolution-precipitation creep, we will mainly discuss the models of Wassmann and Stöckhert (2013) and Hellmann et al. (2012) for which we found direct evidence in our natural samples.

2 Geological setting and sample description

The South Armorican Shear Zone (SASZ) in European Variscides represents a major tectonic zone dividing the Central Armorican and the South Armorican Massif in France (Ballèvre et al., 2009; Fig. 1a). This subvertical shear zone has approximately WSW-ENE

strike and consists of several branches spreading over hundreds of kilometres from westernmost Brittany to Vendée-Poitou region. The SASZ bears subhorizontal lineation, records right-lateral movement and is associated with development of S-C fabrics (Berthé et al., 1979).

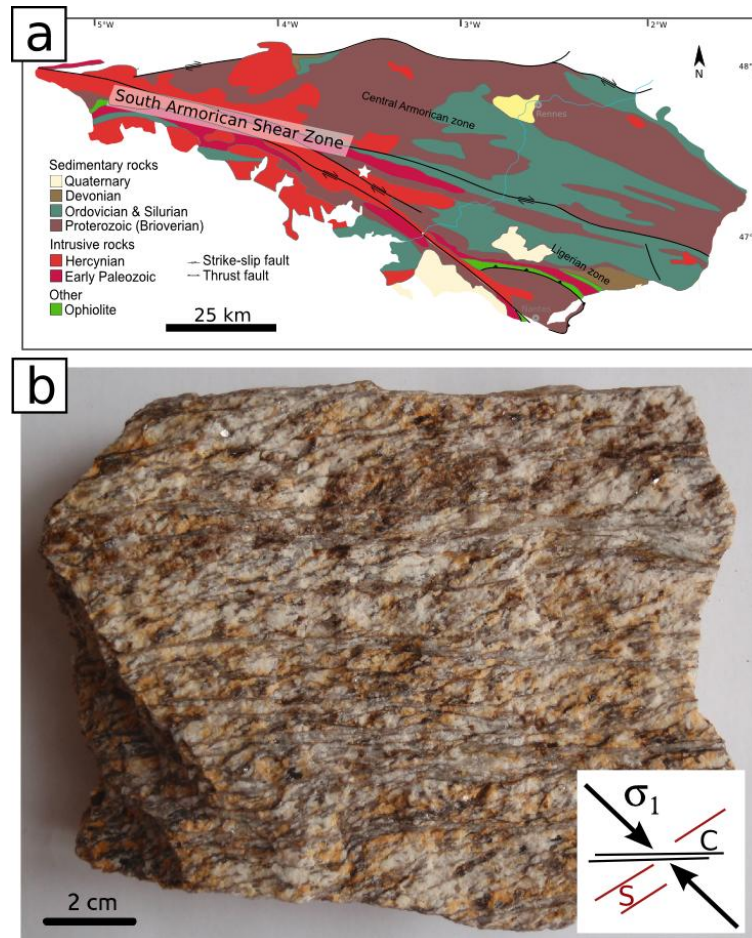


Fig. 1 a) Geological map of Armorican domain in Brittany, France with location of South Armorican Shear Zone and sample location (white star). b) Sample of orthogneiss with S-C fabric and estimated orientation of maximum compressive stress (σ_1) with respect to the S and C surfaces

Samples of an orthogneiss from one of the granitic plutons crosscut by the shear zone were chosen to study the interfaces of muscovite, quartz and K-feldspar. The original rock is a peraluminous leucogranite (Tartèse and Boulvais, 2010) deformed syntectonically to orthogneiss. The deformation within the shear zone led to the development of S-C fabrics (Fig. 1b), that were firstly described in this locality in the classical work of Berthé et al. (1979). The deformation evolution of these rocks includes different episodes of brittle and ductile deformation, where pressure solution plays an important role, as evidenced by quartz, K-feldspar and white micas that occur in the orthogneisses (Fig. 2). The studied S-C fabrics

were formed with decrease of temperature connected to the cooling of plutons down to cataclasis (Tartèse et al., 2012). Numerous types of fluids (reaching from crustal fluids to meteoric water) were documented from the South Armorican Shear Zone. These operated during different stages of the cooling and shear zone activity (Tartèse et al., 2012).

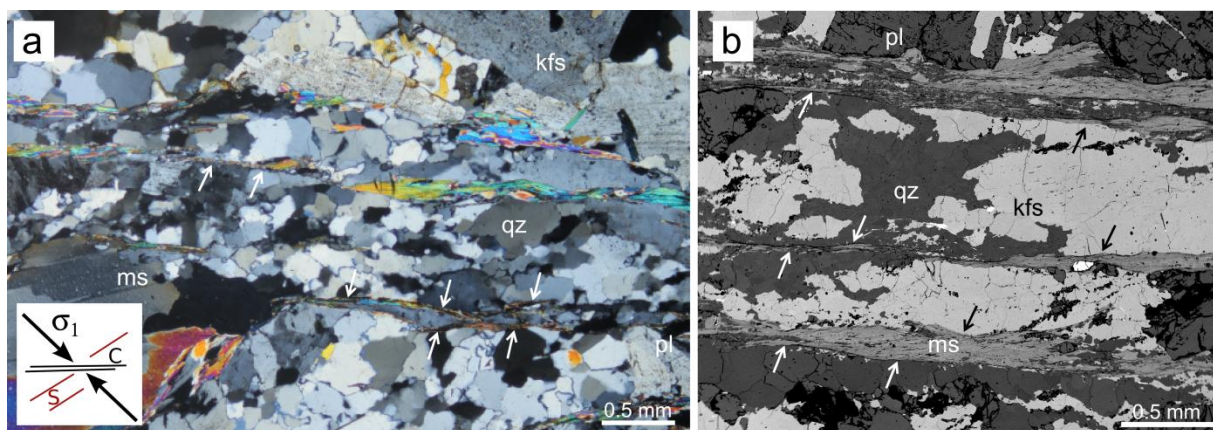


Fig. 2 a) Optical micrograph (crossed polarizers) of orthogneiss composed mainly of quartz, K-feldspar and muscovite. The arrows point at locations with pressure solution features such as sheet silicates in contact with quartz or K-feldspar and flattened grain shape. Orientation of maximum compressive stress (σ_1) is given with respect to the S-C fabric. b) BSE image of orthogneiss with matrix formed by quartz and K-feldspar with plagioclase porphyroclasts that is crosscut by muscovite. The white arrows indicate quartz – muscovite interfaces and black arrows K-feldspar – muscovite interfaces where pressure solution process was studied. Abbreviations: kfs – K-feldspar, ms – muscovite, pl – plagioclase, qz – quartz

The samples C fabric (shear bands) is parallel to the shear zone trace, where the orientation of maximum component of compressive stress on regional scale is oblique (at about 45°) to the shear zone. In order to relate the orientation of the observed pressure solution features, the orientation of the C fabric is shown in each figure and thus can be the features related to regional stress field.

The first evidences for the occurrence of pressure solution are already visible under the optical microscope, where mica grains form straight phase boundaries with quartz and K-feldspar grains (Fig. 2a and 2b, respectively). The quartz and K-feldspar phase boundaries are truncated by micas along the phase boundary, forming a new phase boundaries. The mineral assemblage that is present with the pressure solution features in the S-C fabric includes quartz, K-feldspar, white mica and chlorite.

3 Analytical techniques and sample preparation

TEM foils ($0.15 \mu\text{m}$ thick) were prepared directly from preselected areas in the thin-section via the focused ion beam technique (FIB) in a FEI FIB200 instrument following the

procedure described by Wirth (2009). We have studied TEM foils containing quartz – white mica and K-feldspar – white mica phase boundaries. The foils were cut both normal to the thin section surface and the phase boundaries. The TEM analyses were performed in a FEI Tecnai F20 X-Twin TEM operating at 200 kV. Both FIB and TEM are operating at the German Research Centre for Geosciences (GFZ Potsdam). Initial imaging and phase characterization via high angle annular dark field (HAADF) imaging coupled with energy-dispersive X-ray spectroscopy (EDS) was followed by high resolution TEM along the phase boundaries. We also performed FIB-SEM nanotomography along a quartz-muscovite phase boundary to observe its three-dimensional aspect via the Slice-and-View® approach. Through this technique, the 3D imaging of a certain volume of the target material is achieved by repeating the sputtering process with the focused ion beam intercalated with electron beam imaging in a Dual-Beam machine® (FIB/SEM), with the sample normally tilted at 52°. For this study we selected an area of 20 x 20 µm, where a protective layer of 1.5µm of Pt was first deposited to prevent FIB damage. We then sputtered material out from the frontal and lateral sides of this region with the FIB operating at accelerating voltage of 30 kV and beam current of 30 nA. The frontal surface was then “polished” with the FIB operating at 3 nA beam current, and the slice-and-view process was conducted at the same conditions. The selected region was sliced normal to the grain boundaries. Electron imaging was obtained via the back-scattered detector via accelerating voltage of 20 kV and beam current of 8 nA, and each slice of sputtered material had 100 nm. All this procedure was performed in a FEI Quanta 3D FEG dual beam machine, also operating at GFZ Potsdam.

4 Results

4.1 Quartz – white mica phase boundary

The phase boundaries of white mica – quartz were studied in a foil where a muscovite grain neighbours two quartz grains (Fig. 3b). We selected a region affected by pressure solution, due to the straight phase boundary between mica and the quartz – K-feldspar matrix (Fig. 2, 3a), where the quartz and K-feldspar grains are crosscut by mica.

The mica grain has its c-axis perpendicular to the foliation and the phase boundary runs parallel to the white mica basal plane. Quartz has highly irregular phase boundary with the mica grain (Fig. 3b). Along this boundary, voids are opened towards the quartz grains (Fig. 3b) and in some locations muscovite interpenetrates quartz. Another important observation is that the white mica and the quartz crystal are rarely in direct contact to each other along the

phase boundary due to the numerous voids along this boundary. These voids vary in size from few nanometres up to approx. 100 nm (Fig. 4) and have different shapes. They might have been filled with a fluid that has escaped into the vacuum during sample preparation or might be filled with vermiculite as revealed by EDS.

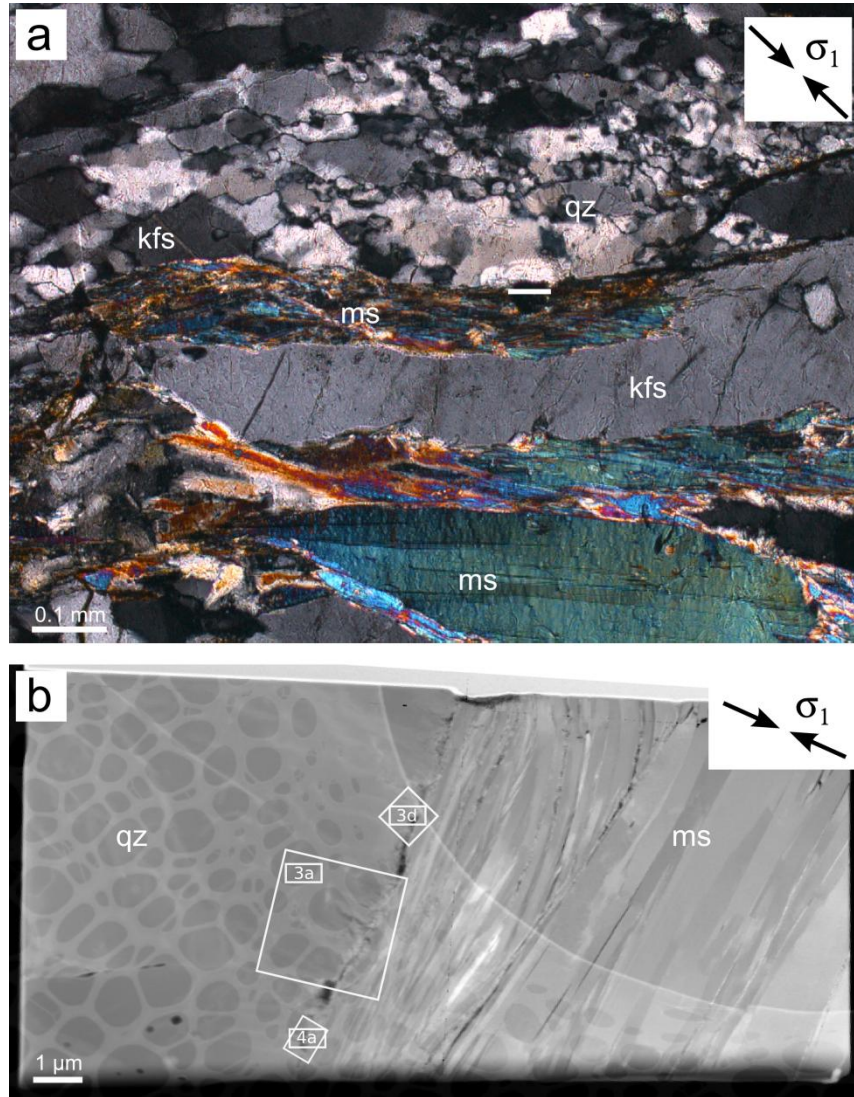


Fig. 3 a) Optical micrograph (crossed polarizers) of orthogneiss sample with quartz – muscovite grain boundaries where the TEM foil was prepared and FIB 3D slice-and-view produced. The phase boundary area is marked with white line over the hole that was sputtered during FIB slicing. b) The high-angle annular dark field (HAADF) image of the foil cut across the quartz – muscovite phase boundary with location of figures 3 a, 3 d and 4 a along the phase boundary indicated. Porosity along the grain boundaries is visible as dark spots or elongated contrasts. The underlying carbon grid the foil rests on forms the bubble structure below the foil. Assumed orientation of maximum compressive stress (σ_1) is given to each figure. Abbreviations as in Fig. 1.

The roughness of the quartz grain surface is pronounced, and is visualized by the dark contrast of quartz imaged with a low indexed zone axis parallel to the electron beam (Fig. 4). Locations in quartz where voids penetrate deeper into quartz grain are characterized by higher

dislocation density, with the dislocation lines directly penetrating through to the surface of the grain (Fig. 4b, 5a, 5b).

In this foil (Fig. 3b) the dissolution of quartz produces very different features in two neighbouring quartz grains. In the upper grain, the quartz surface is extremely irregular (Fig. 4) and voids vary from trapezium to triangle shapes, with smaller embayments into the quartz. The lower grain on the other hand is triangular-shaped with straight and oriented crystal surfaces (Fig. 5). The void spaces are filled with nanocrystalline, needle-like vermiculite. The surface of quartz in the lower grain with triangular voids (Fig. 5a) is smooth. Determination of the crystallographic orientation of the phase boundary planes was carried out via high resolution TEM (HRTEM, Fig. 5b) and fast Fourier transform (FFT) of HRTEM lattice fringe images. Fig. 5c is a dark-field image (01-10 reflection) of the same location as in Fig. 5a. The respective planes of a triangular void represent crystallographic positive and negative rhombs (01-11) and (10-11) (as depicted at Fig. 5a, b).

In order to document the phenomena of dissolution of quartz boundaries at the contact to mica in three dimensions, we performed a nanotomography study (Fig. 6 a-d and Supplementary material – to be found on CD) via FIB/SEM in the same location where the foils were extracted (Fig. 3a). The phase boundary separates quartz and mica grains (Fig. 6a - d, left and right respectively) with a small K-feldspar grain that is grown in between quartz grains (Fig. 6b, c, d). The voids are shown as these appear along the phase boundary causing increase in phase boundary porosity. The movie documents the phenomena of partially opened phase boundaries, as well as opening and closing of the dissolution sinks (voids; Fig. 6), detail illustrated in the Figs. 4 and 5.

Quartz – mica dissolution features were also found in quartz enclosed in micas (Fig. 7a, d) that are crosscutting the quartz – K-feldspar (Fig. 2b) matrix. Quartz has highly irregular grain shape (Fig. 7a, d), that is better visualized in the dark field image (Fig. 7c). Quartz grains document different dissolution features that depend on the orientation relationship between adjacent mica and quartz grains. Partially opened grain boundaries represented by pores along the phase boundary of mica and quartz are also commonly observed, depending on the grain orientation (Fig. 7a).

Small dissolved voids are found along the quartz phase boundary neighbouring with mica basal plane (Fig. 7b, e) with dislocations connected to the tips of dissolved voids (Fig. 7b). In those locations where the basal plane of mica is (approximately) perpendicular to the quartz grain, mica grew over quartz and penetrated into its structure (Fig. 7e). In other parts of the

phase boundary, no voids are observed, but amorphous material occurs (Fig. 7e). The mica basal plane is inclined at an angle of ca. 45° with respect to the quartz surface, as documented by HRTEM by the presence of fringes of both grains (Fig. 7f) and measured with FFT of

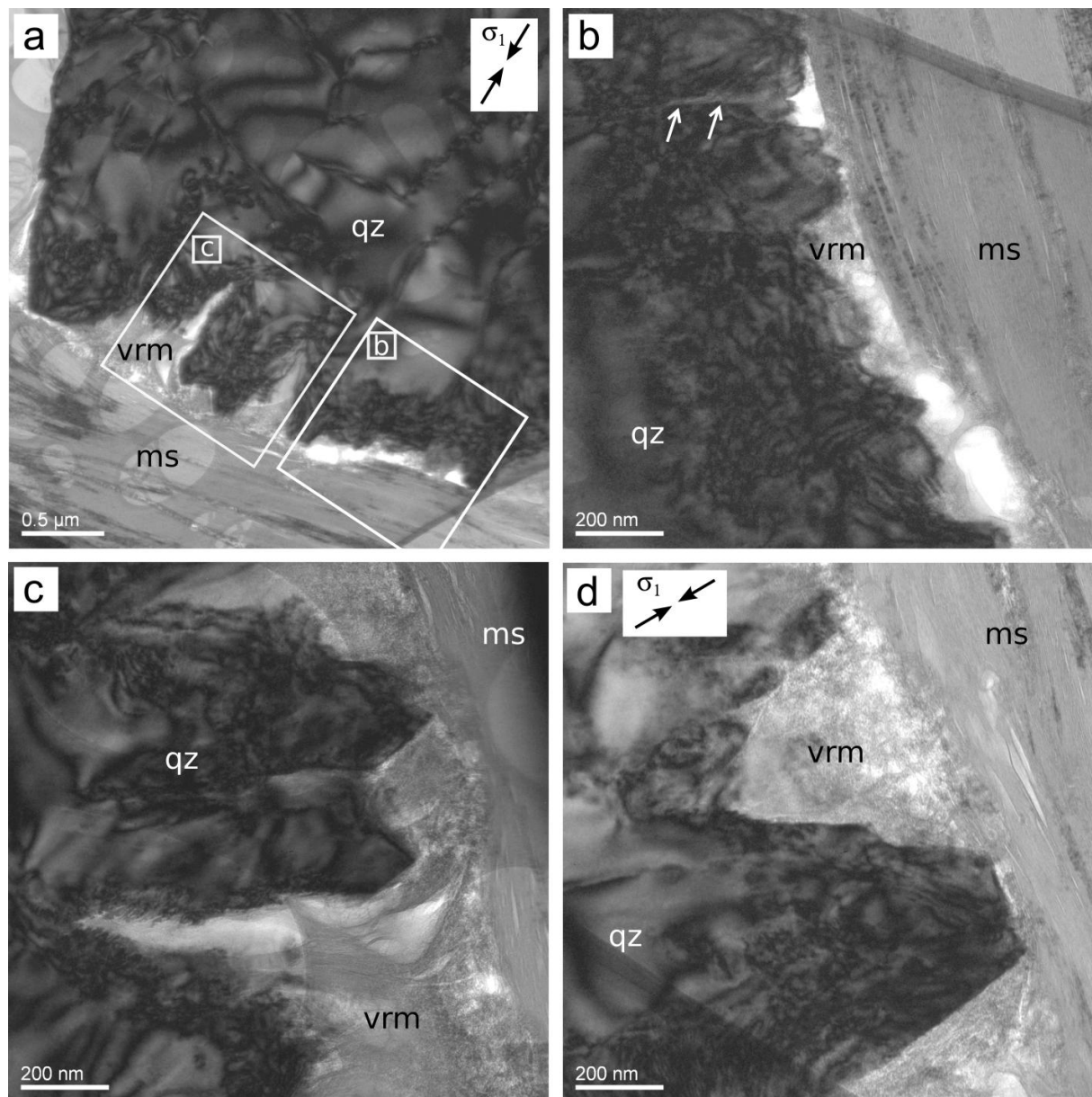


Fig. 4 TEM bright-field images of a quartz – muscovite phase boundary. Quartz grains are dissolved and voids have been formed. Newly formed vermiculite is found within the opened phase boundary and the voids. The dislocation density increases towards the quartz phase boundary. The shadow of the underlying perforated carbon film is visible in some locations of the images. a) Quartz grain with high dislocation density and the location of the detailed images 3b and 3c indicated as boxes. b) Detailed image of the interface quartz-muscovite showing very rough surface of quartz with many dissolved embayments on a different scale. White arrows show the dislocation connected to the end of voids thus indicating preferential solution of the quartz in the vicinity of the dislocation core. c) Protruding embayment into the quartz grain partially filled with vermiculite growing on the dissolved quartz surfaces. d) Pronounced almost triangular voids with straight quartz surfaces. The voids are filled with vermiculite. Assumed orientation of maximum compressive stress (σ_1) is given to each figure. Abbreviations: ms – muscovite, qz – quartz, vrm – vermiculite

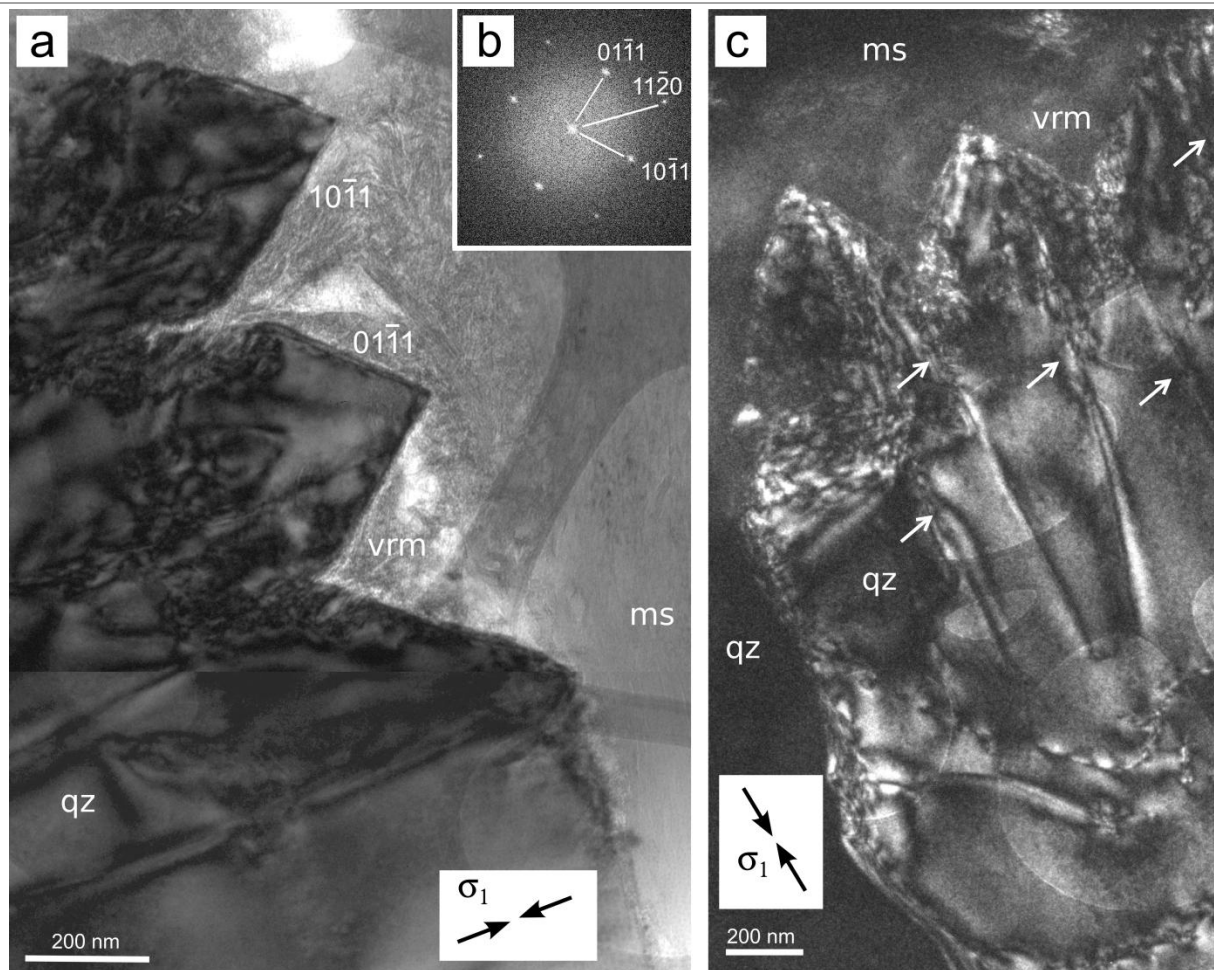


Fig. 5 a) Composite TEM bright-field image of dissolved quartz interface quartz-muscovite with triangular voids. Note the straight surfaces of quartz correspond to (01-10) and (10-11) crystal faces. The now opened phase boundary is filled with vermiculite. b) Diffraction pattern (FFT of HREM image) of the partially dissolved quartz grain. c) Corresponding dark-field image of quartz grain with dislocations connected to the tips of triangular voids marked by white arrows. Assumed orientation of maximum compressive stress (σ_1) is given to each TEM figure. Abbreviations as in Fig. 3

HRTEM (Fig. 7g). The original thickness of the amorphous layer is approximately 15 nm, but the irradiation damage of quartz during imaging caused the thickness to increase to 29 nm as shown on Fig. 7f. The observed dissolution features are closely connected to the preferred orientation of the mica.

4.2 K-feldspar – white mica phase boundary

In the orthogneiss matrix, quartz is neighbouring K-feldspar (Fig. 2b). The evidence for pressure solution was therefore also expected to occur along the K-feldspar – white mica grain boundaries because the K-feldspar grains are truncated at the contact to mica in a same way as quartz. The partially opened phase boundaries of both phases are rough and do not correspond in shape to each other, suggesting partial dissolution of one or both phases.

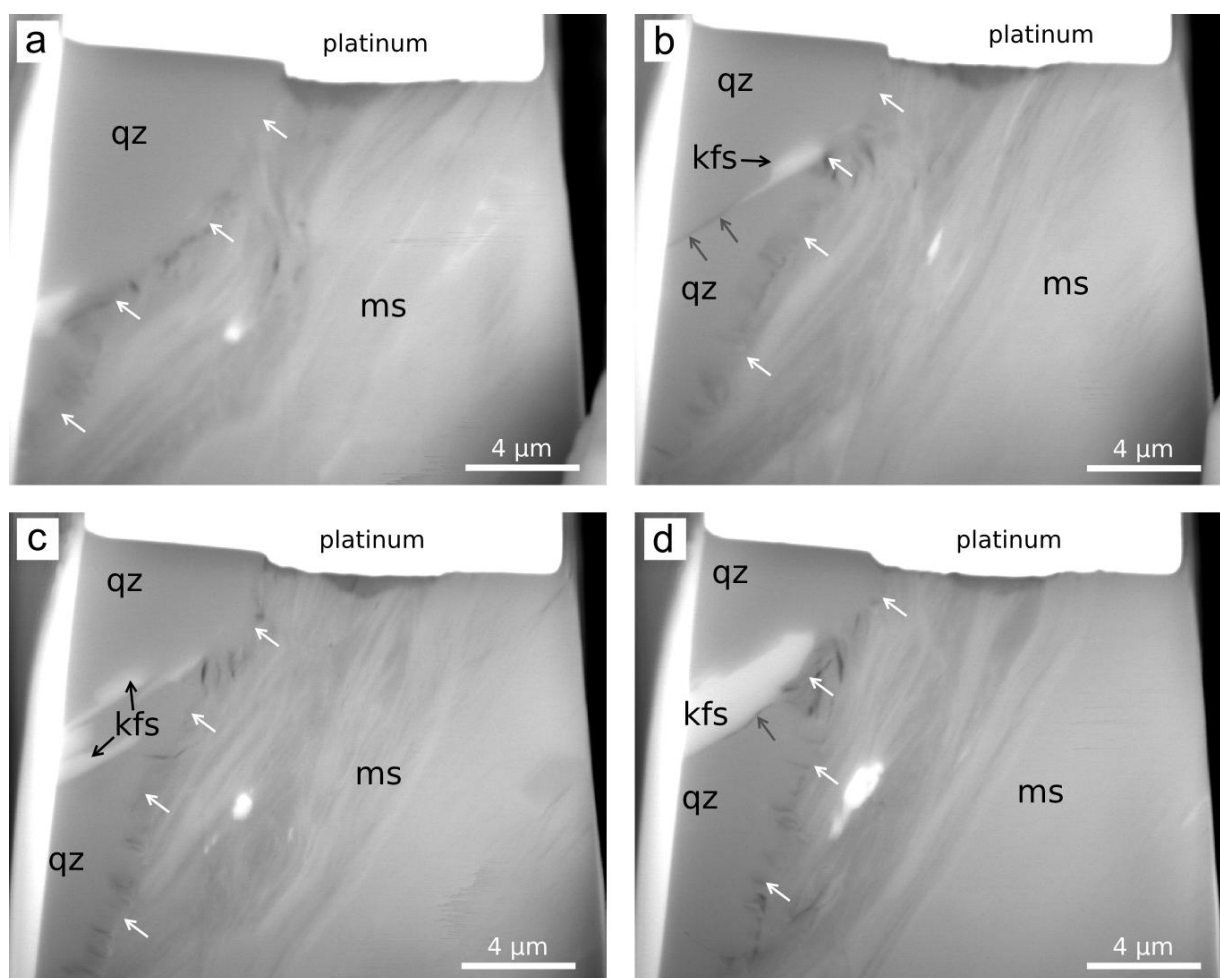


Fig. 6 a) - d) FIB images from 3D slice-and-view of the quartz (left) and muscovite (right). The opening and closing of larger voids along the grain boundaries (white arrows) is demonstrated in the movie (supplementary material). The precipitation of small K-feldspar grain (white) is possible because of presence of partially opened grain boundaries (grey arrows) which allows the fluid flow

The phase boundaries contain numerous pores (Fig. 8a), especially when the basal plane of mica is parallel to the phase boundary with K-feldspar (Fig. 8a, d). When the mica basal plane is inclined at high angle to the phase boundary with feldspar, the former tends to grow over the latter (Fig. 8b, c). The mica initially grows over the K-feldspar grains, which at more evolved stages leads to disaggregation and isolation of smaller K-feldspar or quartz grains, such as the smaller K-feldspar grain in Fig. 8c (in the upper part of the image) isolated from the larger K-feldspar grain in the same image. This process also affected the smaller quartz grain nearby.

Another related feature found in direct contact with the phase boundaries affected by dissolution are low-angle grain boundaries. In a bulged K-feldspar grain, a low-angle grain boundary evolves in continuation of mica – K-feldspar interface (Fig. 8b). Often these are connected to the voids at the opened K-feldspar – mica interfaces (Fig. 8d). Higher

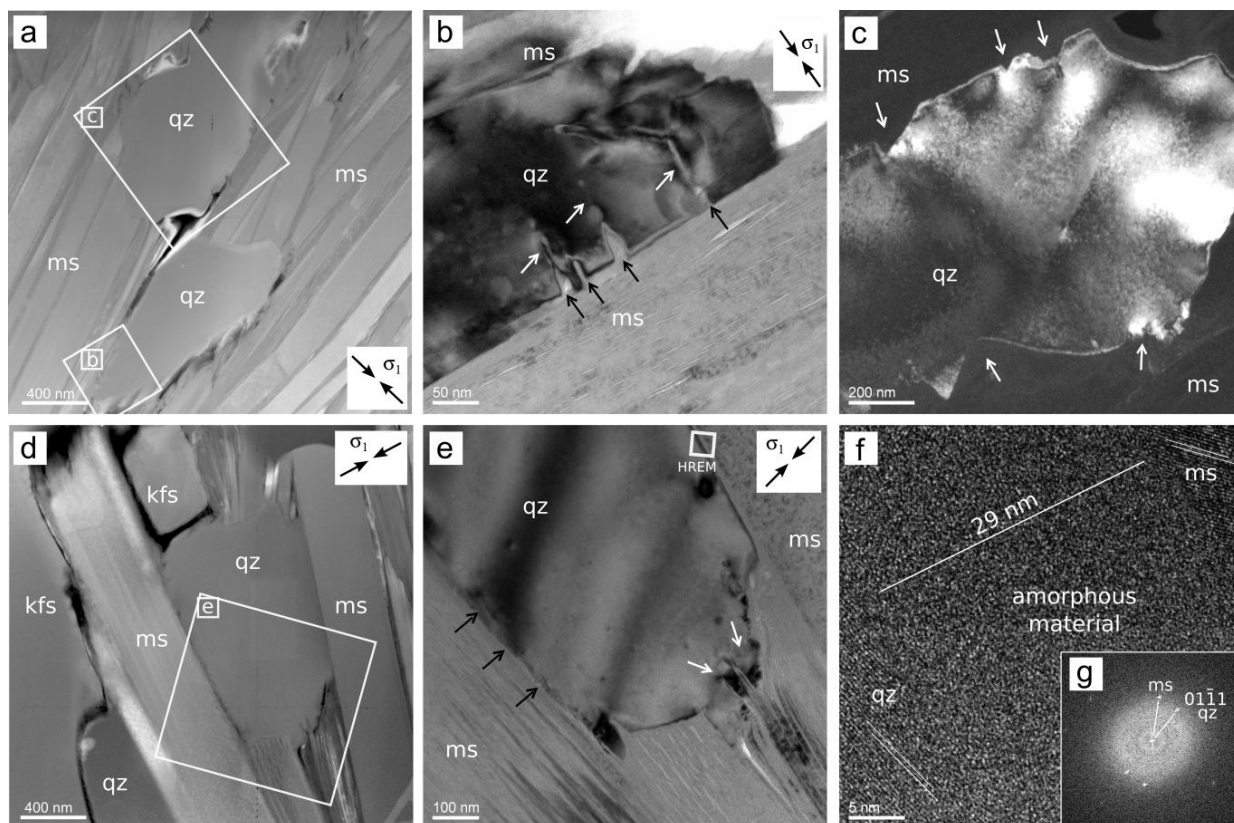


Fig. 7 Quartz – muscovite grain boundaries of small quartz grains enclosed in a muscovite matrix. a) HAADF image of two quartz grains within muscovite with numerous voids along the quartz-muscovite interface. The bright contrast surrounding the pore between quartz and muscovite is caused by redeposited gallium during FIB foil preparation thus indicating an open pore space prior to FIB milling. The location of Fig. 6b and 6c is indicated by white rectangles. b) TEM bright-field image of quartz grain with dark diffraction contrast together with small voids (black arrows) along the phase boundary quartz muscovite at the basal plane of muscovite. The voids are filled with non-crystalline material. The tips of voids mark the endpoints of dislocation lines (white arrows) that protrude out of the quartz grain surface. c) TEM dark-field image of a quartz grain with dissolved surfaces imaged at different scale. Note the in form of small embayments or much more altered grain boundaries resulting in an irregular shape of the grain (some of them marked by white arrows). d) HAADF image of quartz grains within muscovite with location of Fig. 4e. e) TEM bright-field image of quartz surrounded by muscovite. Pressure solution is different depending on the orientation relationship of quartz and muscovite. The quartz grain with small embayments (marked by black arrows) at the interface parallel to the basal plane of muscovite. At those locations where the muscovite basal planes of muscovite are approximately perpendicular to the quartz surface, the muscovite grows into the quartz (white arrows). Other quartz-muscovite interfaces display amorphous material at the quartz- muscovite phase boundary (Fig. 6f). f) TEM lattice fringe image of the quartz-mica interface. In the lower left corner and in the upper right corner lattice fringes from quartz and muscovite are visible. The width of the amorphous material is 29 nm, however, the original extent measured was only 15 nm. During the exposure time of the sample to electron irradiation during HREM imaging quartz and muscovite are damaged resulting in disappearing lattice fringes of both minerals. Quartz is more affected by irradiation damage than muscovite. g) Diffraction pattern (FFT of HREM Fig. 6f) of the interface region. Assumed orientation of maximum compressive stress (σ_1) is given to each figure

dislocation density is present close to the interface (Fig. 8e).

Amorphous phase may also be developed along parts of the partially open phase boundaries between mica and K-feldspar (Fig. 8f). The phase is localized directly at the partially opened K-feldspar phase boundary and may contain some porosity (Fig. 8f, 9a, 9b). The interface of K-feldspar and amorphous phase is straight and very well visible because the diffraction contrast of K-feldspar ends abruptly at the interface (Fig. 9c) with non-crystalline material. Chemical composition of this amorphous phase resembles that of kaolinite. Even though the K-feldspar is dissolved in a different way in comparison to quartz, the dislocations are still connected to the phase boundary and proceed into the K-feldspar grain (Fig. 8f, 9b).

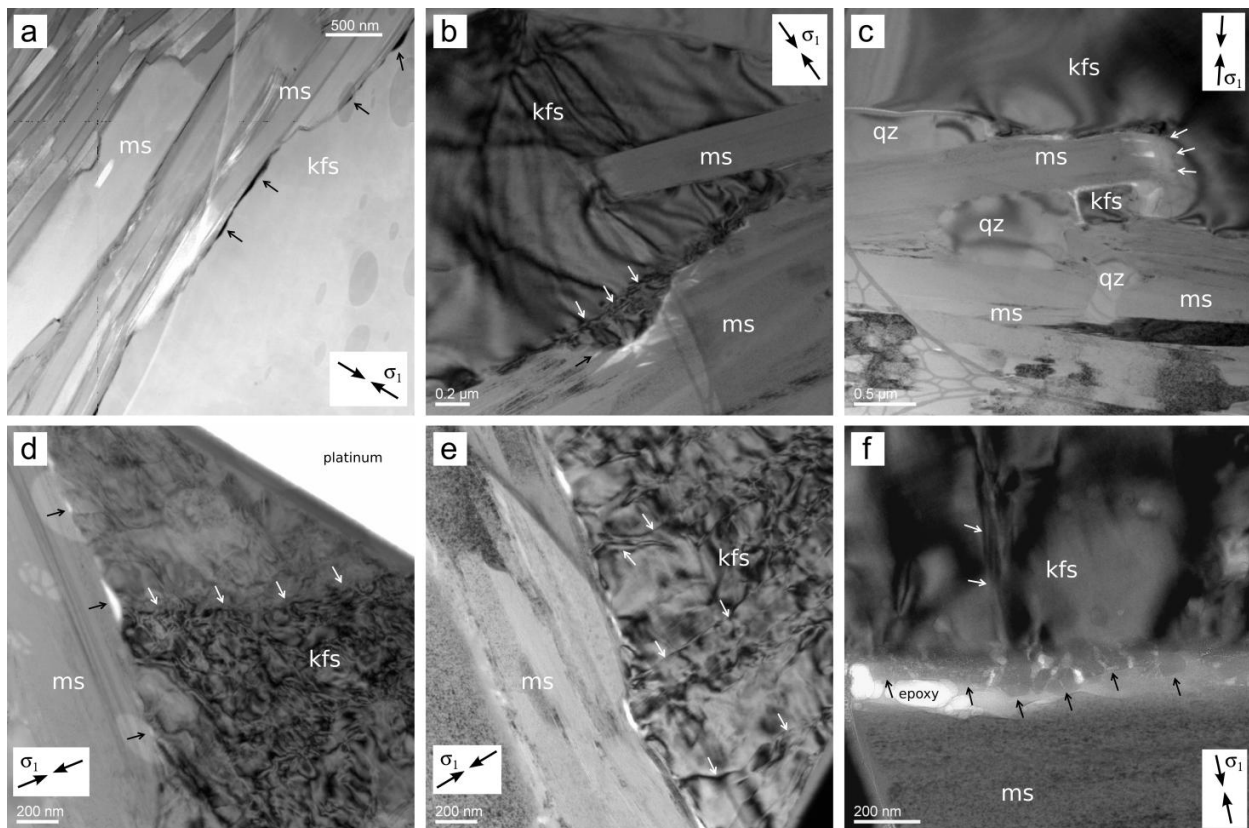


Fig. 8 a) HAADF image of a K-feldspar – muscovite interface which is partially opened. The partially opened phase boundary is displayed by dark contrasts indicated by black arrows. b)-f) TEM bright-field images of K-feldspar – muscovite phase boundaries. b) K-feldspar – muscovite phase boundary. The K-feldspar bulges into the muscovite. The bulged area of K-feldspar is separated from the K-feldspar by a low-angle grain boundary approximately at the position of the original interface K-feldspar - muscovite. Note the porosity at the tip of the bulge extending parallel to the basal planes of muscovite. c) K-feldspar grain being disintegrated by growth of muscovite (white arrows). d) Partially opened phase boundary of muscovite and K-feldspar (black arrows). Low-angle grain boundary in K-feldspar is indicated by white arrows. e) Dislocations (white arrows) protruding from the muscovite – K-feldspar phase boundary into the K-feldspar grain. f) Amorphous material (black arrows) at the K-feldspar - muscovite phase boundary forming patches on the K-feldspar surface. White spots present epoxy from sample preparation. Assumed orientation of maximum compressive stress (σ_1) is given to each figure

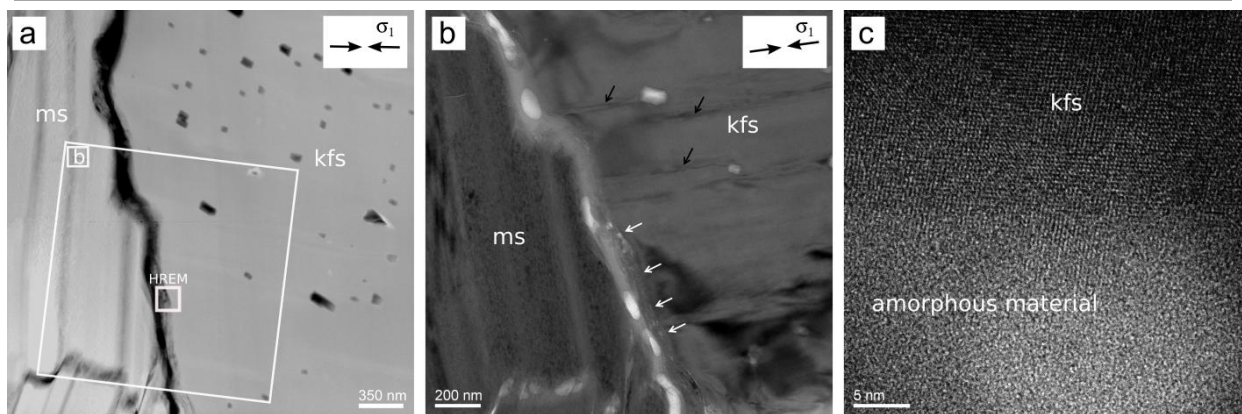


Fig. 9 a) HAADF image of a K-feldspar – muscovite interface with amorphous material at the K-feldspar surface with location of Fig. 8b and 8c indicated. b) Bright-field image of the interface with amorphous material at the K-feldspar surface (white arrows) and dislocations connected to the surface (black arrows). Amorphous material is represented by the absence of diffraction contrast. White areas at the interface represents epoxy from sample preparation, white spots within K-feldspars represent inclusions. c) HREM image of the interface of K-feldspar (crystalline, upper part) and amorphous material with approximate kaolinite composition (lower part). Assumed orientation of maximum compressive stress (σ_1) is given to each figure

5 Discussion

Observations of grain boundaries within quartz / K-feldspar and mica within crustal rocks show complex pressure solution features, such as truncated grains and phase boundaries. The studied grain and phase boundaries show presence of amorphous material, numerous partially opened grain boundaries and voids, resulting in the development of porosity.

Although the processes of dissolution and (re)precipitation are normally explained in terms of the effect of local high and low stresses acting in rocks in the presence of fluids, for certain rock types this might not be the case. Recently, Kruhl et al. (2013) has shown that partially opened grain and phase boundaries are commonly observed in different types of rocks, such as quartzites, granitoids and marbles. Our observations support this study and document a number of partially opened interfaces which serve as fluid pathways especially at the late stage of the rock evolution at temperature <300 °C, which is the temperature for the brittle-ductile transition in quartz (Voll, 1976). The presence of partially open grain and phase boundaries with highly irregular surfaces, where the geometries of the boundaries of opposite neighbour crystals do not match, is a clear evidence of partial dissolution along these interfaces.

The orientation of maximum compressive stress at the grain scale is complicated to assume therefore we can only make an estimate. The maximum compressive stress at the regional scale is oriented approximately at 45° to the shear zone (Fig. 10a). If we extrapolate the stress orientation towards the microscale, the maximum stress would be at 45° to the shear band

(C fabric orientation) in the thin section plane (Fig. 10a). These shear bands contain mica grains that are aligned within the fabric. Thus the orientation of the quartz – mica interfaces is parallel with the shear zone. Looking at the TEM foils the stress (σ_1) extrapolation is not that straight forward (Fig. 10b). Thin foils that were prepared for this study were cut from the thin sections perpendicular to the C fabric and at the same time mica basal planes as shown at Fig. 10. Therefore the orientation of maximum compressive stress on the TEM foil is not oriented at 45° to the mica C fabric. Assuming the foil as a plane we need to project the maximum compressive stress orientation which is thus perpendicular to most of the observed interfaces and mica basal planes. However this should be taken into account as an assumption since we do not have any control on the local stresses.

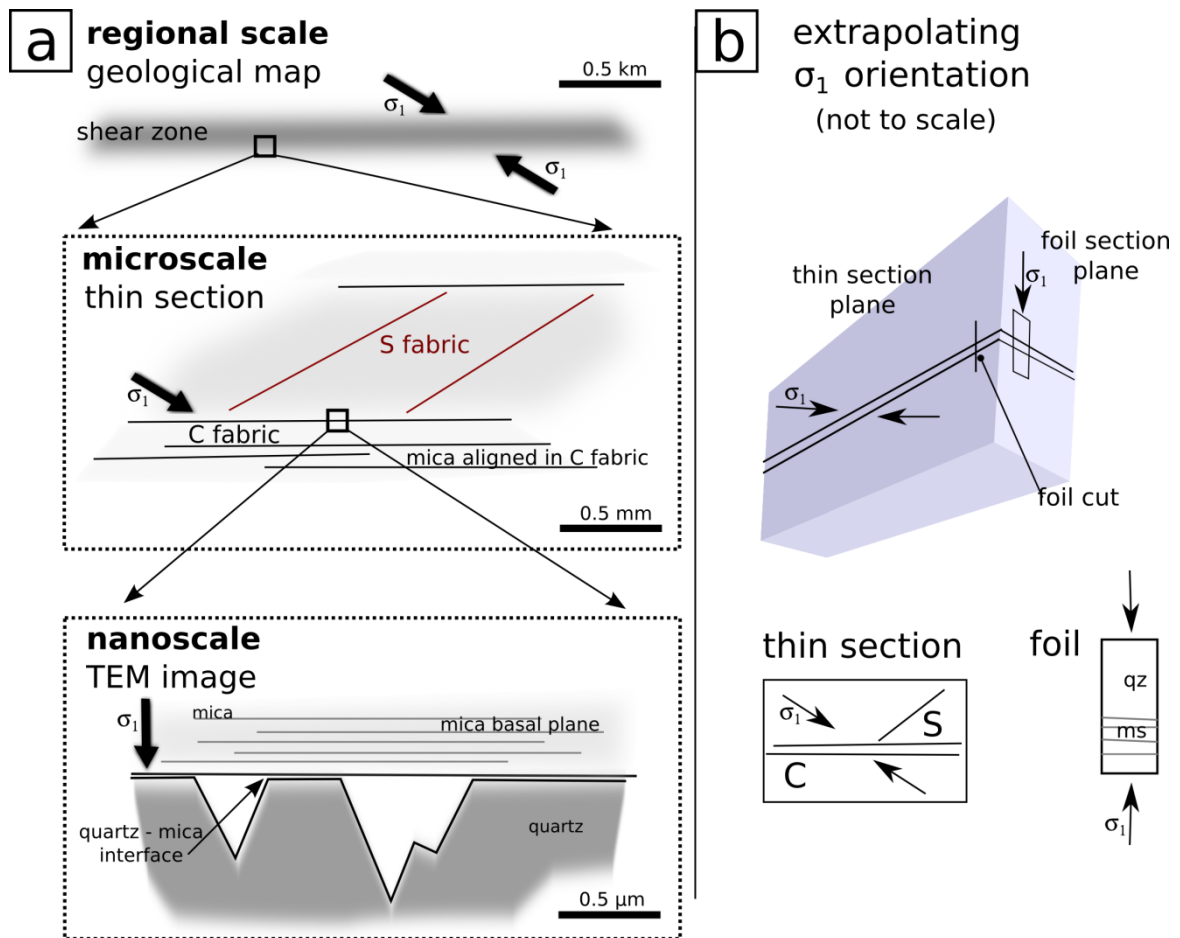


Fig. 10 Extrapolation of stress orientation from regional scale to the mineral interfaces: a) Orientation of maximum compressive stress (σ_1 , black arrow) at the regional scale applicable to the shear zone, at microscale within the thin section with respect to the S-C fabric and on nanoscale in the case of mineral interfaces of mica and quartz. b) Extrapolation of the σ_1 orientation from thin section to the perpendicular thin foil prepared for TEM. In order to assume the stress at the phase interface the foil is assumed to be planar and the σ_1 is suitably projected.

If we assume the maximum compressive stress orientation to 45° to the interface the effect of the maximum compressive stress to the interface with respect to the pressure solution might be questionable. Experimental works mostly assume the maximum compressive stress being perpendicular to the interface however, observed white mica – quartz interfaces with newly formed porosity have the maximum compressive stress oriented at 45° .

The dissolution of quartz when in contact with the white mica appears to be crystallographically controlled, as evidenced by the positive and negative rhomb planes of quartz in contact with the (001) plane of mica. At the same interface, irregular voids with trapezoid and triangle shapes are formed in quartz crystals of different orientations. These features are also observed in the nanotomography method, confirming the extent of this phenomenon in 3D. As discussed by Putnis and John (2010), the newly established porosity generated by dissolution allows fluid to be transported and precipitated with no need for solid-state diffusion. Similar voids were observed by Mancktelow et al. (1998) and Billia et al. (2013) in quartz or quartzo-feldspathic mylonites to ultramylonites, where grain boundary pores are expected to represent transient porosity evolved through dislocation-localized dissolution during dislocation creep of the ultramylonite. Similar features were also observed by Gratier et al. (2005) as experimental microstylolites in quartz where the maximum compressive stress was also perpendicular to the microstylolite interface.

At the white mica – quartz interfaces can be found both dissolution interfaces represented by amorphous or leached material and open voids in the same orientation. This suggests that there is strong effect of stress which can locally either cause leaching or open voids.

The model of island and channel structure based on the presence of a thin fluid film at the interface boundary explaining pressure solution operation on micro – nanoscale described by Wassmann and Stöckhert (2013) appears to be valid for the observations in the orthogneiss samples reported here. According to their model, the dissolution precipitation creep requires at least one fluid and one solid phase, chemically open system and association of dissolution precipitation with chemical changes. In case of the studied samples, the parts of the grain not dissolved represent the islands in the island and channel structure model, while the voids represent the channels of this model. The dissolved areas are commonly filled with vermiculite, which represents residual precipitated material from dissolved phases. The assumed orientation of compressive stress is also preferable for this model.

The model for dissolution precipitation creep in the sense of Wassmann and Stöckhert (2013) further comprise: (i) interface dissolution that might be restricted to load-bearing

islands with thin fluid film; (ii) diffusional transport into network of channels surrounding islands, (iii) diffusional transport through fluid along the channels; (iv) transport through 3D network of tubes and microcracks and (v) large scale focused fluid flow in fractures. The observed combination of voids with partially opened boundaries present numerous ways where fluid flow may operate within the system.

The chemical composition of K-feldspar and its boundary layer has been evaluated by EDS. The amorphous material layer observed in the K-feldspar interface represents K-feldspar leached by fluids operating at this interface, most probably at very low temperatures. In the leached layers, K is removed out of the structure of K-feldspar and an amorphous layer rich in silica and aluminium is preserved with a similar composition of kaolinite. The presence of amorphous layers formed via interface-coupled dissolution-reprecipitation was also observed by Hellmann et al. (2003) in experimentally altered plagioclase and Hellmann et al. (2012) in chemical weathering studies in multiple silicates. In both cases, the development of the leached layer was interpreted by the activation of dissolution reprecipitation mechanisms along the minerals interfaces (Hellmann et al., 2012) although without the presence of external stress and in free fluid. The main arguments of Hellmann et al. (2012) that unify laboratory and field chemical weathering were: (i) sharp chemical interfaces in the form of crystalline-amorphous boundary; (ii) cation depletion depths; (iii) fast rates providing the surface layers significantly exceeding diffusion rates. According to Hellmann et al. (2012) the main important processes include dissolution in a thin fluid film with pristine mineral lattice, coupled precipitation of porous amorphous phase and precipitation of amorphous silica even in undersaturated solution. Our observations show nanometre-sharp boundaries at the crystalline-amorphous interfaces, which seem to be formed at a single reaction front. Presented observations therefore support the conclusion of Hellmann et al. (2012) that interfacial dissolution reprecipitation is universal mineral-water alteration mechanism also in the presence of external stresses. Moreover the alteration of feldspars leading to its breakdown, growth of muscovite and the loss of K into fluid was shown to be significantly important in mylonites (Knipe and Wintsch, 1985).

The leached layer formation is extensively studied mainly with respect to weathering and building materials damage either through solid-state transformation (e.g. Casey et al., 1993) or through interface-coupled dissolution and subsequent precipitation (e.g. Hellmann et al., 2012; Ruiz-Agudo et al., 2012). We have observed amorphous phase with evolving porosity (Fig. 8f) that is assumed to be formed through interface-coupled dissolution-precipitation.

The newly formed porosity represents another possibility for fluid transport. Amorphous material is found at the surfaces which are parallel or sub-parallel to the shear zone and perpendicular to the maximum compressive stress. There is only a small amount of the amorphous material thus we do not assume that it will affect the rheology of the rock. Similar silica gel material was observed in experimentally deformed granite by Di Toro et al. (2004) who documented dynamic weakening of granite with silica gel formation during sliding on fault.

6 Conclusions

The evidence for activity and progress of pressure solution mechanism is shown on an example of quartz – mica – K-feldspar grain boundaries in orthogneiss from South Armorican Shear Zone. The partially open phase boundaries allow fluids to wet the interface and therefore allow the pressure solution to occur at a broad scale of conditions.

The process of dissolution reprecipitation appears to be fairly complex and driven by more than the stress concentration at the interface or chemical composition of fluid. The observations confirm the validity of island and channel model of Wassmann and Stöckhert (2013) and model of leached layers presented by Hellmann et al. (2012). Our data show that within the presence of external stresses the respective crystallographic orientation of phases plays a major role, as well as the fluid presence that directly dissolve the mineral phases, and the local dislocation density or more general the defect density. As shown from the dissolved quartz grains at the interface to mica, the dissolution appears in different locations, where preferentially quartz is being dissolved preferentially along crystallographic surfaces that represent rhomb planes. The crystallographic orientation of mica with respect to the dissolved phase is important, where the dissolution can form the void dissolved sinks, amorphous layers or leached layers even at the same orientation of maximum compressive stress. At the same time the mica might be overgrowing the dissolved phases and thus causing grain size reduction That is significantly important because of the rock rheology and deformation mechanism change as well as the increase of fluid path that is being induced. On a larger scale the grain size reduction is important mechanism allowing plate tectonic processes (Platt and Behr, 2011). Moreover the stress effect in the shear zone can cause both opening of voids and dissolution at the same time.

Acknowledgements

Anja Schreiber is thanked for precise TEM foil preparation. We thank J.P. Gratier and two anonymous reviewers for constructive comments that helped to improve this manuscript. This study was performed during the Erasmus Practical Placement provided by Charles University that allowed Z. Bukovská to work at the GFZ Potsdam. The samples were collected during the field work supported by Charles University Grant Agency Project Nr. 504112.

References

- Ballèvre, M., Bosse, V., Ducassou, C., Pitra, P. (2009). Palaeozoic history of the Armorican Massif: models for the tectonic evolution of the suture zones. *C. R. Geosci.* 341: 174–201.
- Berthé, D., Choukroune, P., Jegouzo, P. (1979). Orthogneiss, mylonite and non coaxial deformation of granites: the example of the South Armorican Shear Zone. *J Struct Geol* 1: 31-42.
- Billia, M.A., Timms, N.E., Toy, V.G., Hart, R.D., Prior, D.J. (2013). Grain boundary dissolution porosity in quartzofeldspathic ultramylonites: Implications for permeability enhancement and weakening of mid-crustal shear zones. *J Struct Geol* 53: 2-14.
- Bray, A.W., Benning, L.G., Bonneville, S., Oelkers, E.H. (2014). Biotite surface chemistry as a function of aqueous fluid composition. *Geochim Cosmochim Acta* 128: 58-70.
- Casey, W.H., Westrich, H.R., Banfield, J.F., Ferruzzi, G., Arnold, G.W. (1993). Leaching and reconstruction at the surfaces of dissolving chain-silicate minerals. *Nature* 366: 253-255.
- Daval, D., Hellmann, R., Saldi, G.D., Wirth, R., Knauss, K.G. (2013). Linking nm-scale measurements of the anisotropy of silicate surface reactivity to macroscopic dissolution rate laws: New insights based on diopside. *Geochim Cosmochim Acta* 107: 121-134.
- Di Toro, G., Goldsby, D.L., Tullis, T.E. (2004). Friction falls towards zero in quartz rock as slip velocity approaches seismic rates. *Nature* 427 (6973): 436-439.
- Fletcher, R.C. (1998). Effects of pressure solution and fluid migration on initiation of shear zones and faults. *Tectonophysics* 295: 139-165.
- Gratier, J.P., Favreau, P., Renard, P. (2003). Modeling fluid transfer along California faults when integrating pressure solution crack sealing and compaction processes. *J Geophys Res* 108. doi: 10.1029/2001JB000380.
- Gratier, J.P., Muquet, L., Hassani, R., Renard, F. (2005). Experimental microstylolites in quartz and modeled application to natural stylolitic structures. *J Struct Geol* 27(1): 89-100.
- Gratier, J.P., Dysthe, D.K., Renard, F. (2013). The role of pressure solution creep in the ductility of the Earth's upper crust. *Advances in Geophysics* 54: 47-179.

Hellmann, R., Penisson, J.-M., Hervig, R.L., Thomassin, J.H., Abrioux, M.F. (2003). An EFTEM/HRTEM high-resolution study of the near surface of labradorite feldspar altered at acid pH: evidence for interfacial dissolution-reprecipitation. *Phys Chem Minerals* 30: 192-197.

Hellmann, R., Wirth, R., Daval, D., Barnes, J.-P., Penisson, J.-M., Tisserand, D., Epicier, T., Florin, B., Hervig, R.L. (2012). Unifying natural and laboratory chemical weathering with interfacial dissolution-reprecipitation: A study based on the nanometer-scale chemistry of fluid-silicate interfaces. *Chem Geol* 294-295: 203-216.

Hövelmann, J., Putnis, A., Geisler, T., Schmidt, B.C., Golla-Schindler, U. (2010). The replacement of plagioclase feldspars by albite: observations from hydrothermal experiments. *Contrib Mineral Petrol* 159: 43-59.

Knipe, R.J., Wirth, R.P. (1985). Heterogeneous deformation, foliation development, and metamorphic processes in a polyphase mylonite. In: *Metamorphic Reactions*, Springer, New York, pp 180-210.

Kruhl J.H., Wirth, R., Morales, L.F.G. (2013). Quartz grain boundaries as fluid pathways in metamorphic rocks. *J Geophys Res-Sol Ea* 118: 1957-1967. doi: 10.1002/jgrb.50099.

Lehner, F.K. (1995). A model for intergranular pressure solution in open systems. *Tectonophysics* 245(3): 153-170.

Mancktelow, N.S., Grujic, D., Johnson, E.L. (1998). An SEM study of porosity and grain boundary microstructure in quartz mylonites, Simplon Fault Zone, Central Alps. *Contrib Mineral Petrol* 131: 71-85.

Menegon, L., Pennacchioni, G., Spiess, R. (2008). Dissolution-precipitation creep of K-feldspar in mid-crustal granite mylonites. *J Struct Geol* 30(5): 565-579.

Miyakawa, K., Kawabe, I. (2014). Pressure solution of quartz aggregates under low effective stress (0.42-0.61 Mpa) at 25-45 °C. *Appl Geochem* 40: 61-69.

Platt, J.P., Behr, W.M. (2011). Lithospheric shear zones as constant stress experiments. *Geology* 39(2): 127-130.

Putnis, A. (2009). Mineral Replacement Reactions. *Rev. Mineral. Geochem.* 70: 87-124.

Putnis, A., John, T. (2010). Replacement Processes in the Earth's Crust. *Elements* 6: 159-164.

Putnis, A., Putnis, C.V. (2007). The mechanism of reequilibration of solids in the presence of a fluid phase. *J Solid State Chem* 180: 1783-1786.

Renard, F., Brosse, É., Gratier, J.P. (2000). The different processes involved in the mechanism of pressure solution in quartz-rich rocks and their interaction. *Spec Publs int Ass Sediment* 29: 67-78.

Rodriguez-Navarro, C., Benning, L.G. (2013). Control of Crystal Nucleation and Growth by Additives. *Elements* 6: 203-209.

Rutter, E.H. (1976). The kinetics of rock deformation by pressure solution. *Phil. Trans. R. Soc.Lond. A.* 283: 203-219.

Rutter, E.H. (1983). Pressure solution in nature, theory and experiment. *J Geol Soc London* 140, 725-740.

Spiers, C.J., Schutjens, P.M.T.M. (1990). Densification of crystalline aggregates by fluid phase diffusional creep. In: Barber DJ, Meredith PJ (Eds.) *Deformation Processes in Minerals, Ceramics and Rocks*. Unwin Hyman, London, 334–353.

Stöckhert, B., Wachmann, M., Küster, M., Bimmermann, S. (1999). Low effective viscosity during high pressure metamorphism due to dissolution precipitation creep: the record of HP-LT carbonates and siliciclastic rocks from Crete. *Tectonophysics* 303: 299-319.

Tartèse, R., Boulvais, P. (2010). Differentiation of peraluminous leucogranites “en route” to the surface. *Lithos* 114: 353-368.

Tartèse, R., Boulvais, P., Poujol, M., Chevalier, T., Paquette, J.L., Ireland, T.R., Deloule, E. (2012). Mylonites of the South Armorican Shear Zone: Insights for crustal-scale fluid flow and water–rock interaction processes. *Journal of Geodynamics* 56: 86-107.

Voll, G. (1976). Recrystallization of quartz, biotite and feldspars from Erstfeld to the Leventina Nappe, Swiss Alps, and its geological significance. *Schweiz. Mineral. Petrogr. Mitt.* 56: 641–647.

Wassmann, S., Stöckhert, B. (2012). Matrix deformation mechanisms in HP-LT tectonic mélanges – Microstructural record of jadeite blueschist from the Franciscan Complex, California. *Tectonophysics* 568-569: 135-153.

Wassmann, S., Stöckhert, B. (2013). Rheology of plate interface – Dissolution precipitation creep in high pressure metamorphic rocks. *Tectonophysics* 608: 1-29, doi: 10.1016/j.tecto.2013.09.030.

Wheeler, J. (1987). The significance of grain-scale stresses in the kinetics of metamorphism. *Contrib Mineral Petrol* 97: 397-404.

Wintsch, R.P., Kvale, C.M., Kisch, H.J. (1991). Open-system, constant-volume development of slaty cleavage, and strain-induced replacement reactions in the Martinsburg Formation, Lehigh Gap, Pennsylvania. *Geological Society of America Bulletin* 103(7): 916-927.

Wirth, R. (2009). Focused Ion Beam (FIB) combined with SEM and TEM: Advanced analytical tools for studies of chemical composition, microstructure and crystal structure in geomaterials on a nanometre scale. *Chem Geol* 261: 217-229. doi: 10.1016/j.chemgeo.2008.05.019.

Supplementary material captions

3D slice-and-view movie along the quartz – white mica interface. The movie shows an interface of quartz (left) and white mica (right). The dissolution processes formed a numerous voids along the phase boundary of the two mineral phases, which are opening and closing – documenting 3D character of the voids. Many of the voids are formed at lower left part, where the protruding voids move into the quartz from the interface of mica. Small grain of K-feldspar (white) occurs along the grain boundary of two quartz grains and in its vicinity another mica grain is grown. Just at the beginning of K-feldspar slicing the pronounced opened grain boundary in between two quartz grains is present. With the growth of mica numerous grain boundaries are more or less opened. Some of the voids are filled with vermiculite (as shown on Fig. 4, 5)

.

CONCLUSIONS

Localization of deformation in crustal anisotropic rocks, such as granites, is an important phenomena that is observed in many areas. The formation of shear zones is studied broadly – this thesis contributes to the topic with description on formation of tiny shear zones – shear bands as well as with the study on the kinematic continuity or discontinuity of such fabric formation. Both development cases are presented here with geodynamic interpretations: a) kinematically discontinuous S-C fabric formed during two different deformational events and b) kinematically continuous S-C fabric formed during single deformational event.

Studies from Tauern Window and Central West Carpathians show examples of kinematically discontinuous S-C fabrics that are found in granitoids and related cover sequences and refer to two distinct deformation events – the first is burial of basement rocks that forms S fabric, while the second forms C fabric and is connected to the exhumation. The difference in the kinematically unrelated fabrics is distinguished by preserved deformation microstructures, mineral associations related to either of these fabrics and its chemical differences that were studied by microanalytical techniques. The differences are more over described in means of thermodynamic conditions of fabric formation, kinematic differences of deformation microstructures and age differences obtained from $^{40}\text{Ar}/^{39}\text{Ar}$ dating and previously published data. On macroscale the difference of the individual fabric distribution across the studied area show the localized deformation event connected to the exhumation of basement rocks, while the S fabric that represents burial is more evenly distributed. Most of the deformation localized in C fabric is found close to the contact of basement granitoids and cover metasediments. The age difference of the two deformational events is estimated to ca. 10-15 million years. In case of Tauern Window the most important asset on the differences is the presence of garnet with prograde zoning in S fabric, while the retrograde mineral association in C fabric. There are several models of extensional exhumation of westernmost Tauern Window (e.g. Selverstone, 1988; Fügenschuh, 1997; Lammerer and Weger, 1998; Rosenberg and Garcia, 2011). In this work the relationship between the fabrics and deformational events and reinterpretation of the main S1 fabric as prograde gives a new sight on its evolution. In Central West Carpathians the difference is mainly in quartz microstructure also accompanied by differences in chemical compositions of micas. These observations led to new interpretation of the exhumation history of Vepor Unit, where aside the previous theories (Hók et al., 1993; Plašienka et al., 1999; Janák et al., 2001) more complete

explanation of evolution has been published (Jeřábek, 2012; and this work).

On the other hand, samples of orthogneisses from South Armorican Shear Zone reveal continuous kinematic evolution of shear bands and S-C fabric defined by Berthé et al. (1979). The granitoid plutons were synkinematically sheared after its emplacement during 315 – 300 Ma (Tartèse et al., 2012) when successively the S and C fabrics formed. The continuity of this deformation and formation of the two fabrics is documented by decreasing temperature – where the temperature difference of fabric formation is ~200 °C. The chemical composition of minerals in either fabric differs as well with temperature as shown e.g. by primary and secondary composition of white mica. The formation of shear bands is continuous process that is here described in three stages. At the first stage microcracking allows income of fluids in the rock and precipitation of minerals within the cracks. It is followed by dynamic recrystallization of quartz and microcline dissolution-precipitation creep in stage II. Stage III is dominated by localized slip along white mica bands accommodated by dislocation creep that is followed by pressure solution along the white mica in shear bands. The evolution of shear bands as documented here show positive feedback between the deformation mechanisms and chemical processes that are closely related to fluids present in the shear zone and the switches in deformation localization and delocalization. The estimated conditions reveal shear band localization at the brittle-plastic transition in dominantly weakening regime. Such non-steady-state evolution might be common in shear zones if phase transformations are included.

The detailed look on the deformation mechanisms led to study of pressure solution which was assumed to operate on the boundaries of white mica in shear band and the matrix minerals. Transmission electron microscopy revealed important features indicative for dissolution creep such as rough boundaries, dissolution pits and presence of amorphous phase. The observations show evidence for operation of island-and-channel model as described in Wassmann and Stöckhert (2013) and formation of amorphous layers via interface-coupled dissolution-reprecipitation as described by Hellmann et al. (2012). Both these mechanisms are present under oriented stress and thus represent pressure solution features as it has never been shown before.

The indicative criteria for distinguishing the continuity of the S-C fabrics studied in this work include microstructure of the respective fabrics, mineral associations and mineral chemistry changes, age and P-T estimates together with precise field work. However, great attention should be paid to combination of proper techniques on micro- and macro-scale.

The observation from macroscopic structure down to the nanometric features on grain interfaces document shear bands and S-C fabric formation in either kinematically continuous or discontinuous evolution. This study shows the importance of detailed studies of macroscopic structures and combination of different corner points and analyses on different scales. In order to understand the crustal processes it is of great importance to understand deformation processes and mechanisms from the basis on micro/nanoscale, which allows the extrapolation and interpretation of geodynamic evolution.

References

- Berthé, D., Choukroune, P., Jegouzo, P. (1979). Orthogneiss, mylonite and noncoaxial deformation of granites: the example of the South Armorican Shear Zone. *Journal of Structural Geology* 1, 31-42.
- Fügenschuh, B., Seward, D., Mancktelow, N. (1997). Exhumation in a convergent orogen: the western Tauern window. *Terra Nova*, 9 (5-6), 213-217.
- Hellmann, R., Wirth, R., Daval, D., Barnes, J.-P., Penisson, J.-M., Tisserand, D., Epicier, T., Florin, B., Hervig, R.L. (2012). Unifying natural and laboratory chemical weathering with interfacial dissolution-precipitation: A study based on the nanometer-scale chemistry of fluid-silicate interfaces. *Chem Geol* 294-295: 203-216
- Hók, J., Kováč, P., Madarás, J. (1993). Extensional tectonics of the western part of the contact area between Veporicum and Gemericum (Western Carpathians). *Mineralia Slovaca* 25, 172-176 (in Slovak with English summary).
- Janák, M., Plašienka, D., Frey, M., Cosca, M., Schmidt, S.T., Lupták, B., Méres, Š. (2001). Cretaceous evolution of a metamorphic core complex, the Veporic unit, Western Carpathians (Slovakia): P–T conditions and in situ $^{40}\text{Ar}/^{39}\text{Ar}$ UV laser probe dating of metapelites. *Journal of Metamorphic Geology* 19, 197–216.
- Jeřábek, P., Lexa, O., Schulmann, K., Plašienka, D. (2012). Inverse ductile thinning via lower crustal flow and fold-induced doming in the West Carpathian Eo-Alpine collisional wedge. *Tectonics*, 31(5).
- Lammerer, B., Weger, M. (1998). Footwall uplift in an orogenic wedge: the Tauern Window in the Eastern Alps of Europe. *Tectonophysics*, 285(3), 213-230.
- Plašienka, D., Janák, M., Lupták, B., Milovský, R., Frey, R. (1999). Kinematics and metamorphism of a Cretaceous core complex: the Veporic unit of the Western Carpathians. *Phys. Chem. Earth (A)* 24, 651-658.
- Rosenberg, C. L., Garcia, S. (2011). Estimating displacement along the Brenner Fault and orogen-parallel extension in the Eastern Alps. *International Journal of Earth Sciences*, 100(5),

1129-1145.

Selverstone, J. (1988). Evidence for east-west crustal extension in the Eastern Alps: Implications for the unroofing history of the Tauern window. *Tectonics*,7(1), 87-105.

Tartèse, R., Boulvais, P., Poujol, M., Chevalier, T., Paquette, J. L., Ireland, T. R., Deloule, E. (2012). Mylonites of the South Armorican Shear Zone: Insights for crustal-scale fluid flow and water–rock interaction processes, *Journal of Geodynamics*, 56, 86-107.

Wassmann, S., Stöckhert, B. (2013). Rheology of plate interface – Dissolution precipitation creep in high pressure metamorphic rocks. *Tectonophysics* 608: 1-29, doi: 10.1016/j.tecto.2013.09.030